University of Sussex

CMB Lensing: Polarization, Large-Scale Structure and the Primordial Bispectrum

Ruth Pearson

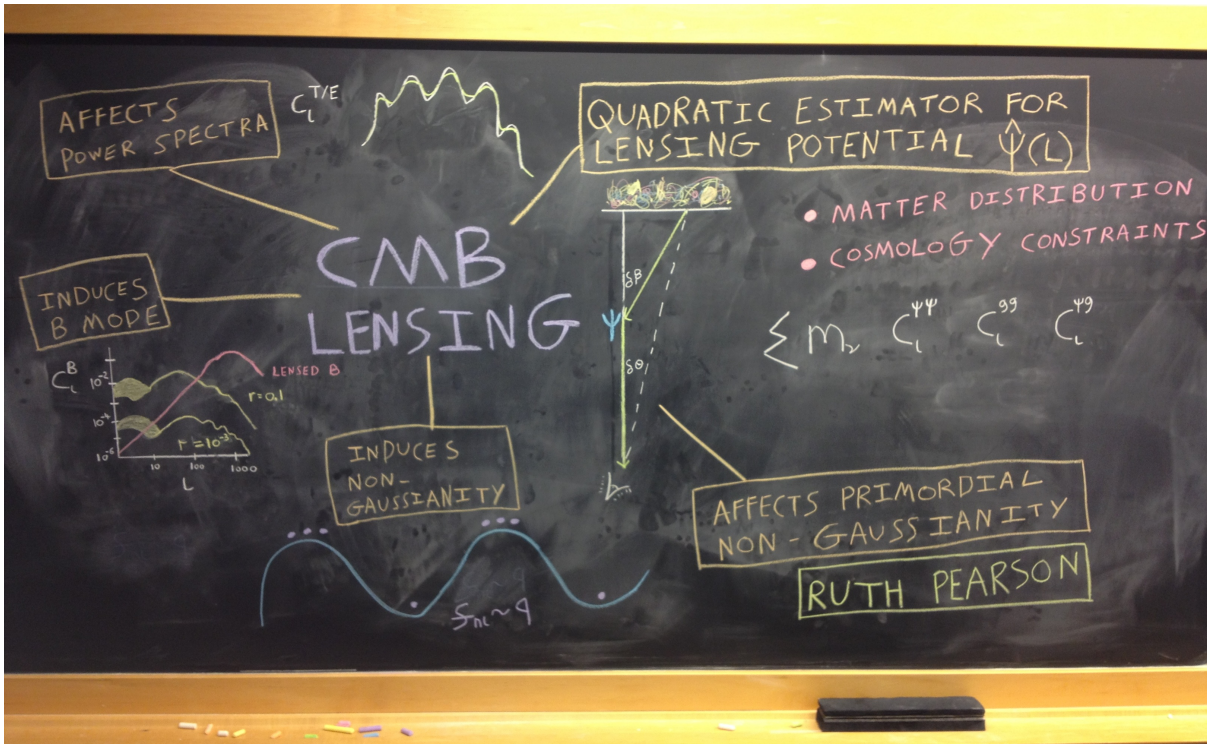

Submitted for the degree of Doctor of Philosophy

University of Sussex

March 2014

UNIVERSITY OF SUSSEX

Ruth Pearson, Doctor of Philosophy

CMB Lensing: Polarization, Large-Scale Structure and the Primordial Bispectrum

Abstract

Gravitational lensing of photons in the Cosmic Microwave Background (CMB) can be described by an integrated potential along the line of sight, the CMB lensing potential. Covariances in maps of the CMB are generated by the lensing effect, and are used to reconstruct the lensing potential itself, which is a useful probe of the matter distribution. The CMB lensing potential has been measured to high significance with CMB temperature data. However, signal to noise for lensing reconstruction from CMB polarization data is expected to be much better due to the presence of the lensing B-mode. Upcoming data from ground based CMB polarization instruments will provide high resolution maps over small patches of the sky. This will provide much better lensing reconstruction, but also presents data analysis challenges. This thesis begins with an introduction to the field of CMB lensing and CMB lensing reconstruction. The second chapter details the biases present in reconstructing the lensing potential from CMB polarization maps considering first the full sky, and then small patches of sky. It also shows that using the pure-B mode formalism for the CMB polarization leads to improved lensing reconstruction over the naive case on the cut sky. Given the upcoming improvement in the CMB lensing reconstruction, it is expected that cross-correlations of the CMB lensing with other structure tracers, such as galaxies, will yield improved information for cosmology. It is also expected that the CMB lensing will become useful to help constrain uncertainties in the galaxy power spectrum, and provide information on the linear galaxy bias and redshift distribution. The third chapter of the thesis forecasts the power of cross correlation science for a number of galactic and non-galactic parameters. Finally, the CMB lensing effects the level of non-Gaussianity observed in the CMB. The fourth chapter of the thesis is a study of the lensing effect on the primordial squeezed bispectrum. We conclude in the fifth chapter.

Acknowledgements

There are many people that I would like to thank for supporting me on this journey, I will mention only a few of them here. For the freedom to do my own thing as well as infinite time and patience when I asked for help: my supervisor Antony Lewis. For hosting me in California: the Chao-Lin Kuo group at Stanford. My colleagues and collaborators, especially: Donough Regan, Oliver Zahn, Blake Sherwin, Amanda Yoho, Kristin Mikkelsen, Katie Mack and all of my office mates. For believing in me: Zara Abdelrahman, Victoria Martin and Gemma Anderson. For the telescope: Nick Pearson. For a home: Ithaka Coop, 7 Delano, The Maritol, Flat 15, 25 Margaret St. and Rainbow Mansion.

Contents

Chapter 1

Introduction

When I was born (1988), our understanding of the universe was in its infancy. We knew little of the geometry of the universe, nothing of the existence of dark energy, and we'd never observed anisotropies in the cosmic microwave background (CMB). Now we've measured all three at better than percent level and can say with increasing confidence that all the structure in the universe originates as quantum fluctuations soon after the big bang.

The standard model of cosmology, ΛCDM, is the best fit model of the universe to current data. The 'Λ' denotes that we expect a universe with some scalar field which is driving the expansion of the universe, (sometimes a cosmological constant). The 'CDM' term describes Cold Dark Matter. We think that the universe contains mostly dark matter — matter which does not emit light but interacts gravitationally — which does not have much kinetic energy, hence 'cold'. Edwin Hubble was first to observe that galaxies are moving away from us at a rate proportional to their distance, the first evidence of an expanding universe. If we believe that the universe is moving apart in all directions, rewinding this picture leads to an initial state where all the matter is densely packed into one point. This idea is the foundation of the current picture of the beginning of the universe which we call the hot big bang model. An important consequence of big bang cosmology is a period of nucleosynthesis in the early universe in which light elements are created, something which is very well supported by observation.

Another cornerstone of the standard cosmology is a period of exponential expansion know as inflation, which takes place a fraction of a second after the universe begins. The simplest model for inflation is the standard slow roll model. In slow roll inflation there exists a single scalar field driving the exponential expansion of the universe. This field rolls slowly down its potential until it reaches the global minimum at which point inflation ends and the energy is transformed into standard model particles via a period called reheating.

A period of exponential expansion is required in our model to solve some outstanding problems which would exist without it:

1. *The Flatness Problem:* A priori the geometry of the universe could be open, closed or flat. These scenarios correspond to a curvature which is positive ($\Omega_k > 0$), negative ($\Omega_k < 0$) or zero ($\Omega_k = 0$). Observations tell us that the universe is very close to flat, which without inflation corresponds to having an exceedingly flat universe as an initial condition which presents a fine tuning problem. However, if we assume a long enough period of inflation (more than 60 e-folds), any initial geometry will look spatially flat to an observer in a causal patch.

2. *The Horizon Problem:* The horizon size is the maximum distance that light can travel in the age of the universe. Things outside of each others' horizon are causally disconnected. The horizon size at the surface of last scattering corresponds to an angular size on the sky today of $\sim 2^\circ$. However, measurements of the CMB confirm that it is homogeneous across the whole sky to one part in 10^{-5}. This implies that the photons across the whole sky were once in causal contact, which makes sense in the standard cosmology if we allow for a period of inflation.

3. *The Magnetic Monopole Problem:* The standard model of particle physics suggests that we should expect to observe magnetic monopoles as a large fraction of the energy density in the universe. Without a period of inflation, the hot big bang model is not able to explain why we do not observe the magnetic monopole.

A slowly rolling field for inflation is the simplest model which fits current observations. However, there is a large number of other more complicated models for inflation which can also describe current observations, and a major challenge of modern cosmology is to distinguish between these different models. During the period of inflation, there are quantum fluctuations in the value of the potential which become perturbations in the density field after inflation finishes. The details of these perturbations is therefore imprinted in the CMB and hence there is opportunity to make observations which may help to distinguish between the many inflationary models. In fact, due to the successes in measuring the CMB the field of cosmology has become a precision science. For full reviews of modern cosmology see Dodelson (2003) and Liddle & Lyth (2000).

When we point our telescopes into the sky we observe a background radiation across the whole sky which is in the microwave spectrum at a temperature of ~ 2.7K. This is the CMB which has yielded two Nobel prizes in physics. The photons that comprise this

radiation come from a very specific early time in the universe, the period of so called recombination at a redshift of around 1000, or roughly 300,000 years after the big bang. The early universe was a hot dense opaque plasma. But as the universe expanded, the plasma became less hot and less dense. Eventually it was cool enough that electrons and protons were able to form stable hydrogen atoms, after which photons were able to free stream without being constantly Compton scattered: the universe became transparent.

It was the photons released during this epoch of "last scattering" that have travelled through the universe to be observed in our telescopes today as the CMB. In fact when we measure the CMB we find small changes in its temperature and polarization at the 10^{-5} level. These small fluctuations were seeded by quantum fluctuations during inflation which became fluctuations in the density field after reheating. As such the CMB is like a snap shot of the universe at early times, and we can learn much about cosmology when we analyse the CMB temperature and polarization anisotropy. There have been three major satellite missions to date which have observed the CMB over (almost) the full sky: COBE (NASA, 2014a), WMAP (NASA, 2014c) and Planck (ESA, 2014). A comparison of these missions is shown in Fig. 1.1. There are many other ground based telescopes and balloon borne missions measuring smaller fractions of the CMB sky. The statistical properties of the CMB temperature and polarization anisotropies are described in section 1.1.

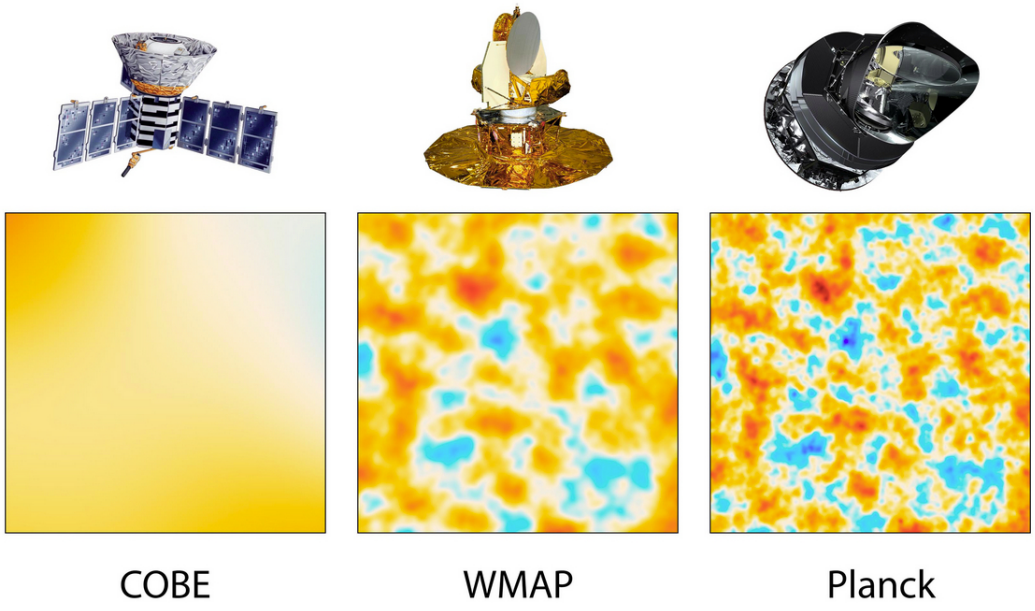

Figure 1.1: A comparison of the resolution of the COBE (NASA, 2014a), WMAP (NASA, 2014c) and Planck (ESA, 2014) satellites measuring CMB temperature fluctuations over a $10^\circ \times 10^\circ$ patch of sky (NASA, 2014b).

However, as the CMB photons travel through the universe, they encounter gravitational potentials. The potentials deflect the path of the CMB photons. This moves around on the sky the photons which we observe, though surface brightness is preserved. Figure 1.2 shows how the Earth would look if 1000× the magnitude of the CMB lensing was applied to a map of it. The CMB lensing effect introduces signals in the primary CMB such as B mode polarization and non-Gaussianity, but is also interesting itself as it probes the matter distribution from a high redshift source (the surface of last scattering) until today. Since the photons are deflected by both baryonic and dark matter, the matter distribution that the lensing traces is a combination of the two. The same quantum fluctuations which gave rise to the anisotropy in the CMB also seeded the large-scale structure of the universe. The structure of the biggest thing we know — the whole observable universe — is seeded by the smallest thing we know, quantum fluctuations. When we observe the structure of the universe we look at galaxies and clusters of galaxies across a range of wavelengths. Unlike for the CMB, the large-scale structure is highly non-linear and contains 3-Dimensional information since a range of redshifts can be observed.

The CMB lensing effect is sensitive to the geometry of the universe (e.g. dark energy and its evolution) and the shape of the matter power spectrum (affected by e.g. massive neutrinos). It is well known that CMB lensing breaks the degeneracy between the neutrino mass fraction Ω_ν and the dark energy fraction Ω_Λ, and using this information CMB lensing can be used to distinguish between cosmological models. The lensing of the CMB photons can be described by an integrated potential along the line of sight, the CMB lensing potential. The covariances in the CMB maps generated by the lensing are used to reconstruct the lensing potential itself, usually using the so called quadratic estimator. Using this method, the CMB lensing potential has been measured with CMB temperature data, yielding high significance measurements of the lensing power spectrum. However signal to noise for lensing reconstruction from CMB polarization data is expected to be much better, since B modes on small scales are not present in the absence of lensing. The statistical properties and reconstruction details for the CMB lensing are described in section 2.1.1.

An effect of having CMB data from an incomplete sky is leakage of E mode power in to B mode power. Upcoming data analysis from ground-based CMB polarization instruments will provide high resolution maps over small patches of the sky and therefore must account for this effect. The SPT Pol (Austermann et al., 2012), POLARBEAR (Kermish et al., 2012) and ACT Pol (Niemack et al., 2010) experiments are already taking

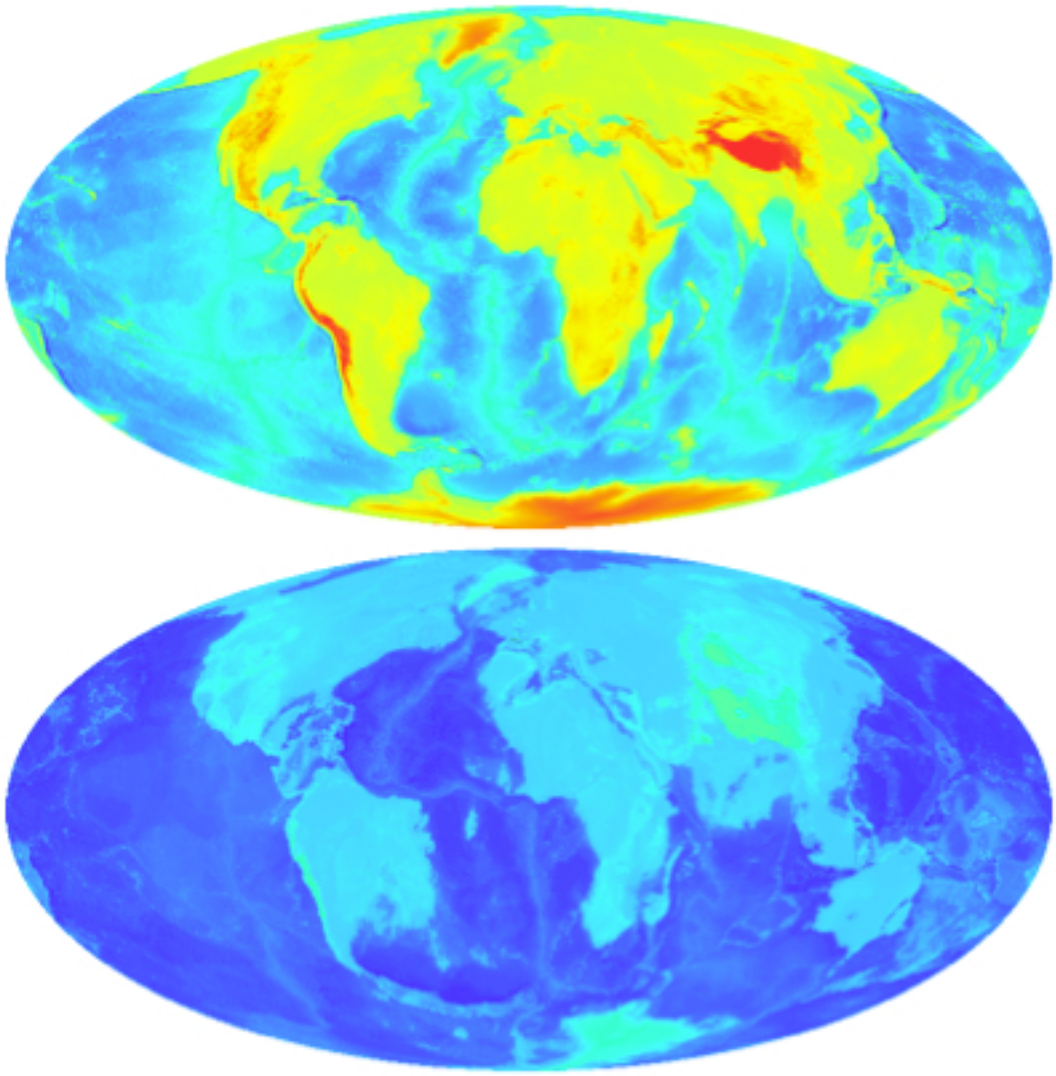

Figure 1.2: Top: An image of the Earth. Bottom: Top image lensed by 1000× the magnitude of the CMB lensing potential.

such data, and the SPT 3G and Simons Array experiments are planned for the future. In Chapter 2 we derive forecasts for CMB polarization lensing reconstruction from small patches of sky, which incorporate the pure-B mode estimator to clean up this problem of E-B leakage. We show the biases associated with full sky (periodic boundary condition) lensing reconstruction from polarization and that using the pure-B mode formalism to account for ambiguous modes in the E-B leakage improves the lensing reconstruction over the naive case on the cut sky.

Since CMB lensing probes all matter, it should be well correlated with galaxy surveys observing the large-scale structure of the universe, indeed CMB lensing was first detected via cross correlation with a radio survey. Current experiments are good enough to detect the CMB lensing potential without the help of an auxiliary tracer, and the cross correlation between CMB lensing and large-scale structure surveys should aid in simultaneously measuring galactic and non-galactic cosmological information. There is already a wealth of data available for such analysis, and upcoming surveys such as LSST (Abell et al., 2009) and DES (Abbott et al., 2005), will offer even better opportunities for cross correlation science. Structure surveys observe light from distant galaxies. However, we know that there is a bias between the light from galaxies and the underlying matter distribution, discussed more in section 1.4. This bias is redshift dependent and non-linear at a scale which is not yet fully understood. The CMB lensing traces the dark matter directly, and so it can be analysed jointly with the galaxy information to help control uncertainties in the linear galaxy bias. There are many other biases and systematic effects associated with analysing galaxy survey data, whereas CMB lensing is a relatively clean probe. For example, it has been shown that CMB lensing can break degeneracies in galaxy analysis between power spectrum normalisation and certain systematic biases (Vallinotto, 2012). In Chapter 3 we show that the joint analysis of these complementary probes will allow much better measurements on parameters such as the linear galaxy bias and the galaxy redshift distribution.

The primordial CMB fluctuations are often assumed Gaussian in nature. However, deviations from Gaussianity in the CMB have been a hot topic of research, since any non-Gaussian signal has the potential to teach us about conditions during inflation. Some measurement bounds of the non-Gaussianity have promised to rule out entire classes of models of inflation, though to date the non-Gaussianity measured from the CMB is consistent with zero. Since we are now searching for very small non-Gaussian signals, it is important to understand how the CMB lensing will change the non-Gaussian signal.

Modelling methods can be computationally expensive, and in Chapter 4 we discuss an approximation for the lensed bispectrum (3-point correlation function) which allows a less computationally expensive method.

1.1 The Cosmic Microwave Background Observables

For a review of the physics of the CMB see e.g. Challinor & Peiris (2009). When we point our telescopes at the CMB, what we actually measure are the Stokes parameters I, Q and U. Stokes parameters describe electromagnetic radiation by splitting a correlation matrix into intensity, linear polarization and circular polarization. An observation can be defined in terms of an intensity correlation matrix

$$\mathbb{P} = c\langle E_a E_b^* \rangle, \tag{1.1}$$

where c is a constant that normalises $\mathbb{P}$ to be measured in temperature units and the angle brackets denote a time average. This is a rank 2 tensor and can be decomposed into irreducible parts

$$\mathbb{P} = P_{ab} + \frac{1}{2}\delta_{ab} I + V_{[ab]}. \tag{1.2}$$

P_{ab} is the symmetric trace-free part, I is the total power intensity and $V_{[ab]}$ is the antisymmetric part corresponding to circular polarization. Thomson scattering in the CMB does not induce circular polarization, so the $V_{[ab]}$ is not considered further.

1.1.1 CMB temperature

The I component of the Stokes parameters corresponds to the CMB temperature which we write in terms of spherical harmonics as

$$\frac{\triangle T(\hat{\mathbf{n}})}{\bar{T}} = \sum_{lm} T_{lm} Y_{lm}(\hat{\mathbf{n}}). \tag{1.3}$$

The left hand side of the equation expresses the temperature perturbation $\triangle T(\hat{\mathbf{n}})$ in the direction $\hat{\mathbf{n}}$, relative to the mean background temperature $\bar{T}$. On the right hand side of the equation, $Y_{lm}(\hat{\mathbf{n}})$ are the spherical harmonics and contain all the information about direction. The T_{lm} are the spherical harmonic coefficients and since the temperature is a real field $T_{lm}^* = (-1)^m T_{l-m}$. For the spherical harmonics, $l \geq 1$ and $-l \leq m \leq l$. Assuming that each T_{lm} is a Gaussian random variable, the 2-point correlation function of the harmonic coefficients is

$$\langle T_{lm} T_{l'm'}^* \rangle = \delta_{ll'} \delta_{mm'} C_l^{TT}. \tag{1.4}$$

Since in practice we only have one sky to observe and cannot take the ensemble average, we construct the estimator for the power spectrum

$$\hat{C}_l^{TT} = \frac{1}{2l+1} \sum_{m=-l}^{l} |T_{lm}|^2. \tag{1.5}$$

This estimator is unbiased ($\langle \hat{C}_l^{TT} \rangle = C_l^{TT}$) and has a variance of

$$V[\hat{C}_l^{TT}] = \frac{2(C_l^{TT})^2}{2l+1}. \tag{1.6}$$

The variance is calculated via Wick's theorem, where for Gaussian variables all higher order statistics can be reduced to power spectra. The variance decreases at higher multipoles, since $-l \leq m \leq l$ and there are more T_{lm}s to average over for higher multipoles.

In practice, since many experiments only observe small patches of sky, it is often convenient to work in the flat-sky approximation where the temperature anisotropy becomes

$$T(\mathbf{x}) = \int \frac{d^2\mathbf{l}}{2\pi} T(\mathbf{l}) e^{i\mathbf{l}\cdot\mathbf{x}} \tag{1.7}$$

and

$$T(\mathbf{l}) = \int \frac{d^2\mathbf{x}}{2\pi} T(\mathbf{x}) e^{-i\mathbf{l}\cdot\mathbf{x}}, \tag{1.8}$$

where $\mathbf{x}$ substitutes $\hat{\mathbf{n}}$ and is the position on the plane of the sky. The best measurement to date of the temperature power spectrum of the CMB has been from the Planck satellite (Ade et al., 2013e) and is shown in Fig. 1.3.

1.1.2 CMB polarization

The P_{ab} component of the intensity matrix is written in terms of the basis dependent Stokes parameters Q and U:

$$P_{ab} = \frac{1}{2} \begin{pmatrix} Q & U \\ U & -Q \end{pmatrix}. \tag{1.9}$$

P_{ab} is a rank 2 tensor, and can be written in terms of two scalar fields P_E and P_B

$$P_{ab} = \nabla_{\langle a} \nabla_{b\rangle} P_E + \epsilon^c{}_{(a} \nabla_{c)} \nabla_b P_B. \tag{1.10}$$

The left hand side of the equation is the physical quantity, the right hand side is the projection into scalar fields. Angle brackets around indices denote the symmetric trace-free part, while curly brackets denote the antisymmetric part. ∇_a is a covariant derivative on the surface orthogonal to the observation direction $\hat{\mathbf{n}}$. P_E describes the parity invariant "E mode" and P_B describes the curl-like "B mode". The polarization patterns of the E and B mode are shown in Fig 1.4. Expressed in the spherical harmonics:

$$(Q \pm iU)(\hat{\mathbf{n}}) = \sum_{lm} (E_{lm} \mp iB_{lm})_{\mp 2} Y_{lm}(\hat{\mathbf{n}}), \tag{1.11}$$

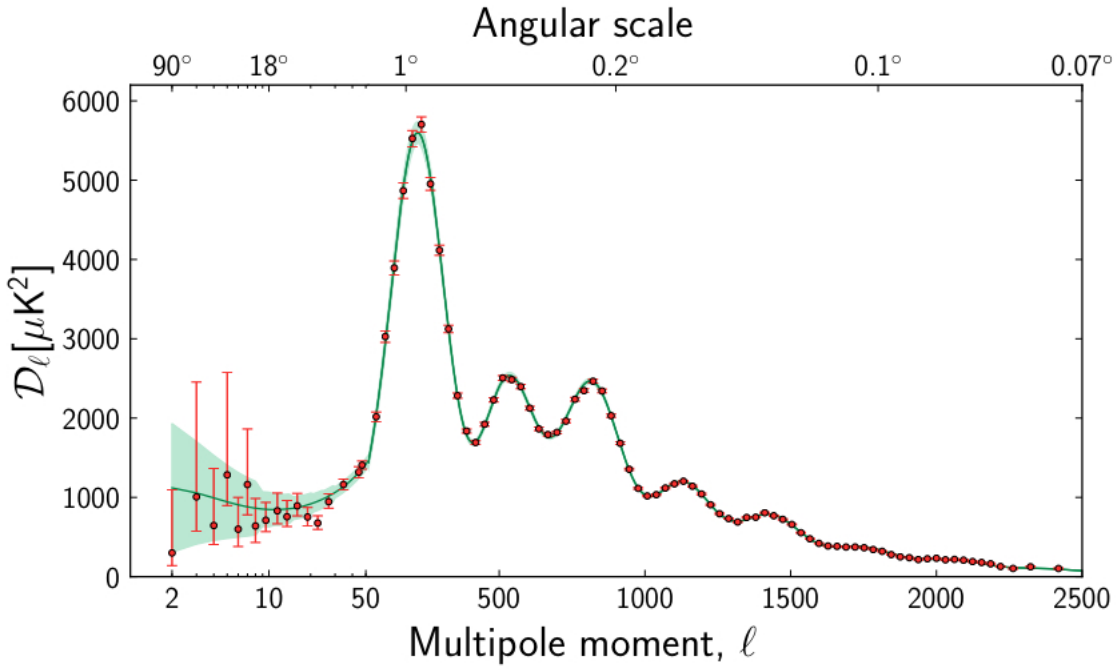

Figure 1.3: The temperature power spectrum measured by Planck (Ade et al., 2013e), where $\mathcal{D}_l \equiv \frac{l(l+1)C_l^{TT}}{2\pi}$.

where ${}_{\mp 2}Y_{lm}(\hat{\mathbf{n}})$ are the spin ∓ 2 spherical harmonics and Q and U are defined relative to the polar-coordinate basis. The E and B mode power spectra are:

$$\langle E_{lm} E^*_{l'm'} \rangle = \delta_{ll'} \delta_{mm'} C_l^{EE} \tag{1.12}$$

and

$$\langle B_{lm} B^*_{l'm'} \rangle = \delta_{ll'} \delta_{mm'} C_l^{BB}. \tag{1.13}$$

The temperature and E mode also correlate to produce the cross-power spectrum:

$$\langle T_{lm} E^*_{l'm'} \rangle = \delta_{ll'} \delta_{mm'} C_l^{TE}. \tag{1.14}$$

Due to parity invariance there are no TB or EB correlations. As in the temperature case, it is often useful to express the Q and U stokes parameters and the E and B modes using the flat sky approximation:

$$[Q \pm iU](\mathbf{x}) = -\int \frac{d^2\mathbf{l}}{2\pi} [E(\mathbf{l}) \pm iB(\mathbf{l})] e^{\pm 2i\varphi_l} e^{i\mathbf{l}\cdot\mathbf{x}}; \tag{1.15}$$

$$[E(\mathbf{l}) \pm iB(\mathbf{l})] = -\int \frac{d^2\mathbf{x}}{2\pi} [Q \pm iU](\mathbf{x}) e^{\mp 2i\varphi_l} e^{-i\mathbf{l}\cdot\mathbf{x}}. \tag{1.16}$$

This assumes a Cartesian basis for Q and U, which is a simple rotation from the polar-coordinate basis on the full sky.

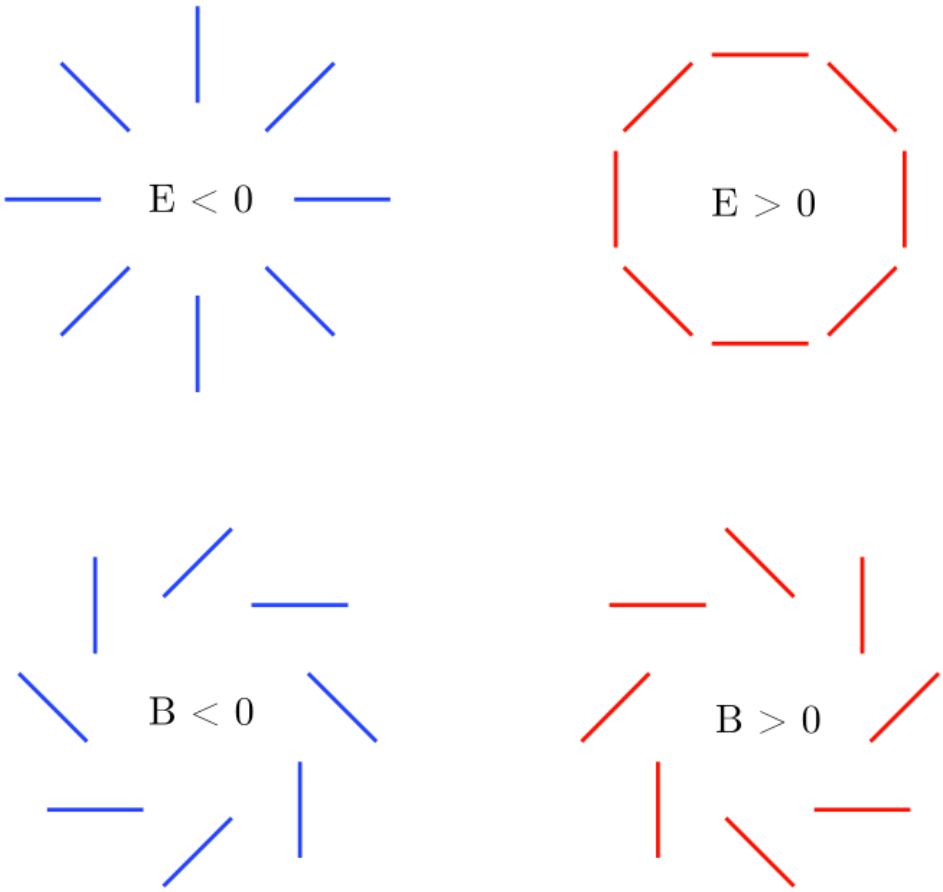

Figure 1.4: Polarization patterns for azimuthally-symmetric E and B modes.

1.2 CMB Lensing

1.2.1 The lensing deflection angle and the lensing potential

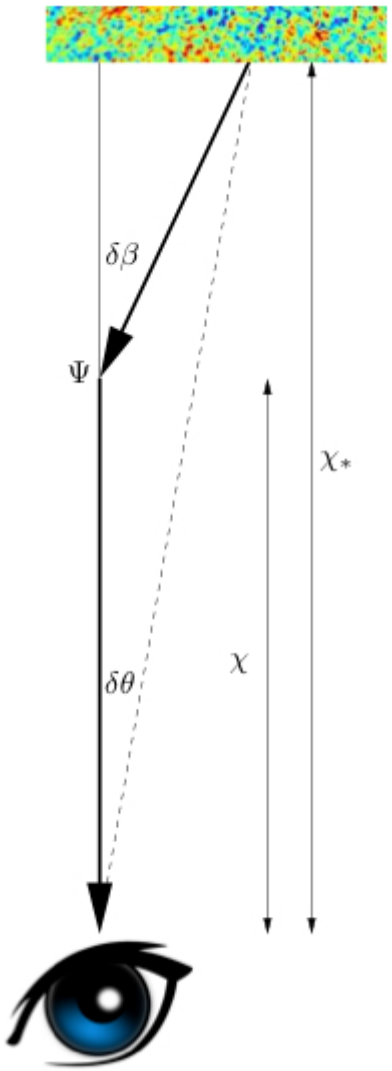

Figure 1.5: An illustration of the deflection of a CMB photon caused by a gravitational potential Ψ at distance χ from the observer.

For a full review of the CMB lensing effect see Refs. Lewis & Challinor (2006) and Hanson et al. (2010). It is well known that a gravitational potential will bend the path of light. We would like to know how much the gravitational potentials in the universe will deflect the CMB photons, so we start with a simple Newtonian calculation: for a photon approaching a point mass M the gravitational potential Ψ is

$$\Psi = \frac{GM}{r}, \tag{1.17}$$

where G is Newton's constant and r is the distance between the photon and point mass M. The transverse acceleration of the photon due to the mass is

$$\dot{v}_\perp = -\nabla_\perp \Psi = \frac{GM}{r^2}\cos\theta. \tag{1.18}$$

Where θ is the angle of the photon from the mass relative to its angle at a distance of closest approach R_0. Integration over the photon path for constant speed $|\mathbf{v}| = c$ gives a total (Newtonian) deflection angle:

$$\frac{v_\perp}{|\mathbf{v}|} = \frac{2GM}{c^2 R_0}, \tag{1.19}$$

where we can use natural units and set $c = 1$. In General Relativity, we replace the derivative with the covariant derivative giving an acceleration of $D_\chi \hat{\mathbf{v}} = -\nabla\Psi$ where D_χ is the covariant derivative along the photon world line. To get the deflection angle, we must also account for the curvature of space to give a local deflection angle of

$$\delta\beta = -2\delta_\chi \nabla_\perp \Psi, \tag{1.20}$$

where δ_χ is a small distance along the photon path. This General Relativity result is essentially the Newtonian result plus an equal term due to the effect of space-time curvature. We would like to know how a deflection in a photon's path changes its observed angle on the sky. The angular diameter distance $f_K(\chi)$ relates comoving distances to angles via:

$$f_K(\chi) = \begin{cases} K^{-1/2}\sin(K^{1/2}\chi) & \text{for } K > 0, \text{ closed,} \\ \chi & \text{for } K = 0, \text{ flat,} \\ |K|^{-1/2}\sinh(|K|^{1/2}\chi) & \text{for } K < 0, \text{ open.} \end{cases} \tag{1.21}$$

We are working under the approximation of weak lensing and in the small angle approximation $f_K(\chi_* - \chi)\delta\beta = f_K(\chi_*)\delta\theta$. Solving for $\delta\theta$ the deflection due to the source at χ is

$$\delta\theta_\chi = \frac{f_K(\chi_* - \chi)\delta\beta}{f_K(\chi_*)} = \frac{f_K(\chi_* - \chi)}{f_K(\chi_*)} 2\delta_\chi \nabla_\perp \Psi. \tag{1.22}$$

The total deflection angle is a sum over all of the individual deflections due to gravitational potentials between the surface of last scattering and today:

$$\alpha = -2\int_0^{\chi_*} d\chi \frac{f_K(\chi_* - \chi)}{f_K(\chi_*) f_K(\chi)} \nabla_\perp \Psi(\chi\hat{\mathbf{n}}, \eta_0 - \chi), \tag{1.23}$$

where $\eta_0 - \chi$ is the conformal time at which a photon was at position $\chi\hat{\mathbf{n}}$. We then define the lensing potential:

$$\phi(\hat{\mathbf{n}}) \equiv -2\int_0^{\chi_*} d\chi \frac{f_K(\chi_* - \chi)}{f_K(\chi_*) f_K(\chi)} \Psi(\chi\hat{\mathbf{n}}, \eta_0 - \chi), \tag{1.24}$$

so that $\alpha = \nabla_{\hat{\mathbf{n}}}\phi$ which in the following text will be written as simply $\alpha = \nabla\phi$. We will assume a flat geometry where angular diameter distance $f_K(\chi) = \chi$, and take last scattering as a plane at $\chi = \chi_*$. The lensing potential looks divergent at $\chi = 0$, but the divergence only affects the monopole which does not contribute to the deflection angle. It is useful to consider the 2-point correlation of the lensing potential, the lensing potential power spectrum. To calculate this, expand the 3-dimensional gravitational potential Ψ into harmonic space

$$\Psi(\mathbf{x}, \eta) = \int \frac{d^3\mathbf{k}}{(2\pi)^{3/2}} \Psi(\mathbf{k}, \eta) e^{i\mathbf{k}\cdot\mathbf{x}}. \tag{1.25}$$

Assuming the gravitational potential is statistically homogeneous, its power spectrum is

$$\langle \Psi(\mathbf{k}, \eta) \Psi^*(\mathbf{k}', \eta') \rangle = \frac{2\pi^2}{k^3} \mathcal{P}_\Psi(k, \eta, \eta') \delta(\mathbf{k} - \mathbf{k}'), \tag{1.26}$$

where η is conformal time. Taking the 2-point correlation function of Eq. (1.24) reduces to the 2-point correlation of Eq. (1.25) and we can use the result of Eq. (1.26) to write:

$$\langle \phi(\hat{\mathbf{n}}) \phi(\hat{\mathbf{n}'}) \rangle = 4\int_0^{\chi_*} d\chi \int_0^{\chi_*} d\chi' \left(\frac{\chi_* - \chi}{\chi_* \chi}\right)\left(\frac{\chi_* - \chi'}{\chi_* \chi'}\right) \int \frac{d^3\mathbf{k}}{(2\pi)^3} \frac{2\pi^2}{k^3} \mathcal{P}_\Psi(k, \eta, \eta') e^{i\mathbf{k}\cdot\mathbf{x}} e^{-i\mathbf{k}\cdot\mathbf{x}'}. \tag{1.27}$$

Where $\mathbf{x} = \chi\hat{\mathbf{n}}$ and $\mathbf{x}' = \chi\hat{\mathbf{n}}'$. We can use the result

$$e^{i\mathbf{k}\cdot\mathbf{x}} = 4\pi \sum_{lm} i^l j_l(k\chi) Y^*_{lm}(\hat{\mathbf{n}}) Y_{lm}(\hat{\mathbf{k}}), \tag{1.28}$$

where the spherical Bessel function $j_l(r) = (\pi/2r)^{1/2} J_{l+1/2}(r)$ where J is the standard Bessel function. Consider the $\mathbf{k}$ integral in spherical coordinates

$$\int d^3\mathbf{k} = \int k^2 dk d\hat{\mathbf{k}}, \tag{1.29}$$

and the orthogonality of the spherical harmonics

$$\int d\hat{\mathbf{k}} Y_{lm}(\hat{\mathbf{k}}) Y^*_{l'm'}(\hat{\mathbf{k}}) = \delta_{ll'}\delta_{mm'}. \tag{1.30}$$

Using Eq. (1.29) and Eq. (1.30) the angular integral can be taken over $\hat{\mathbf{k}}$ to yield

$$\begin{aligned} \langle \phi(\hat{\mathbf{n}}) \phi(\hat{\mathbf{n}'}) \rangle &= 16\pi \sum_{ll'mm'} \int_0^{\chi_*} d\chi \int_0^{\chi_*} d\chi' \left(\frac{\chi_* - \chi}{\chi_* \chi}\right)\left(\frac{\chi_* - \chi'}{\chi_* \chi'}\right) \\ &\quad \times \int \frac{dk}{k} j_l(k\chi) j_l(k\chi') \mathcal{P}_\Psi(k, \eta, \eta') Y_{lm}(\hat{\mathbf{n}}) Y^*_{l'm'}(\hat{\mathbf{n}'}) \delta_{ll'}\delta_{mm'}. \end{aligned} \tag{1.31}$$

Expanded in spherical harmonics, the lensing potential is

$$\phi(\hat{\mathbf{n}}) = \sum_{lm} \phi_{lm} Y_{lm}(\hat{\mathbf{n}}), \tag{1.32}$$

and assuming statistical isotropy the power spectrum is

$$\langle \phi_{lm} \phi^*_{l'm'} \rangle = \delta_{ll'} \delta_{mm'} C_l^{\phi\phi}. \tag{1.33}$$

Taking the 2-point correlation of Eq. (1.32):

$$\begin{aligned} \langle \phi(\hat{\mathbf{n}}) \phi(\hat{\mathbf{n}'}) \rangle &= \sum_{ll'mm'} \langle \phi_{lm} \phi^*_{l'm'} \rangle Y_{lm}(\hat{\mathbf{n}}) Y_{lm}(\hat{\mathbf{n}'}) \\ &= \sum_{ll'mm'} \delta_{ll'} \delta_{mm'} C_l^{\phi\phi} Y_{lm}(\hat{\mathbf{n}}) Y_{lm}(\hat{\mathbf{n}'}). \end{aligned} \tag{1.34}$$

Comparing this result to Eq. (1.31) we see that

$$\begin{aligned} C_l^{\phi\phi} &= 16\pi \int_0^{\chi_*} d\chi \int_0^{\chi_*} d\chi' \left(\frac{\chi_* - \chi}{\chi_* \chi} \right) \left(\frac{\chi_* - \chi'}{\chi_* \chi'} \right) \\ &\quad \times \int \frac{dk}{k} j_l(k\chi) j_l(k\chi') \mathcal{P}_\Psi(k, \eta_0 - \chi, \eta_0 - \chi'). \end{aligned} \tag{1.35}$$

This is the theoretical power spectrum for the lensing potential. Defining a linear transfer function

$$\Psi(\mathbf{k}, \eta) = T_\Psi(k; \eta) \mathcal{R}(\mathbf{k}), \tag{1.36}$$

where $\mathcal{R}(k)$ is the primordial comoving curvature perturbation, we can write:

$$C_l^{\phi\phi} = 16\pi \int \frac{dk}{k} \mathcal{P}_\mathcal{R}(k) \left[\int_0^{\chi_*} d\chi T_\Psi(k; \eta_0 - \chi) j_l(k\chi) \left(\frac{\chi_* - \chi'}{\chi_* \chi'} \right) \right]^2. \tag{1.37}$$

This power spectrum can be computed easily along with other CMB power spectra using Boltzmann codes such as CAMB (Lewis et al., 2000).

1.2.2 The lensed CMB power spectra

The lensed temperature $\tilde{T}(\hat{\mathbf{n}})$ is a remapping of the the unlensed temperature $T(\hat{\mathbf{n}})$. On the flat sky, this looks like $\tilde{T}(\mathbf{x}) = T(\mathbf{x}') = T(\mathbf{x} + \nabla\phi)$ and it can be series expanded to

$$T(\mathbf{x} + \nabla\phi) \approx T(\mathbf{x}) + \nabla^a \phi(\mathbf{x}) \nabla_a T(\mathbf{x}) + \frac{1}{2} \nabla^a \phi(\mathbf{x}) \nabla^b \phi(\mathbf{x}) \nabla_a \nabla_b T(\mathbf{x}) + \cdots \tag{1.38}$$

We can write the flat sky Fourier expansion of the lensing potential as

$$\phi(\mathbf{x}) = \int \frac{d^2\mathbf{l}}{2\pi} \phi(\mathbf{l}) e^{i\mathbf{l}\cdot\mathbf{x}} \tag{1.39}$$

and then take the $\mathbf{x}$ derivatives of Eq. (1.7) and Eq. (1.39) respectively:

$$\nabla T(\mathbf{x}) = i \int \frac{d^2\mathbf{l}}{2\pi} \mathbf{l} T(\mathbf{l}) e^{i\mathbf{l}\cdot\mathbf{x}}, \tag{1.40}$$

$$\nabla \phi(\mathbf{x}) = i \int \frac{d^2\mathbf{l}}{2\pi} \mathbf{l} \phi(\mathbf{l}) e^{i\mathbf{l}\cdot\mathbf{x}}. \tag{1.41}$$

Taking the Fourier transform of Eq. (1.38) gives to second order in ϕ:

$$\begin{aligned} \tilde{T}(\mathbf{l}) &\approx T(\mathbf{l}) - \int \frac{d^2\mathbf{l}'}{2\pi} \mathbf{l}' \cdot (\mathbf{l}-\mathbf{l}') \phi(\mathbf{l}-\mathbf{l}') T(\mathbf{l}') \\ &\quad -\frac{1}{2} \int \frac{d^2\mathbf{l}_1}{2\pi} \int \frac{d^2\mathbf{l}_2}{2\pi} \mathbf{l}_1 \cdot [\mathbf{l}_1 + \mathbf{l}_2 - \mathbf{l}] \mathbf{l}_1 \cdot \mathbf{l}_2 T(\mathbf{l}_1) \phi(\mathbf{l}_2) \phi^*(\mathbf{l}_1 + \mathbf{l}_2 - \mathbf{l}). \end{aligned} \tag{1.42}$$

CMB lensing is isotropic since it just moves points around on the sky, so the nth moment of the temperature at any given point is unchanged under lensing on average. (Note that for CMB power spectra homogeneity of the gravitational potential is assumed, but it is the orthogonality of the spherical harmonics which gives the delta function due to isotropy). Therefore the lensed temperature power spectrum is also diagonal:

$$\langle \tilde{T}(\mathbf{l}) \tilde{T}^*(\mathbf{l}') \rangle = \delta(\mathbf{l}-\mathbf{l}') \tilde{C}_l^{TT}, \tag{1.43}$$

(the T-ϕ correlation is small on intermediate and small scales). We can use Eq. (1.42) to write down an expression for the lensed temperature power spectrum $\tilde{C}_l^{TT}$. Neglecting the T-ϕ correlation since it is small and remembering that $\phi(\mathbf{l}) = \phi^*(-\mathbf{l})$, we obtain

$$\tilde{C}_l^{TT} \approx (1 - l^2 R^\phi) C_l^{TT} + \int \frac{d^2\mathbf{l}'}{(2\pi)^2} [\mathbf{l}' \cdot (\mathbf{l}-\mathbf{l}')]^2 C_{|\mathbf{l}-\mathbf{l}'|}^{\phi\phi} C_{l'}^{TT} \tag{1.44}$$

where

$$R^\phi \equiv \frac{1}{2} \langle |\nabla \phi|^2 \rangle = \frac{1}{4\pi} \int \frac{dl}{l} l^4 C_l^{\phi\phi}. \tag{1.45}$$

The situation is analogous but slightly more complicated for the polarization observables. The re-mapping of polarization due to lensing is written via the lensed polarization tensor: $\tilde{P_{ab}}(\mathbf{x}) = P_{ab}(\mathbf{x}') = P_{ab}(\mathbf{x} + \nabla\phi)$ and it can be series expanded to

$$P_{ab}(\mathbf{x} + \nabla\phi) \approx P_{ab}(\mathbf{x}) + \nabla^c \phi(\mathbf{x}) \nabla_c P_{ab}(\mathbf{x}) + \frac{1}{2} \nabla^c \phi(\mathbf{x}) \nabla^d \phi(\mathbf{x}) \nabla_c \nabla_d P_{ab}(\mathbf{x}) + \cdots \tag{1.46}$$

In the absence of tensor modes the primordial B mode is zero. We are mostly interested in the unlensed E mode which lensing converts into B mode, and so we can take the unlensed B mode $B(\mathbf{l}) = 0$. The harmonic expansion gives

$$\begin{aligned} \tilde{E}(\mathbf{l}) \pm i\tilde{B}(\mathbf{l}) &\approx E(\mathbf{l}) - \int \frac{d^2\mathbf{l}'}{2\pi} \mathbf{l}' \cdot (\mathbf{l}-\mathbf{l}') e^{\pm 2i(\varphi_{\mathbf{l}'} - \varphi_{\mathbf{l}})} \phi(\mathbf{l}-\mathbf{l}') E(\mathbf{l}') \\ &\quad -\frac{1}{2} \int \frac{d^2\mathbf{l}_1}{2\pi} \frac{d^2\mathbf{l}_2}{2\pi} e^{\pm 2i(\varphi_{\mathbf{l}'} - \varphi_{\mathbf{l}})} \mathbf{l}_1 \cdot [\mathbf{l}_1 + \mathbf{l}_2 - \mathbf{l}] \cdot \mathbf{l}_2 E(\mathbf{l}_1) \phi(\mathbf{l}_2) \phi^*(\mathbf{l}_1 + \mathbf{l}_2 - \mathbf{l}). \end{aligned} \tag{1.47}$$

To lowest order in $C_l^{\phi\phi}$ the polarization lensed power spectra are:

$$\tilde{C}_l^{EE} = (1 - l^2 R^\phi) C_l^{EE} + \int \frac{d^2\mathbf{l}'}{(2\pi)^2} [\mathbf{l}' \cdot (\mathbf{l} - \mathbf{l}')]^2 C^{\phi\phi}_{|\mathbf{l}-\mathbf{l}'|} C^{EE}_{\mathbf{l}'} \cos^2 2(\varphi_{\mathbf{l}'} - \varphi_{\mathbf{l}}), \tag{1.48}$$

$$\tilde{C}_l^{BB} = \int \frac{d^2\mathbf{l}'}{(2\pi)^2} [\mathbf{l}' \cdot (\mathbf{l} - \mathbf{l}')]^2 C^{\phi\phi}_{|\mathbf{l}-\mathbf{l}'|} C^{EE}_{\mathbf{l}'} \sin^2 2(\varphi_{\mathbf{l}'} - \varphi_{\mathbf{l}}). \tag{1.49}$$

The Taylor expansion is accurate when the thing that it is expanded around, in our case α, is small. Therefore on scales where $l \sim \alpha$ this approximation breaks down, and the Taylor expansion is not very accurate for the lensed power spectra. A better technique is to write down the lensed power spectra in terms of lensed correlation functions, a method which is used in Chapter 4. However, since only relative deflections are important, the Taylor expansion does do quite well in many cases.

1.2.3 Lensing reconstruction

Assuming isotropy, we have seen that harmonics with different $\mathbf{l}$ are uncorrelated (e.g. Eq. (1.4), Eq. (1.12), Eq .(1.13), Eq .(1.14) and Eq .(1.33)). However, for some fixed lensing potential the sky we observe is not isotropic and contains off-diagonal elements in the covariance matrix. We can exploit these off-diagonal terms to build an estimator for the lensing potential. The optimal way to reconstruct the lensing potential would be to use a full maximum likelihood based analysis (Hirata & Seljak, 2003a). However, in practice this is computationally expensive and the quadratic estimator is used instead. For the temperature, we use Eq. (1.38), the series expansion in the deflection, to write down the 2-point function of the lensed temperature averaged over the CMB:

$$\begin{aligned} \langle \tilde{T}(\mathbf{l}) \tilde{T}(\mathbf{l} - \mathbf{L}) \rangle_{CMB} &= \delta(\mathbf{l}) C_l^{TT} - \int \frac{d^2\mathbf{l}'}{2\pi} [\mathbf{l}' \cdot (\mathbf{l} - \mathbf{l}') \phi(\mathbf{l} - \mathbf{l}') \langle T(\mathbf{l}') T^*(\mathbf{l} - \mathbf{L}) \rangle \\ &\quad + \mathbf{l}' \cdot (\mathbf{l} - \mathbf{L} - \mathbf{l}') \phi^*(\mathbf{l} - \mathbf{L} - \mathbf{l}') \langle T(\mathbf{l}) T^*(\mathbf{l}') \rangle] + \mathcal{O}(\phi^2) \\ &= \delta(\mathbf{L}) C_l^{TT} + \frac{1}{2\pi} [(\mathbf{L} - \mathbf{l}) \cdot \mathbf{L} C^{TT}_{|\mathbf{l}-\mathbf{L}|} + \mathbf{l} \cdot \mathbf{L} C_l^{TT}] \phi(\mathbf{L}) + \mathcal{O}(\phi^2). \end{aligned} \tag{1.50}$$

The $\phi(\mathbf{L} = 0)$ mode has zero gradient and is unobservable. However, the $\mathbf{L} \neq 0$ probes the lensing potential and we use a weighted average of the off-diagonal terms to construct the quadratic estimator

$$\hat{\phi}(\mathbf{L}) \equiv N(\mathbf{L}) \int \frac{d^2\mathbf{l}}{2\pi} \tilde{T}(\mathbf{l}) \tilde{T}^*(\mathbf{l} - \mathbf{L}) W(\mathbf{l}, \mathbf{L}). \tag{1.51}$$

Here $N(\mathbf{L})$ is a normalisation function and $W(\mathbf{l}, \mathbf{L})$ is a weighting which we can optimise. For an unbiased estimator $\langle \hat{\phi}(\mathbf{l}) \rangle_{CMB} = \phi(\mathbf{l})$ and so the normalisation is

$$N^{-1}(\mathbf{L}) = \int \frac{d^2\mathbf{l}}{(2\pi)^2} [(\mathbf{L} - \mathbf{l}) \cdot \mathbf{L} C^{TT}_{|\mathbf{l}-\mathbf{L}|} + \mathbf{l} \cdot \mathbf{L} C_l^{TT}] W(\mathbf{l}, \mathbf{L}). \tag{1.52}$$

Now we would like to choose $W(\mathbf{l},\mathbf{L})$ to maximise signal to noise. The variance is given by $\langle|\hat{\phi}(\mathbf{L})-\phi(\mathbf{L})|^2\rangle \sim \langle|\hat{\phi}(\mathbf{L})|^2\rangle$ therefore:

$$\langle\hat{\phi}^*(\mathbf{L})\hat{\phi}(\mathbf{L}')\rangle = \delta(\mathbf{L}-\mathbf{L}')2N(\mathbf{L})^2\int\frac{d^2\mathbf{l}}{(2\pi)^2}C_l^{\rm obs}C_{|\mathbf{l}-\mathbf{L}|}^{\rm obs}[W(\mathbf{l},\mathbf{L})]^2+\mathcal{O}(\phi^2), \tag{1.53}$$

where $C_l^{\rm obs}=\tilde{C}_l^{TT}+N_l$ where N_l is the instrumental noise. Minimising this variance gives a weighting of

$$W(\mathbf{l},\mathbf{L})=\frac{\mathbf{l}\cdot\mathbf{L}C_l^{TT}}{C_l^{\rm obs}C_{|\mathbf{l}-\mathbf{L}|}^{\rm obs}}. \tag{1.54}$$

The analogously derived equations for the polarization quadratic estimator are given in Chapter 2.

1.3 Non-Gaussianity

For zero-mean Gaussian random fields the 2-point correlation function contains all of the statistical information since higher order connected correlators of the Gaussian vanish. For example, if we take the 3-point correlation of the temperature harmonic coefficients T_{lm} analogously to the 2-point function of Eq. (1.4)

$$\langle T_{lm}T_{l'm'}T_{l''m''}\rangle = 0, \tag{1.55}$$

which evaluates to zero because the mean of the Gaussian $\langle T_{lm}\rangle = 0$. The term 'non-Gaussianity' refers to anything which is not Gaussian distributed and therefore contains higher-order connected correlation functions. In cosmology we expect that deviations from slow roll inflation could cause non-Gaussianities in the inflaton field. Measurements of non-Gaussianity in the CMB and Large-Scale Structure can be traced back to non-Gaussianities in the inflaton field, with the potential to differentiate observationally between different inflationary models. The 3-point correlation function is known as the bispectrum and corresponds to a skewness in the distribution. The 4-point correlation function is known as the trispectrum and corresponds to a kurtosis (squashing/stretching) of the Gaussian distribution.

Figure 1.6 shows schematically how non-Gaussianities in the gravitational potential Φ correspond to non-zero 3- and 4-point correlation functions (skewness and kurtosis) in the distribution. During matter domination, the gravitational potential Φ (evaluated in the Newtonian gauge) can be related to the gauge invariant primordial curvature perturbation ζ by

$$\Phi = -\frac{3}{5}\zeta. \tag{1.56}$$

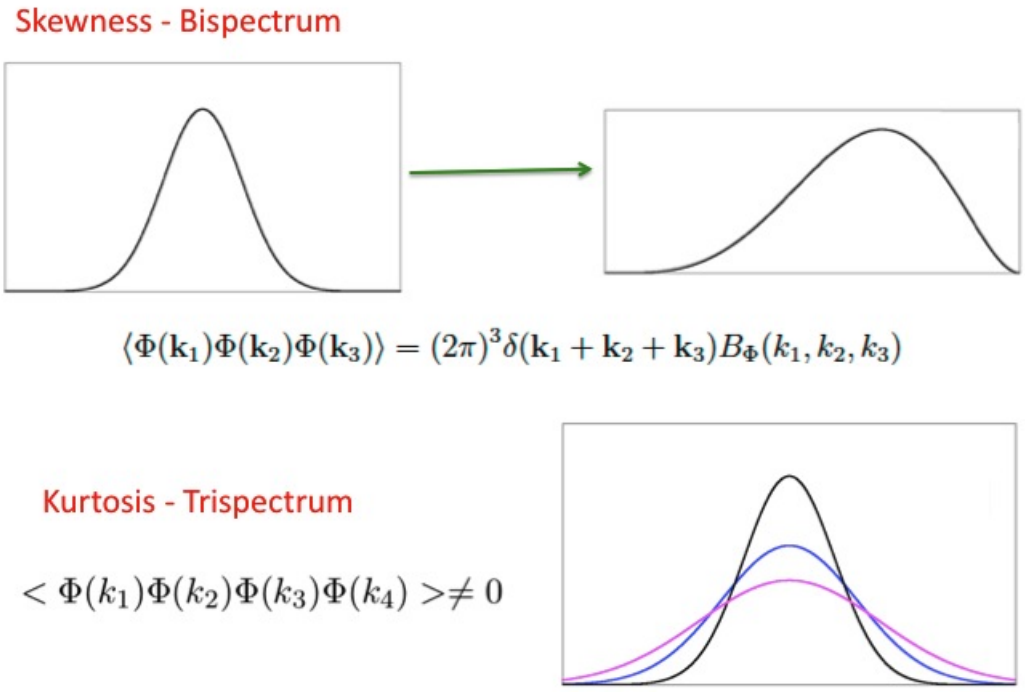

Figure 1.6: A schematic view of the 3- and 4-point correlation functions of a non-Gaussian field.

In practice, we do not measure Φ or ζ. The transfer function tells us how to evolve primordial inflationary quantities into observables. For example, the T_{lm} of the temperature anisotropy is related to ζ via the transfer function $\delta_l(k)$ by

$$T_{lm} = 4\pi(-i)^l \int d^3\mathbf{k}\delta_l(k)\zeta(\mathbf{k})Y_{lm}(\hat{\mathbf{k}}). \tag{1.57}$$

This relation can be used to relate the primordial bispectrum to the CMB bispectrum. The primordial bispectrum in terms of the gravitational potentials is defined as

$$\langle \Phi(\mathbf{k}_1)\Phi(\mathbf{k}_2)\Phi(\mathbf{k}_3)\rangle = (2\pi)^3\delta(\mathbf{k}_1+\mathbf{k}_2+\mathbf{k}_3)B_\Phi(k_1,k_2,k_3). \tag{1.58}$$

The bispectrum is a function of three k modes which must obey the triangle condition. One limit of the bispectrum which is interesting to study is the local bispectrum also known as the squeezed limit. In this limit there are two small-scale modes comparable in size and one large-scale mode $k_1 \sim k_2 >> k_3$. In k-space this looks like squeezed triangles and physically corresponds to a modulation of small-scale power by the large-

scale mode. Figure 1.7 shows the the squeezed triangle and the modulation of small power by a large-scale mode.

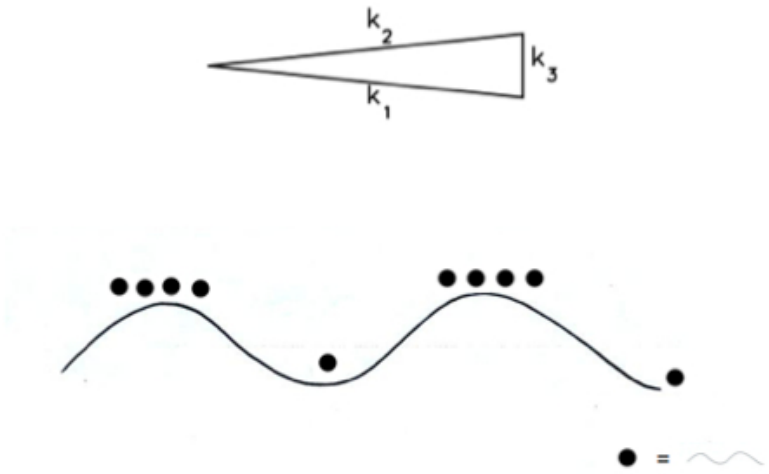

Figure 1.7: Above: The bispectrum triangle condition in the squeezed limit. Below: A real space representation of a large-scale modulation of small-scale power. Each dot represents some small-scale power.

In this limit the non-Gaussian gravitational potential Φ_{NG} can be expressed via a Gaussian potential Φ_G using:

$$\Phi_{NG} = \Phi_G + f_{NL}\Phi_G^2 - \langle\Phi_G^2\rangle. \tag{1.59}$$

This parameterises the level of non-Gaussianity in the squeezed bispectrum via the parameter f_{NL}. The bispectrum can then be written down in terms of the 2-point correlation functions of the gravitational potential in k space:

$$B_\Phi(k_1, k_2, k_3) = 2f_{NL}[P_\Phi(k_1)P_\Phi(k_2) + P_\Phi(k_1)P_\Phi(k_3) + P_\Phi(k_1)P_\Phi(k_3)], \tag{1.60}$$

where

$$\langle\Phi(\mathbf{k}_1)\Phi(\mathbf{k}_2)\rangle = \delta(\mathbf{k}_1 + \mathbf{k}_2)P_\Phi(k_1). \tag{1.61}$$

1.4 Large-Scale Structure

Like the CMB, the Large-Scale Structure (LSS) of the universe is also seeded by the quantum fluctuations in the inflationary potential via gravitational collapse after reheating. An over-dense region will have a larger gravitational potential than an under-dense region causing gravitational collapse in the over-dense regions but not in the under-dense

regions. In the early universe this collapse competes with radiation pressure from photons and neutrinos, whilst in the later universe it competes with the expansion due to dark energy. Therefore, measurements of the LSS will yield information on the neutrino mass sum $\sum m_\nu$ and the dark energy Ω_Λ as well as galaxy clustering properties. However, unlike the CMB the LSS is highly non-linear which presents challenges for measurement. On the other hand, the LSS contains three-dimensional information (it can be measured by different tracers at varying redshifts), and is therefore extremely valuable for cosmology.

To measure the LSS, we can survey various tracers. The dominant contribution of energy density of matter is in CDM and we expect the baryonic matter in the universe to reside in the potential wells of the underlying CDM distribution. Therefore, by measuring the clustering properties of galaxies and clusters of galaxies (as well as voids) we can probe the underlying matter distribution. However, galaxies reside in dark matter halos and the clustering of the halos is different to the clustering of the dark matter distribution itself. This leads to a bias between the power spectrum of the tracer and the power spectrum of the CDM. This is called the 'galaxy bias' and is an active field of research. The galaxy bias is scale dependent, redshift dependent and tracer dependent. The full properties of the the galaxy bias are only just beginning to be understood, and once under control, will give us a much better handle on many cosmological observables. (E.g. see Dekel & Lahav (1999) for a discussion of non-linearity and Smith et al. (2007) for a discussion of scale dependence). A simple formulation of the galaxy bias is to assume a linear relation between the galaxy density field δ_g and the underlying matter density field due to the CDM δ_m:

$$\delta_g(\mathbf{x}) = b\delta_m(\mathbf{x}). \tag{1.62}$$

The power spectrum relation then becomes:

$$P_g(\mathbf{k}) = b^2 P_m(\mathbf{k}). \tag{1.63}$$

The gravitational collapse of over dense regions of the CDM field competes with the expansion of the universe, and dark matter haloes (gravitationally collapsed clumps of dark matter) only form when the CDM density contrast is above a critical threshold. Therefore, where there is one dark matter halo, we expect there to be more, since the local area is probably an over dense region. This leads to the dark matter haloes being more strongly clustered than the underlying CDM because haloes will only form in the peaks of a Gaussian-assumed underlying CDM field. Galaxies will form in haloes, causing the bias to also appear in the galaxy power spectrum which we measure from observations.

Fig. 1.8 shows a cartoon of why the dark matter haloes tend to form in clusters via the high peak model of bias by Kaiser (1984). Theoretically, it is simplest to imagine a linearly extrapolated growth function of the perturbations modelled by spherical collapse. In this picture it is relatively simple to predict the power spectrum of peaks above some threshold using Gaussian statistics, and the threshold density contrast required for haloes to form (via non-linear gravitational collapse) is $\delta_m^{\rm threshold} = 1.686$ (see e.g. Liddle & Lyth (2000) for a derivation). Under these assumptions the halo mass function can be calculated, which describes the abundance of haloes as a function of mass and redshift. In practice, we have to use N-body simulations to simulate the halo mass function and see if it fits with our theory. In the picture described, we expect haloes and therefore galaxies to be more clustered than the underlying CDM distribution, hence usually $b > 1$. The rarer the object we observe, the more biased we expect it to be. For example the largest galaxy clusters we observe are also the most biased. In contrast, as a function of time the bias is decreasing. The older the universe becomes, the more regions will have crossed the density threshold for collapse. This means that lower mass and lower redshift objects are expected to be less biased. For a comprehensive review see Bernardeau et al. (2002).

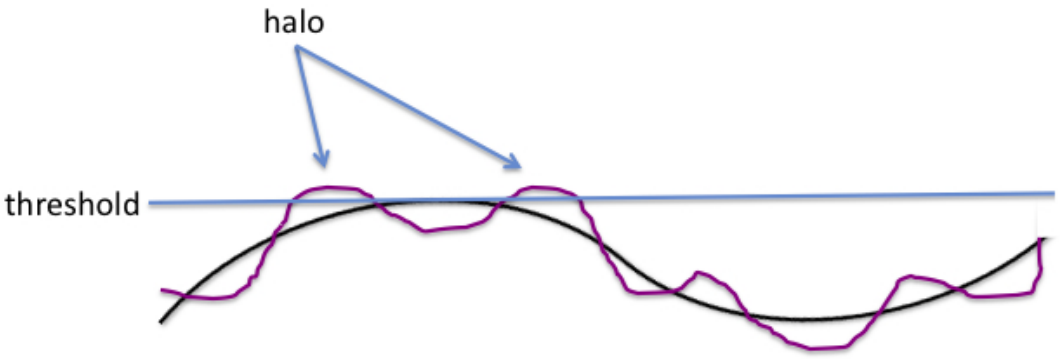

Figure 1.8: A cartoon showing perturbations in the CDM density field. Smaller perturbations (shown in purple) are modulated by the large-scale mode (shown in black). In the vicinity of the large-scale mode peak, the overall density contrast is largest and more likely to exceed the critical density for gravitational collapse (shown by the blue line). Therefore dark matter haloes are more likely to form near other dark matter haloes, causing clustering and the observed galaxy bias. Arrows show those regions which exceed the threshold density and form haloes. (Kaiser, 1984)

Chapter 2

CMB Lensing Reconstruction from Polarization

2.1 Introduction

The contents of this chapter are based on work presented in the paper Pearson et al. (2014) and represent work done by the author in collaboration with Blake Sherwin and Antony Lewis. In Chapter 1 we saw that the photons of the CMB are deflected by gravitational potentials along the line of sight as they travel from the surface of last scattering to our telescopes. While the surface brightness of the CMB is preserved by the remapping of individual photons on the sky, this remapping alters the statistics of the observed CMB anisotropies. For example, CMB lensing induces lensing B modes as well as non-Gaussianity in the data (for reviews see Lewis & Challinor (2006); Hanson et al. (2010)). It is important to understand the CMB lensing so that its effect can be removed and primordial physics can be measured from the observed maps. The CMB lensing signal is also of great interest for cosmology in itself, since it traces structure from the surface of last scattering until today and is thus a powerful probe of the matter distribution. The particular distribution of matter in our universe introduces off-diagonal covariances between modes in the CMB observables, and these can be used to reconstruct the lensing potential (Hu & Okamoto, 2002).

To reconstruct the lensing potential, a full maximum likelihood based analysis is most optimal (Hirata & Seljak, 2003b). However this is computationally challenging, and a leading-order quadratic estimator approximation is usually used instead (Hu & Okamoto, 2002; Okamoto & Hu, 2003). These estimators are nearly optimal for current-generation experiments once generalised for partial sky coverage and inhomogeneous noise (Hirata &

Seljak, 2003a,b; Hanson & Lewis, 2009; Hanson et al., 2010). On the cut sky slightly less optimal but simpler estimators can also be used which use apodized sky maps without the numerically-expensive full inverse-variance weighting required for the perturbatively optimal estimators. We focus on these simpler estimators, as used by various current-generation ground-based experiments, as described in section 2.1.1.

The temperature (TT) quadratic estimator (consisting of a quadratic combination of two temperature modes) has been used to measure the CMB lensing potential to high significance (Das et al., 2011, 2013; van Engelen et al., 2012), most recently at more than 20σ by the Planck collaboration (Ade et al., 2013f). The signal-to-noise ratio for lensing reconstruction from CMB polarization data is expected to be much better in the future, because polarization lensing is not limited by cosmic variance, with B modes on small scales expected to be vanishingly small on the unlensed sky. First examples of CMB lensing reconstruction from polarization data use SPT or POLARBEAR data in cross- or auto-correlation (Hanson et al., 2013; Ade et al., 2013b,a), based on CMB polarization observations on small patches of the sky at high resolution.

In this work we investigate the ability of such current and next-generation polarization observations to measure the CMB lensing potential power spectrum. We begin by studying periodic boundary conditions for the EE and EB quadratic estimators in section 2.2. We show that the known $N^{(0)}$ and $N^{(1)}$ power spectrum biases are sufficient to model the reconstructed lensing potential power spectrum. Since no experiment can actually measure the full sky, we also consider the effect of using cut sky maps from small patches of sky. Because the mapping between the observed polarization Stokes parameters (Q and U) and the physical E and B polarization fields is non-local (involving derivatives), on a patch of the sky E modes can leak into B modes. This provides an additional complication for lensing reconstruction, and could, if not mitigated, significantly impair the use of B modes to reconstruct the lensing field. In section 2.1.2 we outline the effect and review the 'pure' B mode construction that can be used to project the observed data into clean B modes that we then incorporate into our lensing reconstruction pipeline. In section 2.3 we test the EE and EB quadratic estimators when applied to $4.5^\circ \times 4.5^\circ$ patches of sky with non-periodic boundaries. We compare the performance of the EB estimator when incorporating the pure-B mode filter to the naive reconstruction with a simple apodizing window. We also assess the magnitude of any additional biases in the cut sky case.

2.1.1 CMB Lensing

Since we are mainly interested in small patches of sky for this work, we will use the flat-sky approximation, following mostly the notation of Hu & Okamoto (2002), but switching the labelling convention of lensed and unlensed fields. Recall from Chapter 1 that the temperature T at a position $\mathbf{x}$ on the plane of the sky is expanded into harmonics as

$$T(\mathbf{x}) = \int \frac{d^2\mathbf{l}}{2\pi} T(\mathbf{l}) e^{i\mathbf{l}\cdot\mathbf{x}}, \tag{2.1}$$

and the observed Q and U Stokes parameters are expressed in terms of E and B polarization modes as

$$[Q \pm iU](\mathbf{x}) = -\int \frac{d^2\mathbf{l}}{2\pi} [E(\mathbf{l}) \pm iB(\mathbf{l})] e^{\pm 2i\varphi_l} e^{i\mathbf{l}\cdot\mathbf{x}}, \tag{2.2}$$

where the plane wave vector $\mathbf{l}$ is the flat-sky analogue of the full-sky spherical harmonic lm, and $\cos\varphi_l = \hat{\mathbf{x}}\cdot\hat{\mathbf{l}}$ (where $\hat{\mathbf{x}}$ is a unit vector along the x-direction). The fields at last scattering are re-mapped by the lensing as

$$\tilde{T}(\mathbf{x}) = T(\mathbf{x} + \alpha(\mathbf{x})), \qquad [\tilde{\mathbf{Q}} \pm \mathbf{i}\tilde{\mathbf{U}}](\mathbf{x}) = [\mathbf{Q} \pm \mathbf{iU}](\mathbf{x} + \alpha(\mathbf{x})), \tag{2.3}$$

where the tilde denotes lensed fields and $\alpha(\mathbf{x})$ is the lensing deflection field. The deflection can be expressed as $\alpha = \boldsymbol{\nabla}\phi$, where in a flat FRW universe the lensing potential ϕ is given by

$$\phi(\mathbf{x}) = -2\int_0^{\chi_*} d\chi \frac{(\chi_* - \chi)}{\chi\chi_*} \Psi(\chi\hat{\mathbf{n}}_\mathbf{x}), \tag{2.4}$$

as derived in section 1.2.1. Here χ is the comoving distance along the line of sight, and χ_* is the distance to the last scattering surface, and $\Psi(\chi\hat{\mathbf{n}}_\mathbf{x})$ is the (Weyl) gravitational potential at the photon location along the line of sight in direction $\hat{\mathbf{n}}_\mathbf{x}$ on the sky.

Lensing of the CMB can be measured from the response of the lensed two point correlation function to the lensing potential. We have multiple fields, so in general have multiple quadratic combinations to consider, $\tilde{X}_i(\mathbf{l}_1)\tilde{X}_j(\mathbf{l}_2)$, where $\tilde{X}_i$ could be T, E or B. Considering the lensing potential ϕ to be fixed, averaging over all other modes and neglecting correlations between the lensing potential and CMB, to linear order in ϕ

$$\langle \tilde{X}_i(\mathbf{l}_1)\tilde{X}_j(\mathbf{l}_2)\rangle_\phi \approx \int d\mathbf{L}' \left\langle \frac{\delta}{\delta\phi(\mathbf{L}')} \left(\tilde{X}_i(\mathbf{l}_1)\tilde{X}_j(\mathbf{l}_2)\right)\right\rangle \phi(\mathbf{L}') = \frac{1}{2\pi} f_{ij}(\mathbf{l}_1, \mathbf{l}_2)\phi(\mathbf{L}), \tag{2.5}$$

where $\mathbf{l}_1 + \mathbf{l}_2 = \mathbf{L}$ and $\mathbf{L} \neq 0$. Here the response functions f_{ij} are defined as the average linear response to a lensing mode $\phi(\mathbf{L})$ (Lewis, 2011; Lewis et al., 2011)

$$\left\langle \frac{\delta}{\delta\phi(\mathbf{L})} \left(\tilde{X}_i(\mathbf{l}_1)\tilde{X}_j(\mathbf{l}_2)\right)\right\rangle = \frac{1}{2\pi}\delta(\mathbf{l}_1 + \mathbf{l}_2 - \mathbf{L}) f_{ij}(\mathbf{l}_1, \mathbf{l}_2). \tag{2.6}$$

For a result to leading order in the particular mode $\phi(\mathbf{L})$, the expectation can be evaluated over all the fields (the unlensed CMB, and non-zero lensing modes that are also present); the result is then proportional to a delta-function by statistical homogeneity. To zeroth order in the lensing potential the response functions f_{ij} are given by Hu & Okamoto (2002), however because the lensing is a substantial signal, to get the normalisation right higher order corrections must be included (Hanson et al., 2011), corresponding to including the contribution of other lensing modes to the covariance[1]. Explicit exact expressions (for Gaussian unlensed fields) are given in Lewis et al. (2011), and can be approximated quite accurately (non-perturbatively) by using the lensed CMB power spectra in place of the unlensed ones in the results of Hu & Okamoto (2002): to good approximation when we look for a mode $\phi(\mathbf{L})$, the change induced on the sky depends on how it affects the lensed CMB, where the lensing effect is dominated by lensing from other modes that are also present. In the case of polarization the main non-perturbative effect that should be modelled is the substantial effect of lensing on EE. There are also additional corrections of $\mathcal{O}(C_l^{BB})$, but these are much smaller (just including the lensed C_l^{BB} does not include all the terms of equivalent order (Lewis et al., 2011)). For current observations corrections of $\mathcal{O}(C_l^{BB}/C_l^{EE})$ can probably be safely neglected; further perturbative tests of the lensed-C_l approximation are given in Anderes (2013).

Weighting functions $W(\mathbf{l}_1, \mathbf{l}_2)$ can be used to sum the quadratic combinations $\tilde{X}_i(\mathbf{l}_1)\tilde{X}_j(\mathbf{l}_2)$ so that the deflection field estimators are

$$\hat{\alpha}_{ij}(\mathbf{L}) = \frac{A_{ij}(L)}{L}\int \frac{d^2\mathbf{l}_1}{2\pi}\tilde{X}_i(\mathbf{l}_1)\tilde{X}_j(\mathbf{l}_2)W_{ij}(\mathbf{l}_1,\mathbf{l}_2), \tag{2.7}$$

where $\mathbf{l}_1 + \mathbf{l}_2 = \mathbf{L}$, and $A_{ij}(L)$ is a normalisation that makes the estimator unbiased when averaged over other modes:

$$A_{ij}(L) = L^2\left[\int \frac{d^2\mathbf{l}_1}{(2\pi)^2} f_{ij}(\mathbf{l}_1,\mathbf{l}_2)W_{ij}(\mathbf{l}_1,\mathbf{l}_2)\right]^{-1}. \tag{2.8}$$

In Chapter 1 we introduced the quadratic estimator for the temperature reconstruction of the lensing potential in Eq. (1.51). In this case, the normalisation is slightly different, since we are estimating the lensing deflection, rather than the lensing potential. Figure 2.1 shows an example of one realisation of the deflection field and its reconstruction using $\hat{\alpha}_{EB}$. The reconstruction shows the features of the original, but also has a lot of small-scale noise, which is the manifestation of the $N^{(0)}$ bias discussed below.

[1] An $\mathcal{O}(C^{\phi\phi})$ correction to the power spectrum normalisation, giving a total error $\mathcal{O}((C^{\phi\phi})^2)$, and hence an $N^{(2)}$ if neglected (Hanson et al., 2011).

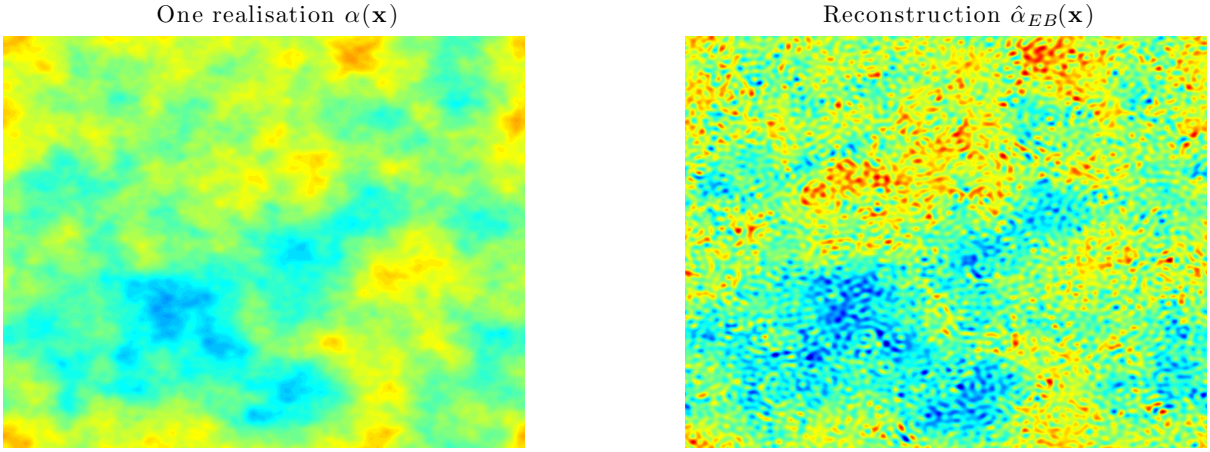

Figure 2.1: Left: A real space map of one realisation of the lensing deflection on a $9^\circ \times 9^\circ$ patch with periodic boundaries. Right: The reconstruction of the lensing deflection in the left panel using $\hat{\alpha}_{EB}$, for the fiducial noise and resolution used in this work ($\triangle_p = 4\mu$Karcmin and $\sigma_{FWHM} = 1.4$arcmin, see secion 2.2 for details).

We can construct a naive estimator for the lensing power spectrum by measuring the power spectrum of the lensing deflection estimator. On the full sky this has an expectation value equal to the lensing potential power spectrum added to 'noise' bias terms:

$$\langle \hat{\alpha}^*_{ij}(\mathbf{L})\hat{\alpha}_{pq}(\mathbf{L}')\rangle = \delta(\mathbf{L}-\mathbf{L}')\left[C^{dd}_L + N^{(0)}_{ijpq}(L) + N^{(1)}_{ijpq}(L)\right], \tag{2.9}$$

to linear order in $C^{\phi\phi}_L$. Using the $\hat{\alpha}_{EE}(\mathbf{L})$ and $\hat{\alpha}_{EB}(\mathbf{L})$ quadratic estimators, there are 3 different ways to reconstruct the lensing power spectrum: $\langle \hat{\alpha}^*_{EE}(\mathbf{L})\hat{\alpha}_{EE}(\mathbf{L}')\rangle$, $\langle \hat{\alpha}^*_{EB}(\mathbf{L})\hat{\alpha}_{EB}(\mathbf{L}')\rangle$ and $\langle \hat{\alpha}^*_{EB}(\mathbf{L})\hat{\alpha}_{EE}(\mathbf{L}')\rangle$. The Gaussian $N^{(0)}_{ijpq}(L)$ disconnected term is given by (Hu & Okamoto, 2002)

$$\begin{aligned} N^{(0)}_{ijpq}(L) &= \frac{A^{ij}(L)A^{pq}(L)}{L^2}\int d^2\mathbf{l}_1 W_{ij}(\mathbf{l}_1,\mathbf{l}_2) \\ &\quad\times\left[W_{pq}(\mathbf{l}_1,\mathbf{l}_2)C^{ip}_{\mathrm{obs},l_1}C^{jq}_{\mathrm{obs},l_2} + W_{pq}(\mathbf{l}_2,\mathbf{l}_1)C^{iq}_{\mathrm{obs},l_1}C^{jp}_{\mathrm{obs},l_2}\right], \end{aligned} \tag{2.10}$$

where $C^{ij}_{\mathrm{obs},l}$ are the total observed lensed CMB power spectra including (isotropic) instrumental noise. In the diagonal case this simplifies to $N^{(0)}_{ijij}(L) = A_{ij}(L)$ for optimised weights. For the $\langle \hat{\alpha}^*_{EB}(\mathbf{L})\hat{\alpha}_{EE}(\mathbf{L}')\rangle$ case $N^{(0)}_{EBEE} = 0$.

The $N^{(0)}$ bias corresponds to random fluctuations in the noise and un-deflected CMB happening to look like lensing, and has contributions from both the Gaussian lensed power spectrum and instrumental noise. The $N^{(1)}_{ijpq}(L)$ term (Kesden et al., 2003) is an additional

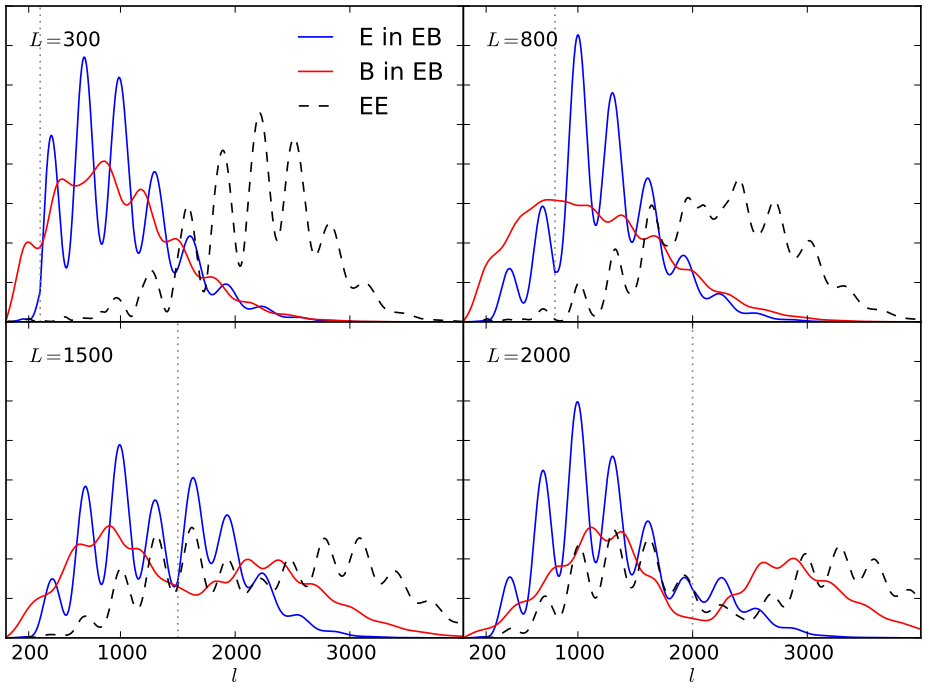

Figure 2.2: Fractional contributions from $E(\mathbf{l})$ and $B(\mathbf{l})$ at $l = |\mathbf{l}|$ to the lensing reconstruction at $L \in \{300, 800, 1500, 2000\}$ (four panels, where in each panel $l = L$ is marked with a dotted line), for the fiducial noise and resolution used in this work ($\triangle_p = 4\mu$Karcmin and $\sigma_{FWHM} = 1.4$arcmin, see secion 2.2 for details). At the lower L the EE reconstruction (dashed lines) is mainly from squeezed shapes with $l \gg L$, however the EB estimator the E and especially B mode signal is important at much lower l (solid lines). Mathematically what is plotted is $A_{ij}(L, l_1) \propto \int l_1 d\varphi_{l_1} f_{ij}(\mathbf{l}_1, \mathbf{l}_2) W_{ij}(\mathbf{l}_1, \mathbf{l}_2)$ as a function of l_1, or equivalently for l_2 in the case of the second field in the quadratic estimator, normalised to sum to unity.

variance from first order effects in the lensing power spectrum, given by

$$N^{(1)}_{ijpq}(L) = \frac{A_{ij}(L)A_{pq}(L)}{L^2} \int \frac{d^2\mathbf{l}_1 d^2\mathbf{L}'}{(2\pi)^2} C^{\phi\phi}_{L'} W_{ij}(\mathbf{l}_1, \mathbf{l}_2) \times [f_{ip}(\mathbf{l}_1, \mathbf{l}_3) f_{jq}(\mathbf{l}_2, \mathbf{l}_4) W_{pq}(\mathbf{l}_3, \mathbf{l}_4) + f_{iq}(\mathbf{l}_1, \mathbf{l}_3) f_{jp}(\mathbf{l}_2, \mathbf{l}_4) W_{pq}(\mathbf{l}_4, \mathbf{l}_3)] \quad (2.11)$$

where $\mathbf{l}_1 + \mathbf{l}_2 = \mathbf{L} = -(\mathbf{l}_3 + \mathbf{l}_4)$, $\mathbf{l}_1 + \mathbf{l}_3 = \mathbf{L}' = -(\mathbf{l}_2 + \mathbf{l}_4)$. These expressions show the biases in the power spectrum of the deflection field C^{dd}_l, which is related to the power spectrum of the lensing potential $C^{\phi\phi}_l$ and power spectrum of the lensing convergence $C^{\kappa\kappa}_l$ by $C^{\kappa\kappa}_l = \frac{l(l+1)}{4} C^{dd}_l = \frac{l^2(l+1)^2}{4} C^{\phi\phi}_l$ on the full sky, and similarly with $l(l+1) \to l^2$ in the flat sky approximation.

Optimal weight functions can easily be derived at lowest order by minimising the Gaussian variance of the estimators (Hu & Okamoto, 2002). In this work we focus on

the polarization quadratic estimators since polarization lensing reconstruction is a novel method which has not been investigated in detail for realistic applications. The full-sky EE and EB quadratic estimators have response functions given by

$$f_{EE}(\mathbf{l}_1,\mathbf{l}_2) = \left[\tilde{C}^{EE}_{l_1}(\mathbf{L}\cdot\mathbf{l}_1) + \tilde{C}^{EE}_{l_2}(\mathbf{L}\cdot\mathbf{l}_2)\right]\cos(2\varphi_{\mathbf{l}_1\mathbf{l}_2}), \tag{2.12}$$

$$f_{EB}(\mathbf{l}_1,\mathbf{l}_2) = \left[\tilde{C}^{EE}_{l_1}(\mathbf{L}\cdot\mathbf{l}) - \tilde{C}^{BB}_{l_2}(\mathbf{L}\cdot\mathbf{l}_2)\right]\sin(2\varphi_{\mathbf{l}_1\mathbf{l}_2}), \tag{2.13}$$

where $\cos\varphi_{\mathbf{l}_1\mathbf{l}_2} = \hat{\mathbf{l}}_1\cdot\hat{\mathbf{l}}_2$ and the optimised weight functions are

$$W_{EE}(\mathbf{l}_1,\mathbf{l}_2) = \frac{f_{EE}(\mathbf{l}_1,\mathbf{l}_2)}{2C^{EE}_{\mathrm{obs},l_1}C^{EE}_{\mathrm{obs},l_2}}, \qquad W_{EB}(\mathbf{l}_1,\mathbf{l}_2) = \frac{f_{EB}(\mathbf{l}_1,\mathbf{l}_2)}{C^{EE}_{\mathrm{obs},l_1}C^{BB}_{\mathrm{obs},l_2}}. \tag{2.14}$$

Here $C^{EE}_{\mathrm{obs},l}$ and $C^{BB}_{\mathrm{obs},l}$ power spectra are the observed E and B mode power spectra, the lensed power spectra plus instrument noise $C^{EE}_{\mathrm{obs},l} = \tilde{C}^{EE}_l + N^{EE}_l$ and $C^{BB}_{\mathrm{obs},l} = \tilde{C}^{BB}_l + N^{BB}_l$. The different trigonometric factors in the response function indicate that the contributions to the estimators come from rather different configurations: the EE estimator has a lot of signal in squeezed shapes with $L \ll l_1, l_2$ and hence $l_1 \sim l_2$, corresponding to reconstructing the large-scale lensing shear and convergence from the effect on the local small-scale power spectrum; however for the EB estimator, $\sin(2\varphi_{\mathbf{l}_1\mathbf{l}_2}) \sim 0$ for $l_1 \sim l_2$, and instead the dominant signal comes from correlating lensing-induced B modes on a scale comparable to the lensing mode. See Fig. 2.2 for the contributions to the lensing signal at various different scales.

Foreground contamination is not considered in this work, although both galactic and extragalactic polarization foregrounds are expected to be present. The quadratic estimator above could be modified to deal with foregrounds by including foreground information as an extra noise contribution in the weight functions.

2.1.2 Cut sky and E-B leakage

The CMB E and B modes are defined as a harmonic transform of the Q and U Stokes parameters without a boundary. In the presence of a boundary (as on cut sky maps), the harmonics are no longer orthogonal, causing power to be leaked from the dominant E mode into the subdominant B mode if they are naively evaluated over only the observed patch of sky. A number of methods have been developed to remove the spurious B mode power originating from non-periodic boundary conditions on small patches of sky, e.g. Lewis et al. (2002); Bunn et al. (2003); Smith (2006); Smith & Zaldarriaga (2007). A clean separation into pure-B modes is effectively optimal for small noise levels where leakage from E is dominating the variance of the contaminated observed B modes. For

intermediate noise levels inverse variance filtering would appropriately down weight the contaminated modes in an optimal way, and a full implementation of a nearly-optimal lensing reconstruction method (Hirata & Seljak, 2003a,b; Hanson & Lewis, 2009) should therefore optimally handle the mixing effect at the expense of a very numerically costly inverse-variance filtering step.

In this work we focus on sub-optimal but simple methods for handling the cut sky as used by some recent ground-based observations, where a window function $W(\mathbf{x})$ is used to apodize the observed area smoothly to zero at the boundaries of the observed region. Pseudo harmonics are defined by directly transforming $W(\mathbf{x})(Q \pm iU)$:

$$[E^{\rm pseudo} \pm iB^{\rm pseudo}](\mathbf{l}) \equiv -\int \frac{d^2\mathbf{x}}{2\pi} W(\mathbf{x})[Q \pm iU](\mathbf{x}) e^{\mp 2i\varphi_l} e^{-i\mathbf{l}\cdot\mathbf{x}}, \tag{2.15}$$

however $B^{\rm pseudo}$ will in general be a mixture of physical E and B modes since $e^{\mp 2i\varphi_l} e^{-i\mathbf{l}\cdot\mathbf{x}}$ are not orthogonal with respect to W. Quantities that depend only on E and B modes can be obtained by choosing a general real window function w that vanishes along with its derivative on the boundary of the observed region and outside. The quantities E_w and B_w defined by

$$E_w \pm iB_w = \int \frac{d^2\mathbf{x}}{2\pi}\, w(\partial_x \mp i\partial_y)^2 (Q \pm iU) = \int \frac{d^2\mathbf{x}}{2\pi} (Q \pm iU)(\partial_x \mp i\partial_y)^2 w \tag{2.16}$$

are then guaranteed to be pure-E and pure-B (Lewis et al., 2002; Bunn et al., 2003). An essentially optimal separation can be performed by using a complete basis of window functions, at the expense of considerable numerical cost. Alternatively Smith & Zaldarriaga (2007) suggest a faster (but suboptimal) method using a set of pure modes obtained by taking $w = l^{-2} W e^{-i\mathbf{l}\cdot\mathbf{x}}$, which reduce to the standard harmonics in the full sky case that $W = 1$ everywhere. Since the small-scale B mode signal is expected to be much smaller than the E modes, the main concern is leakage of E into B rather than vice versa. We therefore only consider the pure-B modes given for a particular choice of window $W(\mathbf{x})$ by

$$B^{\rm pure}(\mathbf{l}) \equiv \frac{1}{2l^2 i} \int \frac{d^2\mathbf{x}}{2\pi} \left[(Q + iU)(\partial_x - i\partial_y)^2 - (Q - iU)(\partial_x + i\partial_y)^2\right] (W e^{-i\mathbf{l}\cdot\mathbf{x}}). \tag{2.17}$$

These modes are numerically simple to compute, and given explicitly by expanding the derivatives:

$$\begin{aligned} B^{\rm pure}(\mathbf{l}) \;=\; & \int \frac{d^2\mathbf{x}}{2\pi} e^{-i\mathbf{l}\cdot\mathbf{x}} \Big(\left[\sin(2\varphi_l) Q - \cos(2\varphi_l) U\right] W \\ & + \frac{2i}{l} \left[(Q\partial_y W - U\partial_x W)\cos\varphi_l + (U\partial_y W + Q\partial_x W)\sin\varphi_l\right] \\ & + \frac{1}{l^2} \left[U(\partial_x^2 - \partial_y^2) W - 2Q\partial_x\partial_y W\right] \Big). \end{aligned} \tag{2.18}$$

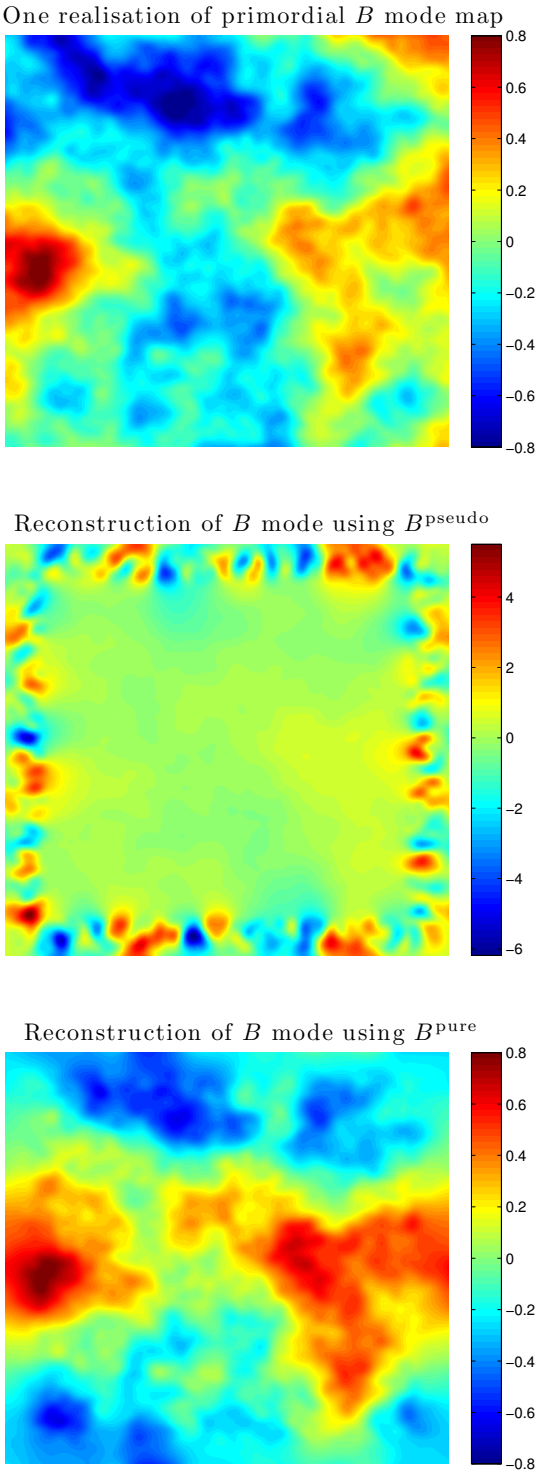

Figure 2.3: One realisation of a B mode map compared to its reconstruction using the $B^{\rm pseudo}$ and $B^{\rm pure}$ estimators. The window used here is that shown in section 2.3 in Fig. 2.5.

Figure 2.3 shows a realisation of a B mode map in real space and the resulting reconstructions using the $B^{\rm pseudo}$ and $B^{\rm pure}$ estimators. The $B^{\rm pseudo}$ reconstruction shows a lot of noise on the boundary, whereas the $B^{\rm pure}$ reconstructs the original well.

The leakage of E modes into B modes is determined by the shape of the window function, with fractionally significant B modes being generated from E modes on a scale comparable to the variation of the window. To the extent that lensing reconstruction is using information only on scales much smaller than the variation of the window, one might expect the impact of the mixing to be modest. However as shown in Fig. 2.2 the EB polarization lensing reconstruction depends on B modes from a very wide range of scales: even large-scale mixing effects are potentially important for EB-reconstruction, even though the EE reconstruction information is mostly coming from very small scales. In section 2.3 we compare the performance of the $EB \times EB$ and $EB \times EE$ lensing power spectrum estimators with and without the projection into pure-B modes, to assess the importance of the mixing effect and the efficiency of using pure-B modes to mitigate it in a straightforward way. Smith & Zaldarriaga (2007) also consider optimization of the window function, but here we just take the window to be a free function that we choose for convenience, so the results are expected to be slightly suboptimal.

2.2 Polarization reconstruction without boundaries

In this section we present results from simulations of the lensing reconstruction on a small patch of sky with periodic boundaries, so there are no issues of E/B mixing. Mock data CMB maps of the Q and U polarization are generated for a $9^\circ \times 9^\circ$ patch of sky with a full width half maximum beam size of $\sigma_{FWHM} = 1.4$arcmin. Each unlensed simulation takes a random realization of theoretical unlensed input power spectra C_l^{EE}, C_l^{BB}. These maps get lensed according to a random realization of a theoretical input power spectrum C_L^{dd}, where the unlensed power spectra and lensing power spectrum are calculated to linear order using CAMB (Lewis et al., 2000) for a ΛCDM cosmology. To simulate the lensing, unlensed Q and U maps are first generated at two times the resolution of the final output lensed Q and U maps. For each realization of the lensing potential, maps of the real-space x- and y-deflections are generated, and lensed maps are produced from the unlensed Q and U maps by bicubic interpolation of the values at the undeflected positions. This is sufficient for pixelization artefacts in polarization lensing reconstruction to be sub-percent. Random isotropic Gaussian beam-deconvolved detector noise is added

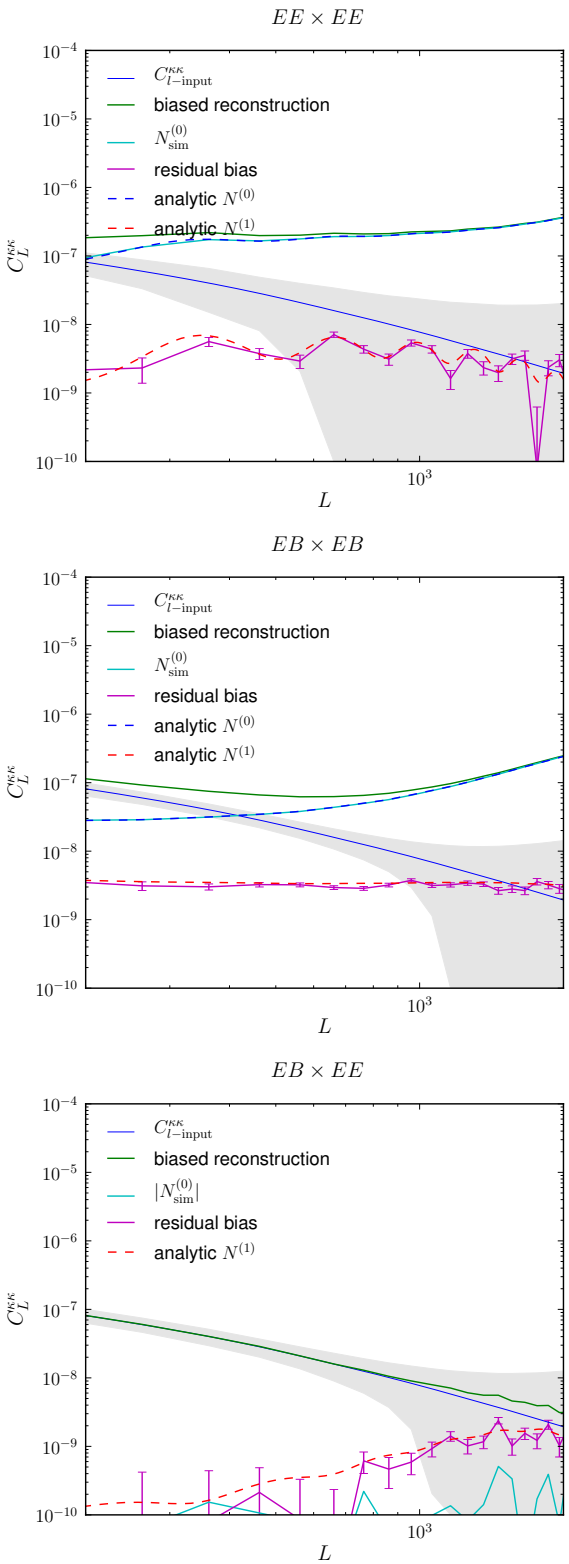

Figure 2.4: The lensing reconstruction power spectra from the $EE \times EE$, $EB \times EB$ and $EB \times EE$ estimators on a $9° \times 9°$ patch of sky with periodic boundaries. Lines show the biased reconstruction, $N^{(0)}_{\mathrm{sim}}$, and residual bias from 1000 simulations, binned with $\Delta L = 100$. The binned one-sigma error on the reconstruction is shown by the grey band for any single realization, while the error bars on the residual bias are Monte Carlo errors from the simulations. Analytic values of the $N^{(0)}$ and $N^{(1)}$ biases are also shown for comparison (dashed lines).

with a power spectrum corresponding to $\triangle_p = 4\mu$Karcmin:

$$N_l^{EE} = N_l^{BB} = N_l = (\triangle_p)^2 e^{l(l+1)\sigma^2_{FWHM}/8\ln 2}. \tag{2.19}$$

The beam-deconvolved lensed noisy maps are then used as the input for the quadratic estimator of the lensing potential, which initially returns a biased reconstruction with expectation $C_L^{dd} + N^{(0)}(L) + \text{residual}$. To calculate the $N^{(0)}$ bias from the simulations $N^{(0)}_{\rm sim}$, we apply the quadratic estimator to unlensed maps generated with lensed power spectra (denoted $\bar{E}(\mathbf{l})$ and $\bar{B}(\mathbf{l})$):

$$\hat{\alpha}^{N0}_{EE}(\mathbf{L}) = \frac{A_{EE}(L)}{L}\int \frac{d^2\mathbf{l}}{2\pi}\bar{E}(\mathbf{l})\bar{E}(\mathbf{l}')\frac{f_{EE}(\mathbf{l},\mathbf{l}')}{2C^{EE}_{{\rm obs},l}C^{EE}_{{\rm obs},l'}}, \tag{2.20}$$

$$\hat{\alpha}^{N0}_{EB}(\mathbf{L}) = \frac{A_{EB}(L)}{L}\int \frac{d^2\mathbf{l}}{2\pi}\bar{E}(\mathbf{l})\bar{B}(\mathbf{l}')\frac{f_{EB}(\mathbf{l},\mathbf{l}')}{C^{EE}_{{\rm obs},l}C^{BB}_{{\rm obs},l'}}. \tag{2.21}$$

To get the $N^{(0)}_{\rm sim}$ bias power spectrum we take the power spectra of Eq. (2.20) and Eq. (2.21) averaged over 1000 simulations, which we can use as a check of the analytic result on the full sky. We do not use the realization-dependent $N^{(0)}$ subtraction here, which may be significantly better for an actual data analysis where the theory and noise power spectra are uncertain, and reconstruction noise correlations would otherwise need to be modelled (Hanson et al., 2011; Schmittfull et al., 2013).

From $\hat{C}^{dd({\rm biased})}_{ijpq,L}$, the raw power spectrum of the deflection angle quadratic estimators on the lensed maps, we define the residual bias $\hat{r}$(L) to be the difference from the input theoretical power spectrum after the Gaussian $N^{(0)}_{\rm sim}$ bias has been subtracted. This is expected to be approximately $N^{(1)}(L)$, and is estimated from the simulations using

$$\hat{r}_{ijpq}(L) = \frac{1}{n_{\rm sim}}\sum_{k=1}^{n_{\rm sim}}\left[\hat{C}^{dd({\rm biased})}_{ijpq,L}\right]_k - N^{(0)}_{ijpq,{\rm sim}}(L) - C_L^{dd}, \tag{2.22}$$

where $n_{\rm sim} = 1000$ and $ij, pq \in EE, EB$. Figure 2.4 shows the average lensing reconstructions for the $EE\times EE$, $EB\times EB$ and $EE\times EB$ power spectrum estimators, along with the $N^{(0)}_{\rm sim}$ and the residual bias as described above. For comparison we show the expected analytic $N^{(0)}$ and $N^{(1)}$ biases as described in section 2.1.1.

The analytic $N^{(0)}$ biases are consistent with the simulated $N^{(0)}_{\rm sim}$ within binning for each estimator. For the $EB\times EE$ reconstruction we show the absolute value of the $N^{(0)}$ from simulation $|N^{(0)}_{\rm sim}|$. Although the theoretical $N^{(0)} = 0$ for the $EB\times EE$ power spectrum reconstruction, in practice we find $N^{(0)}_{\rm sim} \neq 0$ at a level which is small and negligible for the total reconstruction, believed to be induced by pixelization. The $N^{(0)}_{\rm sim}$ biases are shown and discussed in more detail in Fig. 2.12 in a later section.

Furthermore, the analytic $N^{(1)}$ bias is broadly consistent with the residual bias $\hat{r}(L)$ within the 1σ error bars from 1000 simulations. At the level of accuracy required the $N^{(1)}$ bias therefore seems to be an adequate model for the residual bias for polarization reconstruction on small periodic patches of sky. As a test that our pipeline is working correctly, we also calculated the cross correlation power of each lensing realization map with the reconstructed lensing map, which agreed well with the input theoretical lensing power spectrum.

As an aside we note that the formulation of the EB estimator given in Kesden et al. (2003) is slightly suboptimal, as it is derived with a constraint that the estimator is symmetric under interchange of E and B. A comparison of the $N^{(0)}$ bias for the EB quadratic estimator given in Kesden et al. (2003) compared to the form give by Hu & Okamoto (2002) shows that Kesden et al. (2003) is $\sim 25\%$ larger than Hu & Okamoto (2002) on scales $l \gtrsim 2000$. We use the estimators of Hu & Okamoto (2002) (updated with lensed spectra in the weights as described in section 2.1.1), since they are perturbatively optimal on the full sky.

2.3 Polarization reconstruction on the cut sky

In this section we examine the more realistic case of lensing reconstruction when there is a boundary to the observed region. We simulate $EE \times EE$, $EB \times EB$ and $EB \times EE$ lensing power spectrum reconstruction on a cut patch of sky, and then show the improvement in the reconstruction for $EB \times EB$ and $EB \times EE$ when the pure-B mode estimator is used rather than windowing Q and U directly. The underlying quadratic estimators for the cut sky non-periodic boundary cases are:

$$\hat{\alpha}^{\rm cut}_{EE}(\mathbf{L}) = \frac{A_{EE}(L)}{L}\int \frac{d^2\mathbf{l}_1}{2\pi} E^{\rm pseudo}(\mathbf{l}_1) E^{\rm pseudo}(\mathbf{l}_2) \frac{f_{EE}(\mathbf{l}_1,\mathbf{l}_2)}{2C^{EE}_{{\rm obs},l_1} C^{EE}_{{\rm obs},l_2}}, \tag{2.23}$$

$$\hat{\alpha}^{\rm cut}_{EB}(\mathbf{L}) = \frac{A_{EB}(L)}{L}\int \frac{d^2\mathbf{l}_1}{2\pi} E^{\rm pseudo}(\mathbf{l}_1) B^{\rm pseudo}(\mathbf{l}_2) \frac{f_{EB}(\mathbf{l}_2,\mathbf{l}_2)}{C^{EE}_{{\rm obs},l_1} C^{BB}_{{\rm obs},l_2}}, \tag{2.24}$$

$$\hat{\alpha}^{\rm pure}_{EB}(\mathbf{L}) = \frac{A_{EB}(L)}{L}\int \frac{d^2\mathbf{l}_1}{2\pi} E^{\rm pseudo}(\mathbf{l}_1) B^{\rm pure}(\mathbf{l}_2) \frac{f_{EB}(\mathbf{l}_1,\mathbf{l}_2)}{C^{EE}_{{\rm obs},l_1} C^{BB}_{{\rm obs},l_2}}. \tag{2.25}$$

To make our simulated maps non-periodic, we cut out and use one quarter of the $9^\circ \times 9^\circ$ periodic map, which is a $4.5^\circ \times 4.5^\circ$ patch (now with non-periodic boundaries). All other properties of the map simulation are unchanged from those described in section 2.2. To mitigate the effect of harmonic ringing, we use an apodization window which goes

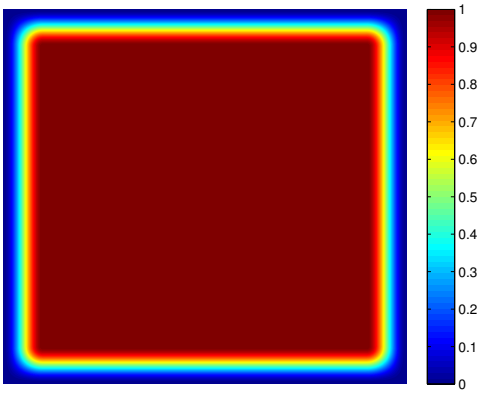

Figure 2.5: The apodization window.

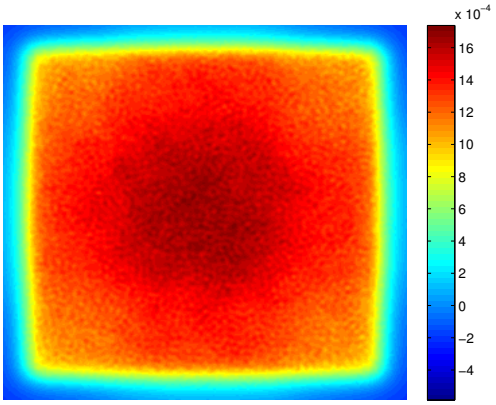

Figure 2.6: The mean field map for $\hat{\alpha}^{\rm cut}_{EE}$.

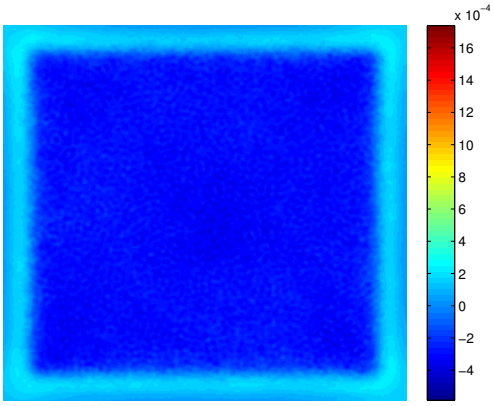

Figure 2.7: The mean field map for $\hat{\alpha}^{\rm cut}_{EB}$.

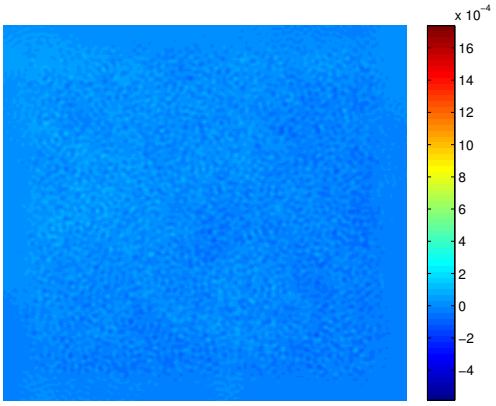

Figure 2.8: The mean field map for $\hat{\alpha}^{\rm pure}_{EB}$.

smoothly to zero at the edges, as required to construct the pure-B mode estimator of Eq. (2.18). We use a window which contains mostly unit values except for a simple cosine tapering on the edge which is one tenth the size of the cut patch. The window is shown in Fig. 2.5. The tapering around the edge is a quarter-period cosine which is normalized such that the tapering falls smoothly from unity in the central area to zero at the map boundary over the one tenth edge. The cut sky patch consists of 600×600 pixels. As the deflection field is generated on the larger $9^\circ \times 9^\circ$ patch before being cut, the cut patch contains modes down to $l_{\rm min} = 20$ (although after cutting the angular scale of the patch is $l = 40$).

The cut sky and window introduce statistical anisotropy in the map, which gives rise to a spurious signal in the lensing reconstruction from $W(\mathbf{x})(Q + iU)(\mathbf{x})$. The average map-level bias is called the mean field (Hanson & Lewis, 2009), and typically closely follows the shape of the window that is causing it. There can also be other sources of

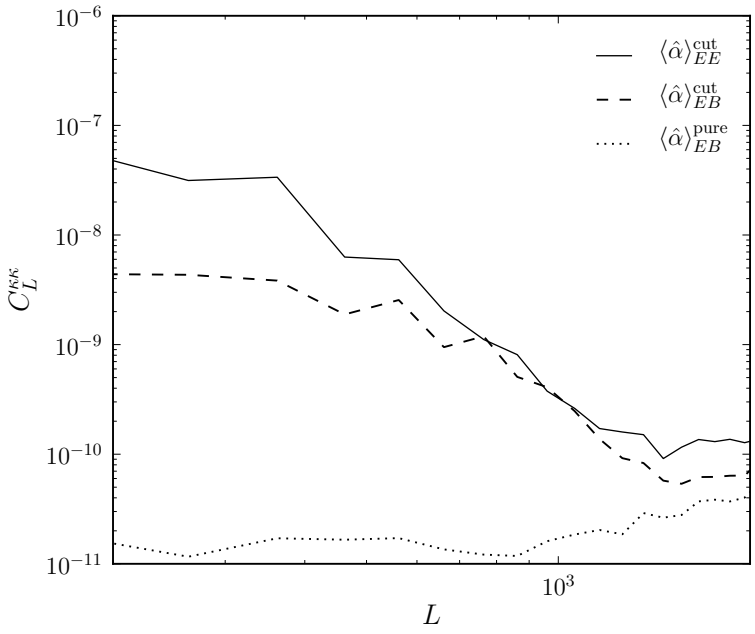

Figure 2.9: Power spectra of the mean field maps shown in Figs. 2.6, 2.7 and 2.8. The EB mean field is substantially reduced by using pure-B modes in the estimator, in good agreement with the low level of EB mean field found by Namikawa & Takahashi (2013) using inverse variance weighting.

mean field, like beam asymmetries and anisotropic noise, but for simplicity we restrict our analysis to isotropic noise. For an ideal full sky measurement the lensing estimators should average to zero, i.e. $\langle\hat{\alpha}\rangle = \langle\alpha\rangle = 0$, but this is no longer the case in the presence of a window. However, simulations can be used to estimate the mean field $\langle\hat{\alpha}\rangle$, which can then be subtracted from the lensing estimator to form an unbiased reconstruction $\hat{\alpha} - \langle\hat{\alpha}\rangle$. To obtain the mean field 1000 reconstructed lensing potential maps were averaged in the map space. This mean field map was then removed from the reconstructed lensing potential maps prior to taking their power spectra.

Figures. 2.6, 2.7 and 2.8 show the mean field maps from the three reconstruction estimators that we simulate on the cut sky: an EE reconstruction, an EB reconstruction using the cut sky B modes, and an EB reconstruction using pure-B modes. The corresponding mean-field power spectra are shown in Fig. 2.9. Unsurprisingly, the mean field follows the shape of the window and is largest in the centre. The EB mean field calculated using the pure-B modes is much less than the EE mean field, in agreement with Namikawa & Takahashi (2013). Without the projection into pure-B modes this is no longer true, and the mean field is substantially larger.

The cut-sky estimators have a reduced amplitude due to the window having $W(\mathbf{x}) < 1$,

and this must be accounted for when estimating power spectra from the windowed sky. In the limit that all the modes of interest (Q, U and lensing potential) are much smaller than the scale of variation of the window, the window can locally be regarded as a constant, and the lensing reconstruction estimator (which depends quadratically on Q and U) is therefore simply the full-sky value multiplied by $[W(x)]^2$. The local power spectrum then scales like $[W(\mathbf{x})]^4$, and the value estimated over the full patch is therefore expected to be scaled by the average value of W^4. Likewise the variance of the power spectrum locally scales like $[W(\mathbf{x})]^8$. Following Benoit-Levy et al. (2013) we therefore use averaged f_{W4} and f_{W8} factors to account for the window in the power spectra and variance respectively, where on the pixelized map

$$f_{Wn} \equiv \frac{1}{N_{\rm pix}} \sum_i \left[W(\mathbf{x}_i)\right]^n . \tag{2.26}$$

This is expected to be accurate for the intermeidate-scale reconstruction from EE (where all the information is in small-scale E modes), but may be less accurate for the EB reconstruction where the B-mode contribution is much less local.

All our simulated cut-sky power spectra ($N^{(0)}_{\rm sim}$, residual bias, biased reconstruction and unbiased reconstruction) have been scaled to account for the smaller sky fraction and the effect of the window via a scaling factor f_{W4}. For example our power spectrum estimators for the cut sky are

$$\hat{C}^{dd({\rm biased})}_{ijpq,L} \equiv \frac{1}{f_{W4}} \left[\hat{C}^{dd({\rm cut})}_{ijpq,L}\right]. \tag{2.27}$$

For a periodic sky patch, neglecting first order ($N^{(1)}$) biases, the approximate error in the lensing potential for the $EE \times EE$ and $EB \times EB$ power spectrum estimators is (Hu & Okamoto, 2002):

$$\triangle C^{dd}_L \approx \frac{1}{\sqrt{L \triangle L f_{\rm sky}}} \left[C^{dd}_L + N^{(0)}(L)\right], \tag{2.28}$$

and for the $EB \times EE$ power spectrum estimator:

$$\triangle C^{dd}_L \approx \frac{1}{\sqrt{2L \triangle L f_{\rm sky}}} \sqrt{\left[C^{dd}_L + N^{(0)}(L)\right]_{EE} \left[C^{dd}_L + N^{(0)}(L)\right]_{EB} + \left(C^{dd}_L\right)^2}, \tag{2.29}$$

where ΔL is the bin size. For a windowed sky patch, the error in a measurement of the lensing potential is modified to approximately (Benoit-Levy et al., 2013):

$$\triangle C^{dd-{\rm cut}}_L \approx \sqrt{\frac{f_{W8}}{f^2_{W4}}} \triangle C^{dd}_L, \tag{2.30}$$

if there are no issues of E/B mixing. On small scales with lower noise, the error bars would be significantly increased due to $N^{(1)}$ biases which couple in cosmic variance from larger-scale modes.

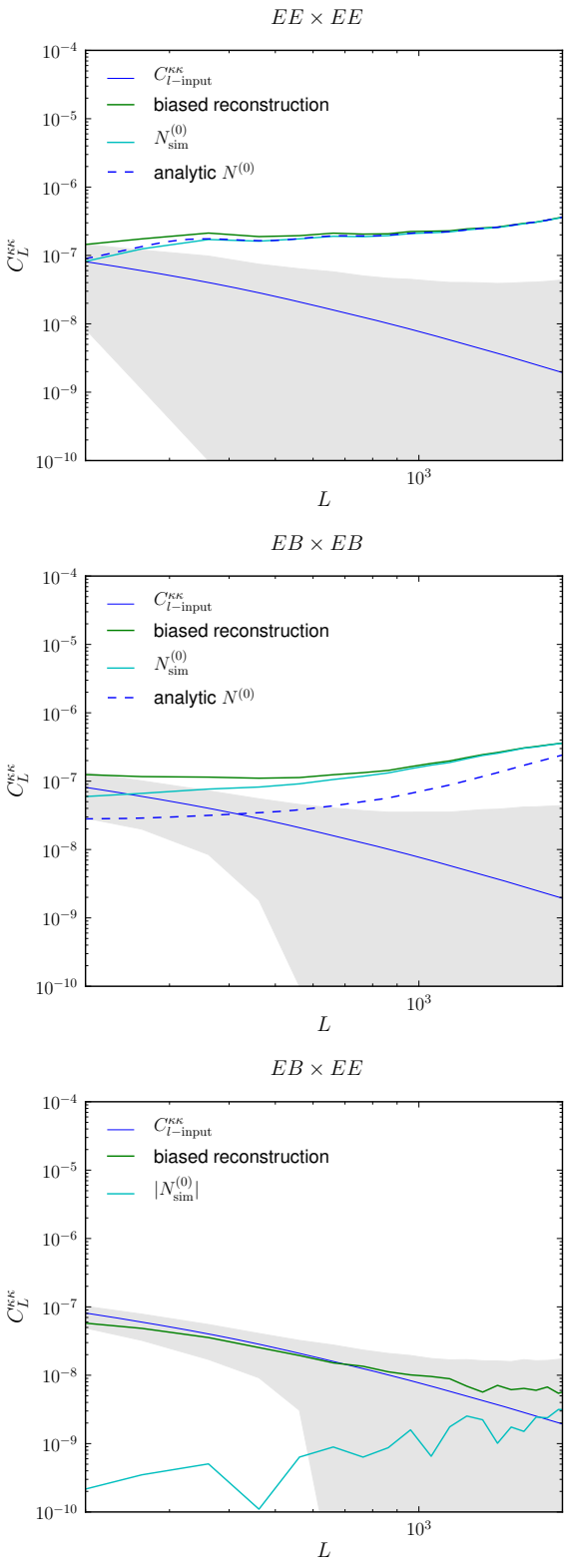

Figure 2.10: The lensing reconstruction using the $EE \times EE$, $EB \times EB$ and $EB \times EE$ power spectrum estimators on a $4.5^\circ \times 4.5^\circ$ apodized cut patch of sky (without E/B separation). The binned one sigma error on the reconstruction is shown by the grey band for any single realization. The full-sky analytic $N^{(0)}$ bias is also shown for comparison. Results shown are from 1000 simulations.

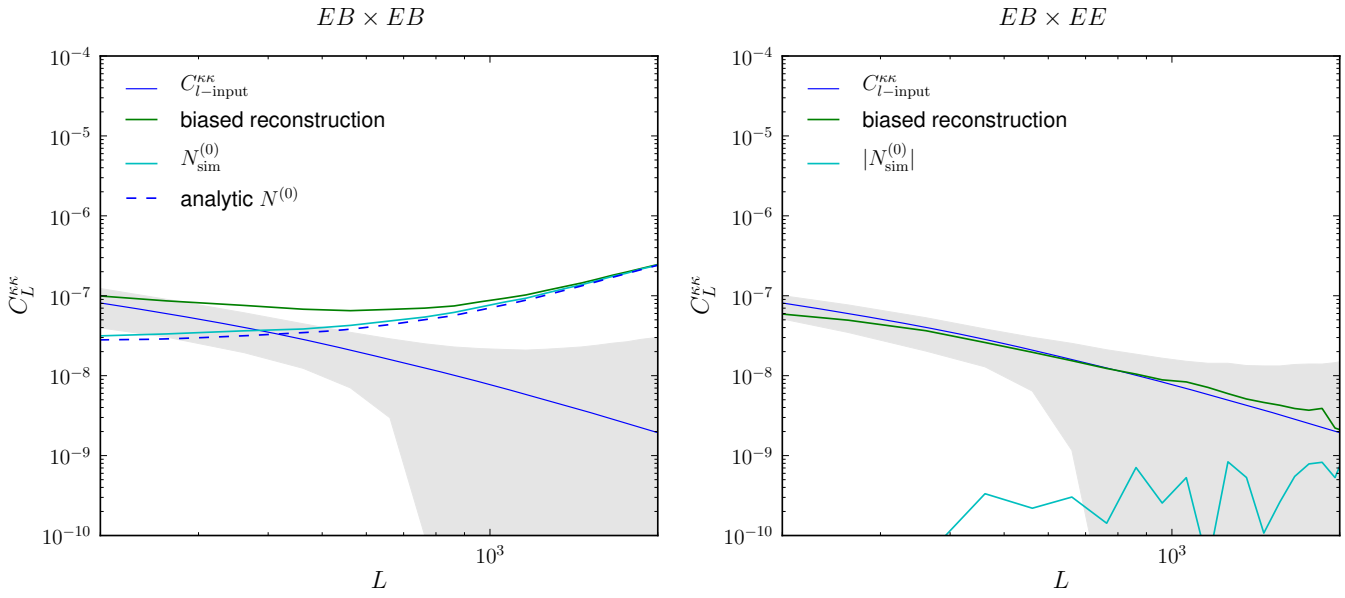

Figure 2.11: The lensing reconstruction using the $EB \times EB$ and $EB \times EE$ quadratic estimators as in Fig. 2.10, but now using pure-B modes in the estimators.

For our choice of window function the scaling factors are $f_{W4} = 0.1826, f_{W8} = 0.1761$, which are less than the 0.25 value one would get from a quarter patch without apodization. We also use a top-hat binning with size $\Delta L = 100$. Using a bin size of e.g. $\Delta L = 50$, close to the window scale, led to correlations between the bins, causing the variance to be underestimated when not accounting for covariances. Tests showed that $\Delta L = 100$ is large enough to prevent large correlations between bins, although for the f_{sky}-scaled comparison of the error bars shown later in Fig. 2.13 we use $\Delta L = 200$ to reduce correlations to a very low level. The cut-sky reconstructed power spectra for $EE \times EE$, $EB \times EB$ and $EB \times EE$ are shown in Fig. 2.10.

In all the cut-sky reconstructions, the error bars are larger than the reconstructions without boundaries, as expected due to the significantly reduced effective area. The leakage of E into B modes is also expected to increase the non-lensing B mode power, and hence increase error in the reconstructions involving cut-sky B modes. Removing this leakage should reduce the error bars. In Fig. 2.11 we show that the the errors are indeed significantly reduced by using pure-B modes in the $EB \times EB$ and $EB \times EE$ estimators.

Figure 2.12 shows a comparison of the $N_{\mathrm{sim}}^{(0)}$ bias power for the $EE \times EE$, $EB \times EB$ and $EB \times EE$ reconstructions in the periodic boundary and cut sky cases. The analytic $EB \times EE$ has $N_{EBEE}^{(0)} = 0$ in the ideal full-sky case, but this becomes non-zero when there is leakage from E into B. Using the pure-B modes successfully reduces $N_{EEEB}^{(0)}$ back to a low level. For the $EB \times EB$ reconstruction using the pure-B modes results in an $N_{\mathrm{sim}}^{(0)}$

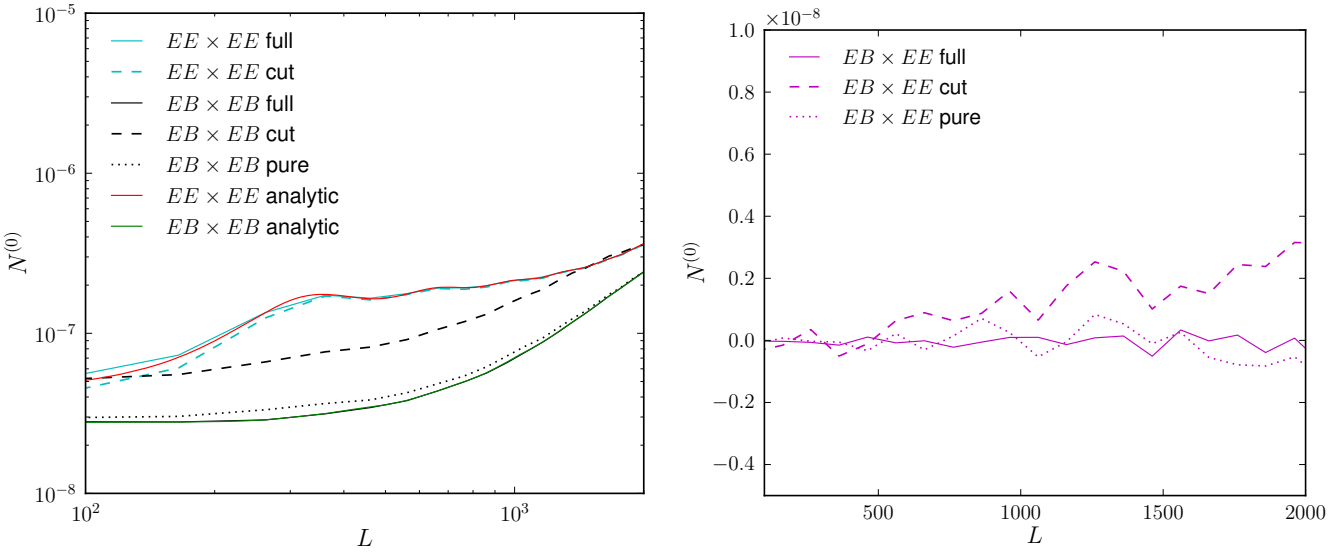

Figure 2.12: A comparison of the $N^{(0)}$ bias reconstructions on the periodic and non-periodic sky patches. Note that non-periodic cut sky power spectra have been scaled by an f_{W4} factor. Left: The $EE \times EE$ and $EB \times EB$ reconstructions. Right: The $EB \times EE$ reconstructions.

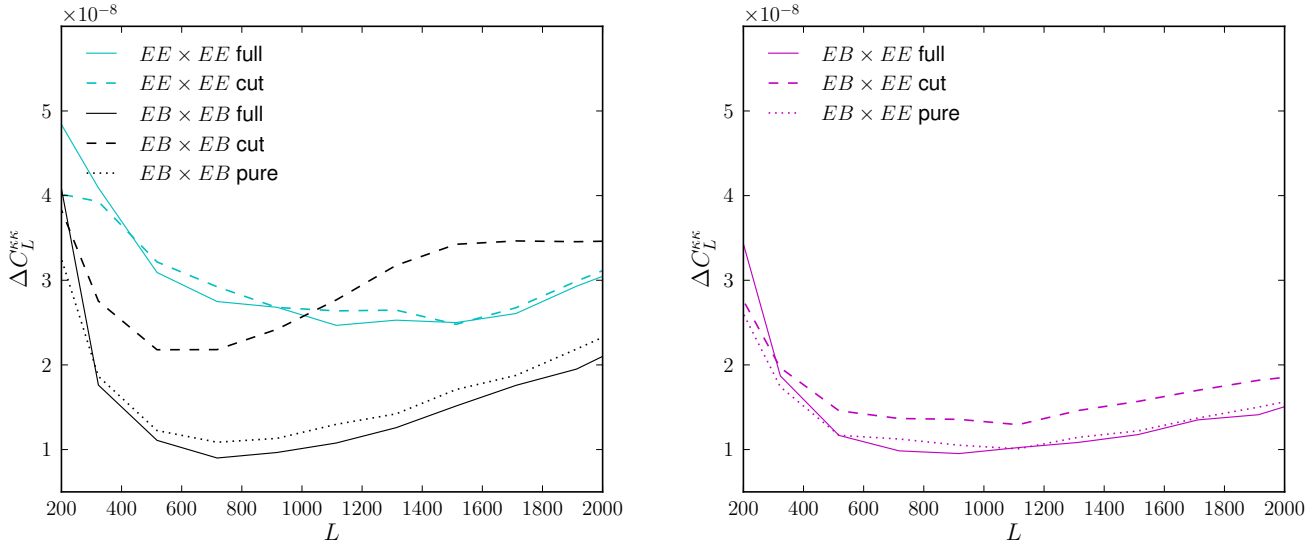

Figure 2.13: A comparison of the lensing power spectrum reconstruction errors, which are significantly reduced by using pure-B rather than cut-sky B modes in the estimators involving B modes. Note that error bars on the periodic sky have been scaled to have the same sky fraction as a periodic $4.5^\circ \times 4.5^\circ$ patch, and the binning here is $\Delta l = 200$ to reduce correlation between bins. Left: The $EE \times EE$ and $EB \times EB$ reconstruction error bars. Right: The $EB \times EE$ reconstruction error bars.

bias roughly the same amplitude as in the ideal full-sky case (i.e. with periodic boundary conditions). The cut-sky analysis without using pure-B modes however produces a much larger $N^{(0)}$ bias, because the leakage of E into B increases the reconstruction variance (which is sensitive to the larger pseudo-B-mode power spectrum). For the $EE \times EE$ reconstruction the $N^{(0)}_{\rm sim}$ bias on the cut sky appears to be slightly lower on large scales than for the periodic sky patch. This is probably due to the approximate f_{W4} scaling that we have used being inadequate on scales approaching the scale of variation of the window (see further discussion below). The $N^{(0)}_{\rm sim}$ bias on the periodic-sky $EE \times EE$ reconstruction appears slightly high on large scales, but this is just due to the binning.

In Fig. 2.13 we show a comparison of the 1σ error bars of the various reconstructions considered in this work. The smallest error bars come from the periodic sky reconstructions which use B modes: the $EB \times EB$ and $EB \times EE$ reconstructions. The $EB \times EE$ estimator does slightly better on small scales, since there is no $N^{(0)}$ noise term dominating at small scales in this case. The error in the cut-sky $EB \times EB$ case is much worse, as expected due to E/B mixing. However, using the pure-B mode reconstruction improves the cut-sky error bars dramatically. Note that the periodic sky error bars have been scaled by a factor of two to have the same error as expected from a $4.5^\circ \times 4.5^\circ$ periodic patch. For the comparison shown, the pure-B mode error bars are roughly the same as the periodic sky error bars, showing that the pure-B method works very well to mitigate the loss from E/B mixing. In Fig. 2.13 the binning used is $\Delta L = 200$, chosen to mitigate correlation between bins which was causing the the $f_{\rm sky}$-scaled error bars to look better than optimal for the cut-sky. Eq.(2.30) shows that, without any spurious reduction from bin correlations, an increase in error bar size of $\sim$15% is expected for the windowed sky patch compared to the un-windowed periodic patch.

Finally, we investigate whether there are any additional biases that appear when using apodized cut sky maps and a simple constant f_{W4} scaling factor. As shown in the left panel of Fig. 2.14, we observe a substantial low bias on very large scales. Since the estimators by construction average to zero for Gaussian fields, any bias must scale at least with the lensing power C_l^{dd}, and we find a nearly-linear scaling consistent with Ade et al. (2013b). The large-scale bias also affects the error bars of Fig. 2.13, where on the largest scales the cut-sky error bars appear to be lower than in the optimal case without boundaries. This is because we have not recalibrated the errors for the bias.

To assess the size of the small-scale residual bias we show the ratio to the input lensing power spectrum in the right-hand panel of Fig. 2.14. On intermediate scales the analytic

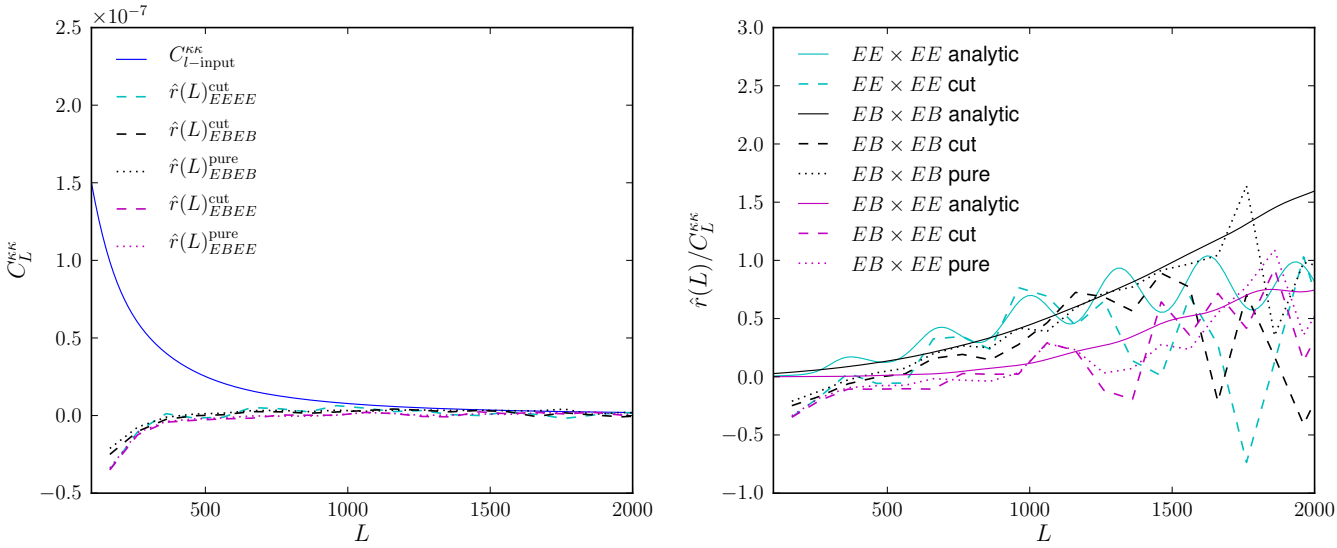

Figure 2.14: Left: The residual biases of the cut sky and pure-B mode sky reconstructions shown in Figs. 2.10 and 2.11 compared to the input lensing power spectrum. Right: The ratio of the residual biases shown in the left-hand panel to the input lensing power spectrum. There is a significant negative bias on large scales, but the small-scale bias is fit quite well by the analytic $N^{(1)}$ (Monte Carlo simulation error dominates on very small scales).

$N^{(1)}$ is a reasonable fit to the bias. For our chosen noise level it is difficult to see the residual bias within the reconstruction noise on very small scales, so we also looked at a simulation with zero noise. We found that the cut-sky residual bias was similar to the full-sky bias, and mostly still close to the analytic $N^{(1)}$, with corrections being small compared to the size of the signal. This suggests that the residual bias on small scales is still fit reasonably well by the approximate analytic $N^{(1)}$, although there may be some approximation error and also a mixing and/or scaling of reconstruction modes that is not accurately accounted for by the simple constant f_{W4} diagonal scaling. For current-generation data the biases are small compared to the reconstruction noise, and the analytic $N^{(1)}$ model is adequate except on large scales.

The large- and small-scale features of the residual bias are likely window dependent, and may be somewhat mitigated with a more optimal choice of window. They are also easily accounted for by subtracting the residual bias measured in simulations, as long as the model assumed for the simulations accurately matches reality. Alternatively they could be approximately modelled as an L-dependent normalization (transfer function). However accurate parameter estimation with more sensitive lensing reconstructions should consider

a more detailed analysis of the full scale dependence of the window function relating the estimated and true lensing power spectra, including L-mixing due to the well-known $N^{(1)}$ bias as well as cut-sky affects. More optimal estimators using full inverse variance weighting may turn out to have simpler properties than the simple windowed estimators considered here, however the $N^{(1)}$ bias is non-local in L and would still have to be modelled.

2.4 Summary

In this chapter we simulated polarization lensing reconstruction for small areas of sky. We used these reconstruction simulations to investigate biases and signal-to-noise in both periodic and non-periodic windowed maps, and tested the use of pure-B modes in the standard quadratic estimator to mitigate the effects of E/B leakage on the cut sky. The main findings are:

For a periodic patch:

- Analytic results for the $N^{(0)}$ and $N^{(1)}$ bias are adequate to model the leading reconstruction biases for current data. There is some evidence for small systematic deviations from the analytic results, possibly arising from higher-order effects or assumed approximations, which may require more detailed study in future.

For the cut sky:

- The large $\hat{\alpha}_{EB}$ mean field introduced by E/B mixing is greatly reduced by using pure-B modes in the estimator ($\hat{\alpha}^{\rm pure}_{EB}$), consistent with the low EB mean field found by Namikawa & Takahashi (2013).

- Using pure-B modes significantly reduces the variance in the power spectrum reconstruction, and for the simple constant noise and nearly-constant window considered here, the reconstruction error is close to optimal.

- We confirm the finding of Ade et al. (2013b) that there is a substantial residual bias on large scales if a simple constant normalization is assumed.

- The approach we present for reconstructing the lensing power spectrum on the cut sky should be sufficient for current-generation CMB polarization measurements if the residual bias is accounted for by simulation, and makes a simple alternative to more numerically-costly perturbatively-optimal estimators.

- Detailed characterization of the normalization biases on the cut-sky may be required to fully exploit future more sensitive observations, where there may also be larger gains from the use of more optimal estimators (including going beyond perturbative leading order).

Chapter 3

Cross Correlation with Large-Scale Structure

3.1 Introduction

The contents of this chapter are based on work presented in Pearson & Zahn (2014) and represent work done by the author in collaboration with Oliver Zahn. In the past few years CMB lensing science has arisen as a promising new probe of cosmology. CMB photons are deflected by matter fluctuations between the surface of last scattering and today. The effect is sensitive to the geometry of the Universe (e.g., dark energy and its evolution) and the shape of the matter power spectrum (affected by e.g., massive neutrinos). Since CMB lensing probes all matter, it should be correlated with galaxy surveys observing the large-scale structure of the Universe. The cross correlation between CMB lensing and such large-scale structure surveys should aid in simultaneously measuring galactic and non-galactic cosmological information. There is already a wealth of data available for such analysis, and upcoming surveys will offer even better opportunities for cross correlation science. A few examples of work to date include: CMB lensing cross correlated with radio galaxies, LRGs and IR using *Planck*, NVSS Quasars, SDSS LRGs, WISE and MAX BCG clusters (Ade et al., 2013f), CMB lensing cross correlated with radio galaxies using WMAP and NVSS (Smith et al., 2007; Feng et al., 2012), CMB lensing cross correlated with LRGs, quasars and radio galaxies using WMAP, NVSS and SDSS (Hirata et al., 2008), CMB lensing cross correlated with optical and IR using SPT, BCS, WISE and Spitzer (Bleem et al., 2012), CMB lensing cross correlated with quasars using ACT, and SDSS (Sherwin et al., 2012), CMB lensing cross correlated with sub-millimetre wavelength galaxies using SPT and Herschel/SPIRE (Holder et al., 2013).

Both CMB temperature and polarization are being measured by modern experiments. At the detector level, the polarization measurement is in terms of the Stokes parameters Q and U, but it is usually useful to consider CMB polarization in terms of even and odd parity modes, the E and B mode respectively. The temperature anisotropy has been measured well down to arcminute scales (e.g. Jones et al. (2006); Hinshaw et al. (2013); Ade et al. (2013e); Calabrese et al. (2013); Story et al. (2013)), E mode polarization has been detected by several groups (e.g. Leitch et al. (2005); Montroy et al. (2006)), and a first measurement of the conversion of E mode to B mode polarization by lensing has been made (Hanson et al., 2013). An observation of large-scale B modes extra to lensing and foreground components could be direct evidence of a primordial gravitational background, and used to discern inflationary theories. Even without the B mode though, observations of E mode polarization allow improved constraints on cosmological parameters compared to temperature information alone, since they are sensitive to the epoch of reionization as well as recombination physics. To obtain the CMB lensing signal, the quadratic estimator method of Hu & Okamoto (2002) is usually used (see section 1.2.3 for discussion). The CMB lensing potential can be reconstructed from various combinations of T, E and B mode measurements. So far the lensing power spectrum has been measured using the temperature anisotropy observed by the Atacama Cosmology Telescope (ACT) (Das et al., 2011), (Das et al., 2013), the South Pole Telescope (SPT) (van Engelen et al., 2012), and most recently the Planck satellite (Ade et al., 2013f) and POLARBEAR experiment (Ade et al., 2013b). Lensing also affects the peaks and troughs in the angular power spectra (e.g., Keisler et al. (2011); Story et al. (2013)). Finally, CMB lensing mixes primordial E modes into lensing-specific B modes. This allows reconstruction of the CMB lensing potential with much smaller variance than for the temperature modes, because no primordial B modes are expected on small scales.

A Fisher matrix calculation marginalizing over various cosmological parameters can be used to estimate the constraining power of current and future data sets. In this work, different CMB and galaxy survey sensitivities are explored with the goal of showing how well cosmology can be constrained in the presence of uncertainties in the galaxy physics, and vice-versa. In particular, we are interested in how well the parameters are constrained using the CMB lensing - galaxy cross correlation. Seven non-galactic parameters are included in the analysis with the following fiducial values: physical baryon fraction ($\Omega_{\rm b}h^2$=0.02258), physical cold dark matter fraction ($\Omega_{\rm CDM}h^2$=0.1109), dark energy fraction (Ω_λ=0.734), physical neutrino mass fraction ($\Omega_\nu h^2$=0.002), optical depth (τ=0.088),

spectral index ($n_{\rm s}$=0.963), scalar amplitude ($A_{\rm s} = 2.43 \times 10^{-9}$); and up to three galactic parameters: the linear galaxy bias (b), the mean of the galaxy redshift distribution (μ), and the standard deviation of the galaxy redshift distribution (σ).

Previous work has already shown that cross-correlation of structure and CMB lensing can constrain various biases, and thus provide useful information for cosmology (Vallinotto, 2012, 2013; Rhodes et al., 2013). In particular, CMB lensing can break degeneracy between the matter power spectrum normalisation and systematic multiplicative biases in shear measurements (Vallinotto, 2012), and can constrain the linear galaxy bias (Vallinotto, 2013). Our work complements the latter analysis by allowing redshift distribution parameters to also vary.

Section 3.2 introduces the Fisher methodology used and outlines the derivation of our theoretical power spectra. In section 3.3 we describe some current and future CMB and galaxy surveys as well as our data cuts. Results on cosmological parameters are given in section 3.4 and we conclude in section 3.5.

3.2 Method

The Fisher matrix formalism provides an estimate for how well an experiment can distinguish the true model of the universe from other models. For a model described by N parameter values (which can be cosmological or astrophysical in nature) $p_i (i = 1, ..., N)$, and a (multivariate Gaussian) likelihood of an observation given these parameters as $\mathcal{L}(O, p_i)$, the Fisher information matrix is given by (Spanos, 1986; Tegmark, 1997):

$$\mathbf{F}_{ij} \equiv - \left\langle \frac{\partial^2 \ln \mathcal{L}(O, p_i)}{\partial p_i \partial p_j} \right\rangle , \tag{3.1}$$

where the partial derivatives and the averaging are evaluated around a fiducial (best guess for the true) set of parameters values. The Cramer-Rao inequality states that $(F^{-1})_{ii}$ is the smallest variance that any unbiased estimator of the parameter p_i can have, and we can generally think of F^{-1} as the lower bound of the covariance for estimates of the vector p_i. If there is some prior constraint on the error of a parameter $\sigma_{\rm prior}$, this information is added in the Fisher matrix via $F_{ii} = F_{ii} + \frac{1}{\sigma^2_{\rm prior}}$.

Dropping irrelevant constant terms, the $\ln \mathcal{L}(O, p_i)$ of Eq. (3.1) can be written down as the natural logarithm of the determinant of the covariance matrix plus a term including the fiducial parameter vector p_i. The first derivative is zero due to construction, and the the second derivative gives the 1σ displacement from the mean (Verde, 2007). For the case considered here, the first term dominates and summing many modes of the CMB power

spectra (via the trace) ensures Gaussianity via the central limit theorem. The Fisher matrix then becomes (Tegmark, 1997; Perotto et al., 2006):

$$F_{ij} = \sum_{\mathrm{l=2}}^{l_{\mathrm{max}}} \sum_{\mathrm{PP',QQ'}} \frac{\partial C_l^{\mathrm{PP'}}}{\partial \lambda_i} (\mathbb{C}_l^{-1})_{\mathrm{PP'QQ'}} \frac{\partial C_l^{\mathrm{QQ'}}}{\partial \lambda_j}, \tag{3.2}$$

where C_l are power spectra. In this analysis we form two Fisher matrices. The first includes auto and cross correlations from CMB temperature and polarization: $PP', QQ' \in TT, EE, TE$. The second includes auto and cross correlations of the CMB lensing potential and 2-dimensional galaxy power spectrum: $PP', QQ' \in \phi\phi, GG, \phi G$. $\mathbb{C}_l$ is the 3×3 covariance matrix between the different power spectra, and the elements are made up of the appropriate $(\delta C_l)^2_{PP'QQ'}$:

$$(\delta C_l)_{PP'QQ'} = \sqrt{\frac{1}{(2l+1)f_{\mathrm{sky}}} \left(C_l^{PQ} C_l^{P'Q'} + C_l^{PQ'} C_l^{P'Q}\right)} \tag{3.3}$$

where an associated experimental noise is added to each power spectrum, e.g. for $PQ = TT$, $C_l^{PQ} = C_l^{TT} + C_l^{\mathrm{noise}}$. The factor f_{sky} accounts for the fraction of sky covered by the experiment. In the CMB temperature and polarization case, the C_l^{noise} is taken to be the standard Gaussian random detector noise as in Knox (1995). For the CMB lensing, C_l^{noise} is the $N^{(0)}$ bias as in Hu & Okamoto (2002), and described in Chapter 2. For the galaxy power spectrum it is simple shot noise. The two Fisher matrices are added together for the final constraint, neglecting correlations between $\phi\phi, GG, \phi G$ and the CMB spectra by using unlensed spectra for the latter. We also neglect small correlations between CMB temperature and lensing ($T\phi$) caused by the integrated Sachs-Wolfe (ISW) effect (e.g. Ade et al. (2013d)).

The theoretical auto and cross CMB lensing and galaxy power spectra limber approximated with a simple linear bias model as in Ade et al. (2013g) are:

$$C_L^{\phi\phi} = \int d\chi (K_L^{\phi}(\chi))^2 P(k = L/\chi, \chi), \tag{3.4}$$

$$C_L^{\mathrm{gg}} = \int d\chi (K_L^{\mathrm{g}}(\chi))^2 P(k = L/\chi, \chi), \tag{3.5}$$

$$C_L^{\phi g} = \int d\chi K_L^{\phi}(\chi) K_L^{\mathrm{g}}(\chi) P(k = L/\chi, \chi). \tag{3.6}$$

Here χ is conformal distance and $P(k, \chi)$ is the 3D matter power spectrum at wavenumber k and conformal look back time χ. (Note that Eq. (3.4) is the Limber approximated form of Eq. (1.37), which does not employ the Limber approximation.) The kernels $K_L^{\phi}(\chi)$ and $K_L^{\mathrm{g}}(\chi)$ fold in information about the lensing and the galaxy dynamics respectively:

$$K_L^{\phi}(\chi) = -\frac{3\Omega_m H_0^2}{L^2} \frac{\chi}{a} \left(\frac{\chi_* - \chi}{\chi_* \chi}\right), \tag{3.7}$$

Table 3.1: CMB EXPERIMENTAL SCENARIOS

	Current	3rd gen.	4th gen.
temperature noise (μK-arcmin)	30	2.5	2.5
polarization noise (μK-arcmin)	60	3.5	3.5
beam (arcmin)	7	1	1
$f_{\rm sky}$	0.75	0.1	0.5

Table 3.2: GALAXY EXPERIMENTAL SCENARIOS

	$f_{\rm sky}$	number density (gal/deg^2)
WISE	0.75	10,000
LSST	0.5	198,000
EUCLID	0.4	108,000

$$K_L^{\rm g}(\chi) = \frac{dN}{dz}\frac{dz}{d\chi}\frac{b(z)}{\chi}. \tag{3.8}$$

Eq. (3.7) depends on non-galactic cosmological parameters, whereas Eq. (3.8) depends on both galactic and non-galactic cosmological parameters, since it includes the bias and redshift distribution.

3.3 Data

The derivatives used in the Fisher matrix are calculated using the theoretical power spectra. CMB temperature, CMB polarization, CMB lensing and galaxy power spectra were calculated for the given parameter choice using CAMB sources (Challinor & Lewis, 2011). To obtain the galaxy auto correlation (GG) and galaxy-CMB lensing cross correlation (ϕG), we used a slightly modified version of the code with source and lensing type windows.

Table 3.1 shows the CMB experimental scenarios we consider in this work. The current type experiment is based on the *Planck* satellite, for which the blue book values (Tauber et al., 2006) agree reasonably well with the satellite's performance so far (Ade et al., 2013c). The 3rd generation experiment is a survey with higher angular resolution (1 arcmin FWHM) covering 10% of the sky. We verified that a three times larger beam would not qualitatively change any of the results. The 4th generation experiment has the same angular resolution as the 3rd generation experiment but covers 50% of the sky. The noise in the CMB temperature and polarization is shown in the table, and the CMB

lensing noise is derived from these values. The 3rd generation is representative of surveys already taking data or soon to begin observations, such as SPTpol (Austermann et al., 2012), ACTpol (Niemack et al., 2010) and POLARBEAR (Kermish et al., 2012). The 4th generation is representative of larger sky area surveys planned for the near future, such as the POLARBEAR extension, the Simons-array.

Table 3.2 shows experimental scenarios for 3 galaxy surveys. The Wide-field Infrared Survey Explorer (WISE) is a satellite experiment which observed the whole sky in the mid-infrared. The four observing bands are centred at 3.4, 4.6, 12 and 22 μm (Wright et al., 2010). WISE has already been used in cross correlation with various data sets such as WMAP (Goto et al., 2012), *Planck* (Ade et al., 2013f) and SPT (Geach et al., 2013). The Large Synoptic Survey Telescope (LSST) is a planned 8.4 meter optical ground based telescope which will observe from Cerro Pachón, Chile. The predicted redshift distribution from the LSST science book (Abell et al., 2009) is

$$\frac{dN}{dz} = \frac{1}{2z_0}\left(\frac{z}{z_0}\right)^2 \exp(-z/z_0). \tag{3.9}$$

Here $z_0 = 0.0417i - 0.744$ (where the survey has sensitivity in the i band for magnitudes $21.5 < i < 23$). In section 3.4 we will use LSST as an example next generation survey for constraints on parameters. Choosing $i = 22.25$ for a mid-range magnitude sample gives a fiducial $z_0 = 0.183$, which we use in our calculation. The LSST science book assumes a galaxy bias evolution of $b = 1 + 0.84z$. Given a median redshift of around $z = 1$, we will estimate the fiducial galaxy bias as $b = 1.84$ in our simulations. Euclid is an ESA satellite mission due to launch in 2019. It will observe 15,000 sq deg in optical and near-infrared using a 1.2m space telescope (Laureijs et al., 2011).

Figure 3.1 shows the redshift distributions of various cuts of these galaxy surveys along with the CMB lensing kernel. Also shown is a Gaussian toy model with $\mu = 1$ and $\sigma = 0.5$. This Gaussian is fairly representative of the galaxy distribution redshift ranges, and all redshift distributions show an overlap with the CMB lensing kernel, suggesting that they are useful for cross correlation studies.

In Table 3.3 we show the combinations of CMB and galaxy surveys which we consider in our Fisher calculations, labelled from A-J. To measure a cross correlation, the fractions of sky observed by CMB and galaxy surveys must overlap. If the CMB experiment has a smaller $f_{\rm sky}$ than the galaxy survey, the smaller value must also be used for the galaxy information in that case. We take a conservative approach, considering the same $f_{\rm sky}$ in the GG case as the ϕG case, rather than using the full survey area available for GG. These details can be read from column 3 of the table. For the CMB information in

Table 3.3: FISHER CALCULATION SCENARIOS

Scenario	CMB surveys	$GG, \phi\phi, G\phi$ surveys	Parameters varied (% prior)
A	*Planck*+4G	Gaussian, 4G	ΛCDMν+bias+μ+σ
B	*Planck*+4G	LSST, 4G	ΛCDMν+bias+z_0
C	*Planck*+3G	Gaussian 1k gal/deg^2, 3G	ΛCDMν+bias+μ
D	*Planck*+4G	Gaussian 1k gal/deg^2, 4G	ΛCDMν+bias+μ
E	*Planck*+3G	LSST, 3G	ΛCDMν+bias(20%)
F	*Planck*+4G	LSST, 4G	ΛCDMν+bias(20%)
G	*Planck*+4G	Gaussian, 4G	ΛCDMν+bias(20%)+μ(20%)
H	*Planck*	LSST, *Planck*	ΛCDMν+bias(20%)
I	*Planck*	LSST, *Planck*	ΛCDM+bias(20%)
J	*Planck*+4G	LSST, 4G	ΛCDM+bias(20%)

A description of the combinations of CMB and galaxy experimental scenarios we consider in our Fisher calculations. Column 2 lists surveys which are used in the TT, EE, TE correlations. 3G denotes a third generation experiment with 10% sky coverage, 4G a fourth generation experiment with 50%. Column 3 details the surveys used for the $GG, \phi\phi, G\phi$ correlations, with the sky fraction given by that of the deeper experiment in column 2. LSST is estimated to have a number density of 198,000 gal/deg^2. For the Gaussian cases, we either explore different values of the number density, or set it to 1,000 gal/deg^2. In column 2, surveys are separated by addition signs. This denotes that the Fisher information matrix was constructed for each of these surveys and then added together. In column 3 the surveys are separated by commas. This denotes that information from both surveys was used in one Fisher matrix to construct auto and cross correlations between the CMB lensing and galaxy power spectra. Column 4 shows what parameters have been varied, where ΛCDM(ν) was defined as $\Omega_{\rm b}h^2 + \Omega_{\rm CDM}h^2 + \Omega_\lambda + \tau + n_{\rm s} + A_{\rm s}(+\Sigma m_\nu)$. Notice that priors of 20% have been added to the galaxy parameters in scenarios E, F, G, H, I, and J. These are added to break degeneracies between the galactic and non-galactic parameters in order to make the Fisher matrix invertible.

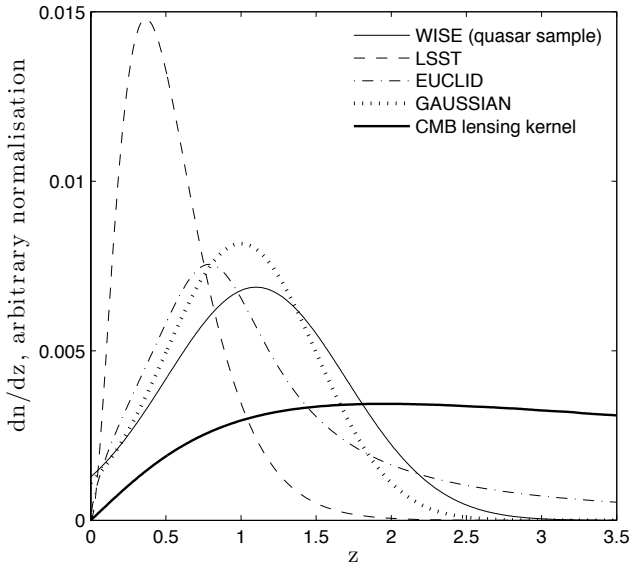

Figure 3.1: Redshift distributions for current and upcoming galaxy survey cuts compared to the CMB lensing redshift kernel. Redshift distributions shown for WISE (quasar sample), LSST and EUCLID are taken from Geach et al. (2013), Abell et al. (2009) and Boldrin et al. (2012) respectively. The Gaussian model has $\mu = 1$, $\sigma = 0.5$.

the TT, EE, TE correlations, we use the maximum $f_{\rm sky}$ possible for the deepest CMB survey (3rd or 4th generation). We then include information from the current (*Planck*) CMB survey, but only up to a combined $f_{\rm sky} = 0.75$, since we do not want to double count patches of sky. This counting assumes that the remaining 25% of the sky are contaminated by foregrounds. In scenarios E, F, G, H, I and J, we add 20% priors to the galaxy parameters. This is to break degeneracies between the galactic and non-galactic parameters in order to make the Fisher matrix invertible. Adding e.g. 40% priors rather than 20% priors made negligible difference to the forecasts.

The GG and ϕG correlations have a sharper cut-off in multipole l, because non-linear clustering will make recovery of cosmological information from smaller scales challenging. The approximate onset of non-linearities at $k \sim 0.2\ h/\mathrm{Mpc}$ yields a projected $l_{\rm non-linear} \gtrsim 300$, assuming a galaxy population peaking at $z \simeq 1$. The ϕG correlation should be less sensitive than GG to the effect of non-linearities because it narrows in on higher redshifts. Taking this into consideration, we choose a slightly higher multipole cut-off of $l_{\rm max} = 500$ for GG and ϕG. In one simulation, we allow the GG and ϕG cut-off to be as high as $l_{\rm max} = 1,000$ and $l_{\rm max} = 5,000$. This is to explore parameter constraints for future improvements in our understanding of the nonlinear clustering regime. In the

same simulation, we calculated the constraint using $l_{\rm max} = 300$, the actual cut-off scale calculated for non-linearities. We found that the constraint in this case was at most <20% worse than that for the default cut-off of $l_{\rm max} = 500$.

Note that we have not modelled scale dependence in the bias due to non-linearities. Some simulations show that non-linear bias should only affect scales where $k \geq 0.7\ h$/Mpc (Zarija, 2008), which is outside the range of modes that we use as our default $l_{\rm max}$. However, other simulation (Smith et al., 2007) and survey (Sanchez et al., 2013) driven work finds that the bias is non-linear on much larger scales. When we move beyond $l_{\rm max} = 1,000$ we are certainly entering this more complicated regime.

In the higher $l_{\rm max}$ cutoff case (Fig. 3.4), we are showing forecasted constraints for a toy model Gaussian redshift distribution where we vary redshift-integrated galaxy density as well as $l_{\rm max}$. Note that the *values* of number density, redshift distribution, bias, and $l_{\rm max}$ are not independent, as for example a change in the number density (by observing down to lower fluxes) would likely affect the mean galaxy bias. Since we are interested in forecasting parameter *errors* around a fiducial model, we can ignore such dependencies. Note also that we do not explicitly model a redshift dependence of the bias, $b(z)$. This dependence is highly degenerate with the evolution of the number density $N(z)$ when using observables integrated over all redshifts, as we do here. The degeneracy can be reduced by using redshift-binned galaxy auto and CMB lensing-galaxy cross power spectra. We defer such an analysis to a future work.

3.4 Constraints on cosmological parameters

In the following sections we refer to the *unlensed* primary CMB information using the notation CMB *ul*. This term encompasses the TT primary CMB temperature power spectrum, the EE primary CMB E mode information and the TE cross correlation information. Using unlensed spectra ensures that we do not over-count lensing information when the temperature and polarization power spectra are considered in conjunction with the reconstruction-based $\phi\phi$ and ϕG spectra (see Schmittfull et al. (2013); Zahn (2014) for more detailed treatments that quantify the shared information content between these estimators). In some cases we consider the lensed theoretical power spectra for the primary CMB. This is denoted by CMB *le*.

3.4.1 Galaxy properties

In this section we present constraints on parameters describing the large-scale tracer structure probed by the cross correlation with CMB lensing, for both a toy model Gaussian case and for a specifically LSST parameterized distribution. In all cases, we allow the full seven (non-galactic) cosmological parameters to vary. In the case of the toy model describing the populations probed by the galaxy survey, we also vary three parameters describing the galaxy properties: the bias (b), and the mean (μ) and standard deviation (σ) of the assumed Gaussian redshift distribution, shown by the black curve of Fig. 3.1.

Figure 3.2 shows constraints on b, μ and σ for a scenario-A combination of surveys (a galaxy survey with a Gaussian redshift distribution and and *Planck* + 4th. generation CMB experiments). Parameter constraints are shown over a range of galaxy survey sensitivities (galaxy number density per square degree). Different combinations of the lensing and galaxy auto correlations $\phi\phi$, GG, and the lensing galaxy cross correlation ϕG and the primary CMB are shown by lines on the plot. For all three parameters, the addition of ϕG information improves constraints significantly over using CMB + GG alone (solid line to dotted line). The constraints can be improved further by adding $\phi\phi$ information (bottom dot-dashed lines). The addition of CMB lensing information is crucial for constraining galaxy bias, because it helps break degeneracies between bias and other cosmological parameters affecting the amplitude and shape of the galaxy power spectra. The figure also shows that for high number densities the shot noise becomes irrelevant and the forecasts saturate.

Table 3.4 shows constraints on galaxy parameters b and z_0 for an LSST type survey (described in section 3.3 and shown in Eq. (3.9)), for the combination with a 4th generation CMB experiment and *Planck*. z_0 is the single parameter describing the shape of the redshift distribution. When the cross correlation is added to the autocorrelations (CMB ul + $\phi\phi$ + GG case to CMB ul + $\phi\phi$ + GG + ϕG case), the constraints on both the bias and shape parameter improve by $\sim$70%. Interestingly, the constraints on both parameters from CMB ul + GG is only 30% improved from the constraint of CMB ul + ϕG. This shows that the CMB lensing-galaxy correlation contains powerful information on galaxy dynamics, in particular the bias, even without using the galaxy clustering auto power spectrum. The significant improvement in the constraint on the shape parameter z_0 in the combination of all observables (last line) compared to CMB ul + GG or CMB ul + ϕG + $\phi\phi$ shows on the other hand that the galaxy clustering auto correlation becomes much more useful with the addition of CMB lensing information.

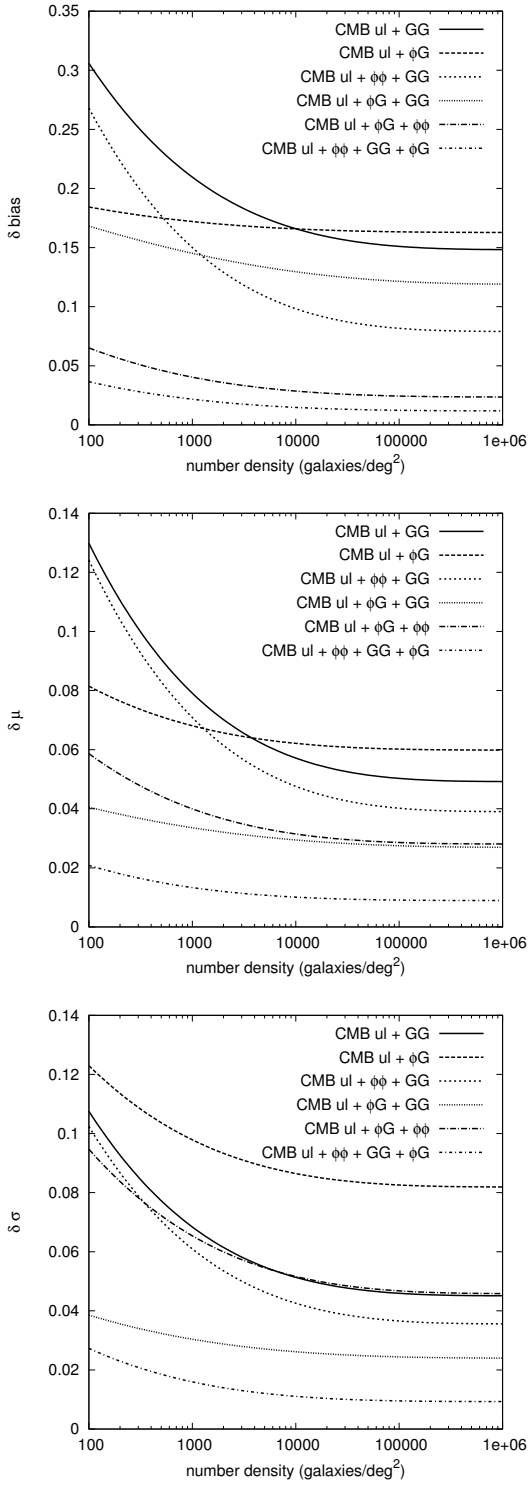

Figure 3.2: Constraints on the 3 galaxy parameters b, μ and σ for a scenario-A experiment combination. Top panel shows the galaxy bias parameter (b), centre panel shows the mean (μ) of the Gaussian distribution, bottom panel shows the sigma (σ) of the Gaussian distribution. The x axes show the number density of galaxies per square degree, and constraints are shown for various combinations of GG, $\phi\phi$ and ϕG with the primary CMB. (1,000 gal/deg^2 $\leftrightarrow$ 0.28 gal/arcmin^2, 10,000 gal/deg^2 $\leftrightarrow$ 2.8 gal/arcmin^2, 100,000 gal/deg^2 $\leftrightarrow$ 28 gal/arcmin^2).

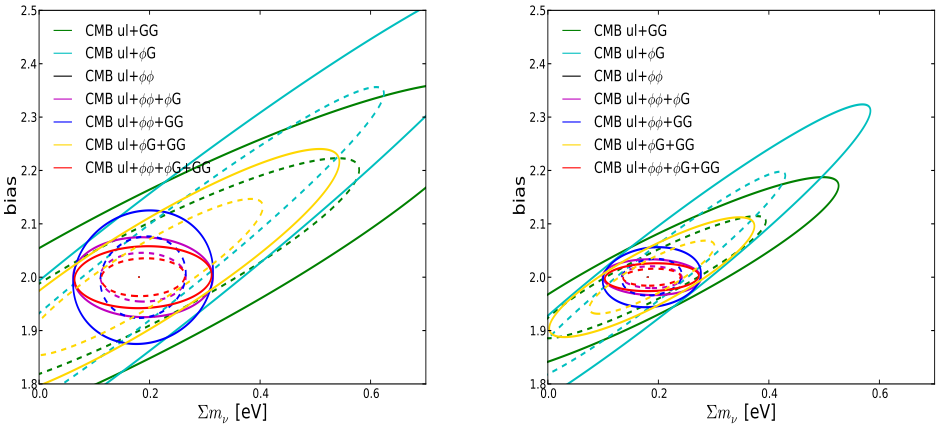

(a) Scenario-C

(b) Scenario-D

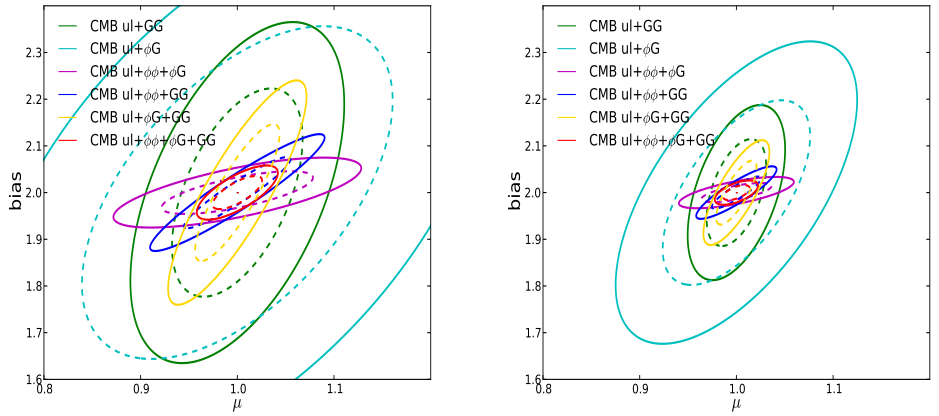

(c) Scenario-C

(d) Scenario-D

Figure 3.3: 1σ (dashed line) and 2σ (solid line) ellipses for various combinations of GG, $\phi\phi$ and ϕG with the primary CMB. Left and right panels show the comparison between a scenario-C (3rd generation CMB) and scenario-D (4th generation CMB) experiment combination. Galaxy survey is Gaussian with number density 1,000 gal/deg^2.

Table 3.4: δb and δz_0 FOR LSST + CMB

scenario-B	δz_0	δb
CMB ul $+GG$	0.010	0.065
CMB ul + ϕG	0.015	0.093
CMB ul + $\phi\phi$ + ϕG	0.010	0.017
CMB ul + ϕG + GG	0.002	0.040
CMB ul + $\phi\phi$ + GG	0.007	0.060
CMB ul + $\phi\phi$ + GG + ϕG	0.002	0.016

Constraints on the galaxy parameters b and z_0 for a scenario-B experiment combination (LSST galaxy survey with *Planck* + 4th generation CMB). Values are shown for different combinations of GG, $\phi\phi$ and ϕG with the primary CMB.

Figure 3.3 shows the 1σ and 2σ ellipses for various parameters for scenario-C and scenario-D experiment combinations. (The galaxy survey is Gaussian with a number density of 1,000 gal/deg^2. The difference between scenario-C and scenario-D is that the former includes a 3rd generation CMB survey, whilst the latter includes a 4th generation CMB survey.) The top two panels show a comparison of the $\sum m_\nu$ and b parameters for both scenario-C (left) and scenario-D (right). The two parameters are highly degenerate when only including the galaxy auto power or galaxy-lensing cross correlation. We see again that CMB ul + ϕG combination does almost as well as the CMB ul + GG combination. The improvement in the CMB ul + ϕG cross combination is $\sim$50% for both parameters when upgrading to scenario-D from scenario-C. The lower two panels show a comparison of the redshift distribution mean (μ) and bias parameter for scenario-C (left) and scenario-D (right). The improvement in the μ parameter is $\sim$40% when upgrading to scenario-D from scenario-C. In all cases we see that adding the $\phi\phi$ lensing auto correlation to the CMB ul $+GG$ (green line to blue line) or CMB ul + ϕG (cyan line to purple line) improves the constraints significantly, because the lensing auto power constrains neutrino mass more directly. There is also a good improvement in the constraints when ϕG is added to the CMB ul + GG (green line to yellow line), although the improvement is more dramatic with the addition of the lensing autocorrelation. In both choices of parameter pairs, when comparing scenario-C and scenario-D, the CMB ul $+GG$ constraints improve about as much as the CMB ul + ϕG constraints.

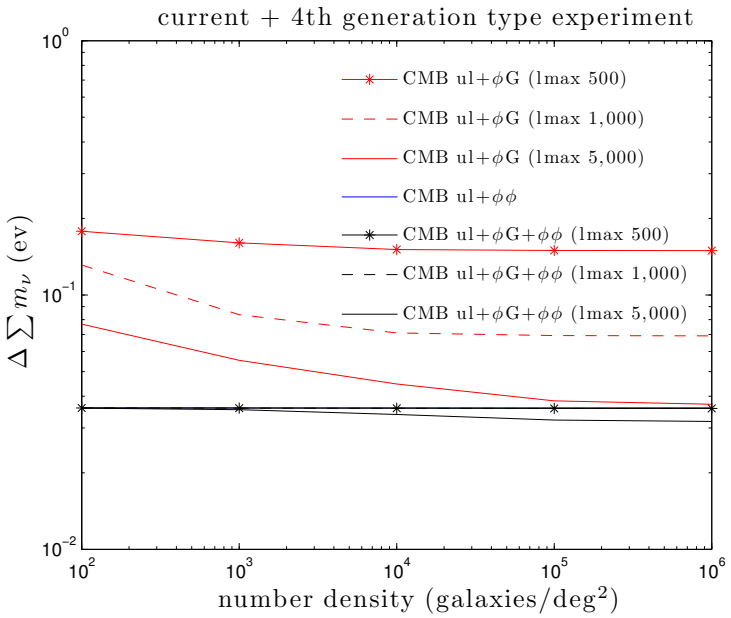

Figure 3.4: $\Delta \sum m_\nu$ for scenario-G. Constraints in the y axis are shown in electron volts, the x axis shows number density of galaxies observed per square degree. Forecasts are shown for different cutoff values of multipole $l_{\rm max}$=500, 1,000, 5,000.

3.4.2 Massive neutrinos and reionization optical depth

In this section we present forecasts on the non-galactic cosmological parameters: the neutrino mass sum $\sum m_\nu$, and the optical depth τ due to free electrons since the epoch of reionization.

Figure 3.4 shows the $\sum m_\nu$ constraint for scenario-G for different cutoff values, $l_{\rm max} = 500$, $l_{\rm max} = 1,000$, $l_{\rm max} = 5,000$. For each value of $l_{\rm max}$ the primary CMB is shown in combination with the ϕG cross correlation (red lines), and the cross correlation plus lensing auto-correlation $\phi G + \phi\phi$ (black lines). These lines can be compared to that of the primary CMB plus only the CMB lensing auto-correlation $\phi\phi$ (blue line). (Remember that the primary CMB is unlensed and includes the TT, EE and TE correlations.) In this scenario, the σ of the redshift distribution was fixed, but the b and μ parameters were allowed to vary with a 20% prior in order to allow matrix inversions. Using a prior of e.g., 40% made negligible difference to the constraints, as did fixing the μ parameter rather than varying it. We see that adding the ϕG information to the CMB ul + $\phi\phi$ combination (blue line to black lines) leads to negligible improvement unless one allows $l_{\rm max} = 5,000$. For a conservative value of $l_{\rm max} = 500$, the combination of the unlensed CMB and ϕG does not give useful constraints. If we consider a less conservative $l_{\rm max} = 1,000$, the CMB ul

Table 3.5: $\Delta \sum m_\nu$ FOR LSST + CMB

	$\Delta \sum m_\nu$ (scenario-E)	$\Delta \sum m_\nu$ (scenario-F)
CMB ul only	0.328	0.201
CMB le	0.055	0.040
CMB ul + $\phi\phi$	0.051	0.036
CMB ul + GG	0.122	0.059
CMB ul + ϕG	0.219	0.119
CMB ul + $\phi\phi$ + ϕG	0.051	0.035
CMB ul + GG + ϕG	0.114	0.058
CMB ul + $\phi\phi$ + GG	0.050	0.034
CMB ul + $\phi\phi$ + GG +ϕG	0.044	0.027

Constraints in electron volts on the $\sum m_\nu$ parameter for an LSST type galaxy survey (Eq. (3.9)) for scenario-E (3rd generation CMB) and scenario-F (4th generation CMB). Constraints are shown for combinations of GG, $\phi\phi$ and ϕG with the primary CMB. (Note that the CMB le does not include any BB correlations).

+ ϕG combination becomes more valuable, and if we consider an optimistic $l_{\rm max} = 5,000$ then the constraint becomes comparable to that of the CMB ul + $\phi\phi$ line. With optimistic $l_{\rm max}$ limits, the ϕG cross correlation could provide a good independent check on the $\sum m_\nu$ parameter. It is worth mentioning that while the CMB ul + ϕG combination places better constraints than the CMB ul does alone, what we actually measure is the lensed primary CMB, and this constrains the $\sum m_\nu$ much better than the cross correlation and almost as well as the CMB lensing autocorrelation for very optimistic surveys (see Table 3.5). (When we consider the $\phi\phi$ correlation in combination with the primary CMB, we always use the unlensed CMB to avoid over-counting the lensing effect).

Tables 3.5 and 3.6 show constraints on the $\sum m_\nu$ and τ parameters for an LSST type galaxy survey (described in Eq. (3.9)). In this case the bias parameter was set to a fiducial value of $b = 1.84$.

Table 3.5 shows constraints on $\sum m_\nu$ for scenario-E and scenario-F. The only difference between scenario-E and scenario-F is that the former includes a 3rd generation CMB experiment, while the latter includes a 4th generation CMB experiment. In the same trend as the Gaussian redshift distribution galaxy survey, using the lensed CMB vs the unlensed CMB gives dramatic improvements, almost an order of magnitude in this case.

The lensed CMB alone is much better than the CMB ul + ϕG, and the addition of ϕG to CMB ul + $\phi\phi$ gives negligible improvement. However, the improvement in the neutrino constraint from CMB ul + GG + $\phi\phi$ to CMB ul + GG + $\phi\phi$ + ϕG is 10% for a 3rd generation CMB experiment and 20% for a 4th generation. This shows that when the redshift distribution is well known, the addition of ϕG helps break degeneracies between cosmological and galaxy parameters in GG.

In table 3.6, we show the constraint on τ for various scenarios. Scenario-H and scenario-F use the full 7 parameter non-galactic cosmology where scenario-H includes *Planck* and scenario-F includes a 4th generation CMB survey. Also shown are scenario-I and scenario-J. These two scenarios include only the ΛCDM 6 non-galactic cosmology parameters, excluding massive neutrinos. Scenario-I includes a current type CMB survey and scenario-J includes a 4th generation CMB survey. When the neutrino mass sum is fixed, the constraint on τ improves significantly for many cases. This highlights the importance of including the neutrino mass sum as an unknown parameter in the analysis.

While ϕG reduces degeneracies between cosmological parameters inherent in TT+GG, the improvement in the τ constraint going from TT + GG + $\phi\phi$ to TT + GG + $\phi\phi$ + ϕG is small. Note that while large-scale polarization information from *Planck* or future experiments will yield the tightest constraints on τ, the addition of $\phi\phi$ information alone to the temperature power spectrum (TT) improves the τ constraints significantly. The constraint from a 4th generation CMB experiment *without* large-scale polarization information will be comparable to that from current large-scale polarization measurements from WMAP (Hinshaw et al., 2013) and will offer a good independent check on the constraint from Planck polarization, to be published in 2014, which could be dominated by uncertainty in the polarization foregrounds.

There is a geometric degeneracy in the unlensed CMB between the $\sum m_\nu$ vs Ω_Λ parameters which CMB lensing significantly helps to constrain (e.g. Stompor & Efstathiou (1999) and Sherwin et al. (2011)). We explored whether the cross correlation could bring any additional information to break the degeneracy further. As expected, adding the CMB lensing auto correlation to the primary CMB improved the constraints dramatically, due to the breaking of the geometric degeneracy. However, after the addition of the $\phi\phi$ correlation, additional information from both GG and ϕG made negligible improvement to the constraint on dark energy. In the absence of the $\phi\phi$ correlation, the addition of GG or ϕG also made negligible improvement on the constraint from the primary CMB alone.

Table 3.6: $\Delta\tau$ FOR LSST + CMB

ΛCDMν	$\Delta\tau$ (scenario-H)	$\Delta\tau$(scenario-F)
TT len	0.084	0.036
CMB le	0.004	0.003
TT+$\phi\phi$	0.041	0.015
TT+GG	0.064	0.056
TT+ϕG	0.068	0.055
TT+$\phi\phi$+ϕG	0.039	0.014
TT+GG+ϕG	0.037	0.025
TT+GG+$\phi\phi$	0.028	0.015
TT+GG+$\phi\phi$ +ϕG	0.028	0.014
ΛCDM	$\Delta\tau$ (scenario-I)	$\Delta\tau$(scenario-J)
TT len	0.027	0.013
CMB le	0.004	0.003
TT+$\phi\phi$	0.020	0.010
TT+GG	0.019	0.018
TT+ϕG	0.047	0.033
TT+$\phi\phi$+ϕG	0.020	0.010
TT+GG+ϕG	0.019	0.016
TT+GG+$\phi\phi$	0.017	0.010
TT+GG+$\phi\phi$ +ϕG	0.016	0.007

Constraints on the τ parameter for an LSST type galaxy survey (Eq.(3.9)). Constraints are shown for a number of scenarios for combinations of TT, CMB, $\phi\phi$, GG and ϕG. Scenarios H and I are *Planck* like, scenarios F and J are 4th generation CMB like.

3.5 Summary

Our analysis is intended to begin to answer the open question of how much information about cosmology is contained in the CMB lensing - galaxy cross correlation. We have used a simple Fisher model where we included all correlations between temperature, polarization, galaxy over-density, and CMB lensing maps. We constrain both galactic and non-galactic cosmological parameters simultaneously, to explore degeneracies in these spectra between the underlying cosmology and galaxy dynamics.

In the case of the galaxy parameters, the ϕG cross correlation is very useful. In all cases the addition of the ϕG cross correlation to the $\phi\phi$ and GG auto correlations improves the constraints significantly, and CMB ul + ϕG is comparable to CMB ul + GG. We also find that the addition of CMB lensing information or any improvements in the primary CMB significantly improve the constraints on galaxy parameters. This is because the CMB lensing and primary CMB information give tighter constraints on the non-galactic cosmological parameters, allowing degeneracies with galaxy parameters to be broken.

For non-galactic cosmology, we find that in the case of the $\sum m_\nu$, once the $\phi\phi$ and GG auto correlations are considered, the ϕG cross correlation adds little improvement. We have imposed a conservative $l_{\rm max} = 500$ for the ϕG cross correlation however, and see that when this is relaxed, the cross correlation does offer useful information, up to the same level as the auto correlations for ambitious values of $l_{\rm max}$. Although for now it may be unrealistic to extend the cross correlation information to such small scales, with some improvement in the non-linear modelling one could hope that the cross correlation provides useful independent checks of constraints derived from the GG auto-correlation. In Table 3.6 we also quantify the near future constraints available on the τ parameter when the CMB lensing information is used. We note that the $TT + \phi\phi$ correlation will constrain τ to $<$20%, which will provide a good independent check on the epoch of reionization, given galactic foreground uncertainties in the polarization constraints.

Although there are a host of issues concerning the reliability of information from galaxy surveys, we expect our most conservative scenarios to be robust. For the GG and ϕG observables we have chosen a conservative $l_{\rm max} = 500$ in all but one of our simulations. This value is just past the scale of the onset of non-linearities ($l_{\rm non-linear} \gtrsim 300$), and should be well modelled in the near future. Furthermore, we expect the ϕG to be less sensitive to non-linear effects. Although we have not modelled the non-linearity of the bias, our forecasts should not change much since we are only considering scales for which simulations have shown the bias is still linear. We expect that a modelling of the redshift

distribution of the bias would only *improve* our constraints, since it would help to break a degeneracy between the redshift distribution and bias parameters.

Chapter 4

CMB Lensing and the Primordial Squeezed Bispecrum

The contents of this chapter are based on work presented in Pearson et al. (2012) and represent work done by the author in collaboration with Antony Lewis and Donough Regan. Notation in this chapter differs slightly such that the symbol ϕ will no longer refer to the lensing potential. Instead the symbol $\phi_{\mathbf{ab}}$ is used to refer to the angle between the vectors **a** and **b**. A squeezed bispectrum or trispectrum produced by local primordial non-Gaussianity is observable in the CMB, and if observed would give a powerful way to rule out simple single-field inflation models and strongly constrain general properties of inflation. The local non-Gaussianity produced in the CMB can be thought of as a modulation of small-scale perturbations by large-scale modes, so over a large overdensity there will be more (or less) small-scale power than over an underdensity, depending on the sign of the non-Gaussianity. However if we observe the small-scale modes they will be gravitationally lensed, so in the squeezed limit we expect to see a modulation of the *lensed* small-scale power spectrum due to large-scale modes. This may be important because lensing smooths out acoustic structures, changing the detailed shape of the bispectrum and trispectrum. Previous work (Hanson et al., 2009) has shown that for the temperature bispectrum due only to local primordial non-Gaussianity, the bias due to this change in shape is very small. However since the shape is changed, accounting for lensing might be important to correctly identify the form of the non-Gaussianity; for example a different shape which is orthogonal to the unlensed bispectrum will not generally be orthogonal to the lensed bispectrum. In this work we give new simple approximations for the effect of lensing on the squeezed CMB temperature and polarization bispectra which allow the effects to be calculated easily. We test these approximations against simulations, and

quantify the importance of the lensing at different levels of primordial non-Gaussianity.

Previous work has investigated the lensing bispectrum in detail, its potential bias on local non-Gaussianity estimators, and its impact on the variance of the primordial non-Gaussianity estimators (Smith & Zaldarriaga, 2011; Serra & Cooray, 2008; Hanson et al., 2009; Lewis et al., 2011). The bispectrum produced by lensing turns out to be significant, corresponding to a projection of $f_{\rm NL} \sim 9$ onto the local shape, and should be detectable by Planck. However the effect is easily modelled and subtracted since the detailed shape of the lensing bispectrum is actually very different from the local shape (Lewis et al., 2011). Here we address the different issue of how lensing affects any other primordial bispectrum that we might want to observe, and assess whether the change due to lensing is important. We give simple analytic forms for the CMB bispectrum that are quite accurate in the highly squeezed limit, and show how general squeezed CMB bispectra can be decomposed into modes of distinct angular dependence.

4.1 Lensed squeezed bispectra

Lensing deflection angles are only a few arcminutes, though coherent on degree scales. As such, lensing only has a large effect on relatively small scales. Local bispectra depend on three wave numbers $\mathbf{l}_1$, $\mathbf{l}_2$, $\mathbf{l}_3$ (we restrict to $l_1 \leq l_2 \leq l_3$ for convenience), and most of the signal is in squeezed triangles with $l_1 \ll l_2, l_3$. It is therefore a good approximation in many cases to take the largest-scale mode to be unlensed: $\tilde{T}(\mathbf{l}_1) \approx T(\mathbf{l}_1)$. This approximation greatly simplifies many calculations with very little loss of accuracy, and also makes a non-perturbative analysis tractable, as shown for the CMB lensing bispectra in Lewis et al. (2011). For the moment we only consider temperature bispectra in the flat-sky approximation, and hence wish to calculate

$$\langle T(\mathbf{l}_1)\tilde{T}(\mathbf{l}_2)\tilde{T}(\mathbf{l}_3)\rangle \approx \langle \tilde{T}(\mathbf{l}_1)\tilde{T}(\mathbf{l}_2)\tilde{T}(\mathbf{l}_3)\rangle = \frac{1}{2\pi}\tilde{b}_{l_1 l_2 l_3}\delta(\mathbf{l}_1+\mathbf{l}_2+\mathbf{l}_3), \tag{4.1}$$

where $\tilde{b}_{l_1 l_2 l_3}$ is the reduced lensed bispectrum. The approximation was previously called the linear (unlensed) short-leg approximation. A general result can be formulated for any shape and the result for the lensed temperature bispectrum obtained from the linear short-leg approximation is correct to quadratic order in a squeezed expansion.

We can now proceed to calculate the lensed bispectra, following the methods and notation used for calculating the lensed CMB power spectra via lensed correlation functions in Lewis & Challinor (2006), with

$$\tilde{T}(\mathbf{l}) = \int \frac{d^2\mathbf{x}}{2\pi} T(\mathbf{x}+\boldsymbol{\alpha}) e^{-i\mathbf{l}\cdot\mathbf{x}} \tag{4.2}$$

where a tilde denotes the lensed field and $\boldsymbol{\alpha}$ is the lensing deflection angle. Hence in the unlensed short-leg approximation

$$\begin{aligned}\langle T(\mathbf{l}_1)\tilde{T}(\mathbf{l}_2)\tilde{T}(\mathbf{l}_3)\rangle &= \int \frac{d^2\mathbf{x}_2}{2\pi}\frac{d^2\mathbf{x}_3}{2\pi}\frac{d^2\mathbf{l}'_2}{2\pi}\frac{d^2\mathbf{l}'_3}{2\pi} \\ &\quad \times\langle T(\mathbf{l}_1)T(\mathbf{l}'_2)T(\mathbf{l}'_3)e^{-i\mathbf{l}_2\cdot\mathbf{x}_2}e^{-i\mathbf{l}_3\cdot\mathbf{x}_3}e^{i\mathbf{l}'_2\cdot(\mathbf{x}_2+\boldsymbol{\alpha}_2)}e^{i\mathbf{l}'_3\cdot(\mathbf{x}_3+\boldsymbol{\alpha}_3)}\rangle. \end{aligned} \tag{4.3}$$

The correlation between $T(\mathbf{l}_1)$ and the lensing potentials gives rise to the lensing bispectrum. We are not interested in this term here, and so only keep remaining terms where $\boldsymbol{\alpha}$ can be taken to be uncorrelated to T. Hence

$$\langle T(\mathbf{l}_1)\tilde{T}(\mathbf{l}_2)\tilde{T}(\mathbf{l}_3)\rangle = \frac{1}{(2\pi)^2}\int \frac{d^2\mathbf{x}_2}{2\pi}\frac{d^2\mathbf{x}_3}{2\pi}\frac{d^2\mathbf{l}'_2}{2\pi} b_{l_1l'_2l'_3}e^{i\mathbf{x}_2\cdot(\mathbf{l}'_2-\mathbf{l}_2)}e^{i\mathbf{x}_3\cdot(\mathbf{l}'_3-\mathbf{l}_3)}\langle e^{i\mathbf{l}'_2\cdot\boldsymbol{\alpha}_2}e^{i\mathbf{l}'_3\cdot\boldsymbol{\alpha}_3}\rangle \tag{4.4}$$

where $\mathbf{l}'_3 = -\mathbf{l}_1 - \mathbf{l}'_2$ and $\boldsymbol{\alpha}_i \equiv \boldsymbol{\alpha}(\mathbf{x}_i)$. From statistical homogeneity (isotropy on the sky) the expectation value is only a function of $\mathbf{r} \equiv \mathbf{x}_2 - \mathbf{x}_3$, so integrating out $\mathbf{x}_2 + \mathbf{x}_3$ we obtain

$$\langle T(\mathbf{l}_1)\tilde{T}(\mathbf{l}_2)\tilde{T}(\mathbf{l}_3)\rangle = \frac{1}{(2\pi)}\delta(\mathbf{l}_1+\mathbf{l}_2+\mathbf{l}_3)\int \frac{d^2\mathbf{r}}{2\pi}\frac{d^2\mathbf{l}'_2}{2\pi} b_{l_1l'_2l'_3}e^{i\mathbf{r}\cdot(\mathbf{l}'_2-\mathbf{l}_2)}\langle e^{i\mathbf{l}'_2\cdot\boldsymbol{\alpha}_2}e^{i\mathbf{l}'_3\cdot\boldsymbol{\alpha}_3}\rangle. \tag{4.5}$$

This is very similar in form to what is required for lensing of the temperature power spectrum (Seljak, 1996; Challinor & Lewis, 2005; Lewis & Challinor, 2006). Let's define $\mathbf{l}' \equiv (\mathbf{l}'_2 - \mathbf{l}'_3)/2 = \mathbf{l}'_2 + \mathbf{l}_1/2$ and $\mathbf{l} \equiv (\mathbf{l}_2 - \mathbf{l}_3)/2 = \mathbf{l}_2 + \mathbf{l}_1/2$ to encode the wavevectors of the small-scale modes, so that

$$\mathbf{l}'_2\cdot\boldsymbol{\alpha}_2 + \mathbf{l}'_3\cdot\boldsymbol{\alpha}_3 = \mathbf{l}'\cdot(\boldsymbol{\alpha}_2-\boldsymbol{\alpha}_3) - \frac{\mathbf{l}_1}{2}\cdot(\boldsymbol{\alpha}_2+\boldsymbol{\alpha}_3). \tag{4.6}$$

Then neglecting non-Gaussianity of the lensing potentials,

$$\tilde{b}_{l_1l_2l_3} = \int \frac{d^2\mathbf{r}}{2\pi}\frac{d^2\mathbf{l}'}{2\pi} b_{l_1l'_2l'_3}e^{i\mathbf{r}\cdot(\mathbf{l}'-\mathbf{l})}\exp\left(-\frac{1}{2}\left\langle\left[\mathbf{l}'\cdot(\boldsymbol{\alpha}_2-\boldsymbol{\alpha}_3) - \frac{\mathbf{l}_1}{2}\cdot(\boldsymbol{\alpha}_2+\boldsymbol{\alpha}_3)\right]^2\right\rangle\right) \tag{4.7}$$

$$\begin{aligned} &= \int \frac{d^2\mathbf{r}}{2\pi}\frac{d^2\mathbf{l}'}{2\pi} b_{l_1l'_2l'_3}e^{i\mathbf{r}\cdot(\mathbf{l}'-\mathbf{l})}\exp\Bigg(-\frac{1}{2}\Bigg[l'^2\left(\sigma^2(r)+\cos 2\phi_{l'r}C_{\mathrm{gl},2}(r)\right) \\ &\qquad +\frac{l_1^2}{4}\left(C_{\mathrm{gl}}(0)+C_{\mathrm{gl}}(r)-\cos 2\phi_{l_1r}C_{\mathrm{gl},2}(r)\right)\Bigg]\Bigg), \end{aligned} \tag{4.8}$$

where $\sigma^2(r_{32}) \equiv \langle(\boldsymbol{\alpha}_3-\boldsymbol{\alpha}_2)^2\rangle/2$, and $C_{\mathrm{gl},2}(r), C_{\mathrm{gl}}(r)$ are defined as in Lewis & Challinor (2006) (sec. 4.2).

For squeezed shapes the second term in the exponential $\mathcal{O}(l_1^2 C_{\mathrm{gl}}(0))$ is very small (same order as things we've already neglected by using the unlensed short-leg approximation) and hence

$$\tilde{b}_{l_1l_2l_3} \approx \int \frac{d^2\mathbf{r}}{2\pi}\frac{d^2\mathbf{l}'}{2\pi} b_{l_1l'_2l'_3}e^{i\mathbf{r}\cdot(\mathbf{l}'-\mathbf{l})}\exp\left(-\frac{l'^2}{2}[\sigma^2(r)+\cos 2\phi_{l'r}C_{\mathrm{gl},2}(r)]\right). \tag{4.9}$$

If $b_{l_1 l_2' l_3'}$ were a function only of l_1 and $|\mathbf{l}'|$, this could be evaluated trivially using exactly the same form as the result for lensing of the power spectrum.

More generally we can parameterize the bispectrum in terms of $l_1, l \equiv |\mathbf{l}_3 - \mathbf{l}_2|/2, \phi_{l l_1}$ instead of l_1, l_2, l_3, where $\phi_{l l_1}$ is the angle between $\mathbf{l}$ and $\mathbf{l}_1$. We can then expand the angular dependence of the bispectrum as

$$b_{l_1 l_2 l_3} = \sum_m \bar{b}^m_{l_1 l} \, e^{m i \phi_{l l_1}} \tag{4.10}$$

(see Lewis (2011) for further discussion). From rotational invariance m should be even, and for parity-invariant fields the dependence on $\phi_{l_1 l}$ is only via $|\phi_{l_1 l}|$, so we can equivalently write

$$b_{l_1 l_2 l_3} = \sum_m b^m_{l_1 l} \cos(m \phi_{l l_1}) \tag{4.11}$$

where m is even and $m \geq 0$.

Using the expansion of Eq. (4.10) in Eq. (4.9), the angular integrals can then be done giving the lensed bispectrum moments in terms of integrals of modified and unmodified Bessel functions:

$$\tilde{b}^m_{l_1 l} \approx \int r dr J_m(l r) \int dl' l' b^m_{l_1 l'} e^{-l'^2 \sigma^2(r)/2} \sum_n I_n[l'^2 C_{\mathrm{gl},2}(r)/2] J_{2n+m}(l' r). \tag{4.12}$$

This shows that lensing, which is on average a statistically isotropic process, does not mix the angular dependence of the squeezed bispectra: the lensed bispectrum $\tilde{b}^m_{l_1 l}$ depends only on the unlensed bispectrum with the same m. For isotropic primordial bispectra in the squeezed limit the angular average $b^0_{l_1 l}$ is expected to dominate over other modes (unless the large-scale modes generate local anisotropy), so to that approximation one would be applying power spectrum lensing to angle-averaged bispectrum slices $b^0_{l_1 l}$ for each l_1. Lensing of the $b^2_{l_1 l}$ moments is mathematically identical to power spectrum lensing of the C_l^{TE} power spectrum.

On the flat sky the Fisher correlation between two different bispectra is usually defined (for small signals) by (Hu, 2000)

$$F(b, b') \;=\; \frac{1}{2\pi^2} \int l_1 \mathrm{d}l_1 \int \mathrm{d}^2\mathbf{l}_2 \frac{b_{l_1 l_2 l_3} b'_{l_1 l_2 l_3}}{6 C_{l_1} C_{l_2} C_{l_3}}, \tag{4.13}$$

which is zero if the bispectra are orthogonal. If the bispectra are both squeezed we can expand in terms of angular dependence, and obtain

$$F(b, b') = \frac{1}{\pi} \int l_1 \mathrm{d}l_1 \int l \mathrm{d}l \sum_m \frac{b^m_{l_1 l} b'^{m*}_{l_1 l}}{6 C_{l_1} C_l^2} \left(1 + \mathcal{O}(l_1^2/l^2)\right). \tag{4.14}$$

As might be expected bispectrum components with $m \neq m'$ are orthogonal in the squeezed limit. Since lensing does not change the angular dependence, this will remain true after

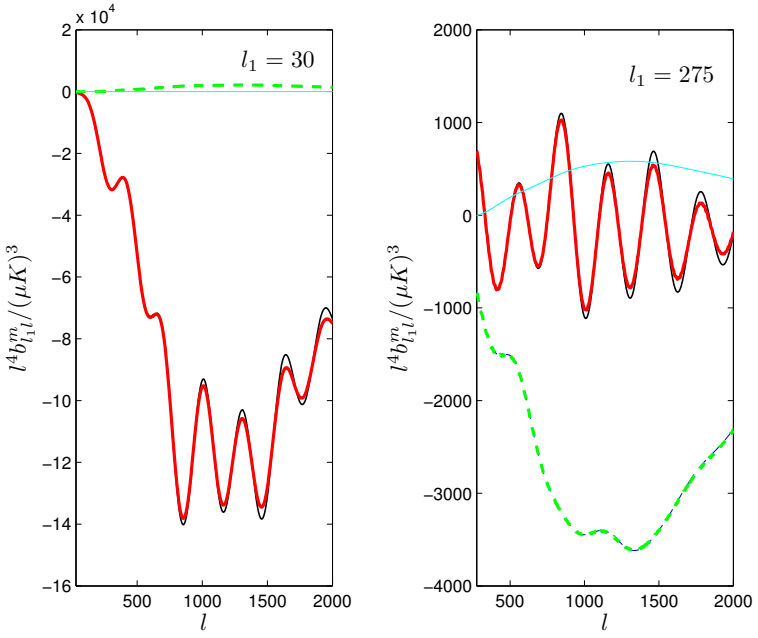

Figure 4.1: The temperature CMB bispectrum from local non-Gaussianity ($f_{\rm NL} = 1$) with $l_1 = 30$ (left) and $l_1 = 275$ (right), projected into the isotropic component (solid lines), $m = 2$ quadrupole (green) and $m = 4$ (cyan) octopole parts. Thick lines are lensed using the approximation described in the text, thin lines show the unlensed bispectrum. The anisotropic components are small on super-horizon scales, and on smaller scales are relatively smooth so lensing has little effect.

lensing. If the correlation is defined without the power spectra in the denominator (or equivalently for constant white-noise power spectra, or using the bispectrum of whitened fields) this remains true for all triangles.

4.1.1 Local non-Gaussianity

The case of most immediate interest is when the primordial non-Gaussianity is of local (scalar) form, parameterized by $f_{\rm NL}$. In this form of non-Gaussianity small-scale modes are modulated by the large-scale scalar modes. In the squeezed limit, since the modulation is scalar, the modulation is expected to be isotropic, i.e. $m = 0$. Specifically the bispectrum is given in terms of 2-point correlation functions of the primordial curvature perturbation $P_\zeta(k)$ by

$$\begin{aligned} b(k_1,k_2,k_3) &= 2\frac{3}{5} f_{\rm NL}[P_\zeta(k_1)P_\zeta(k_2) + P_\zeta(k_1)P_\zeta(k_3) + P_\zeta(k_2)P_\zeta(k_3)] \\ &= 4\frac{3}{5} f_{\rm NL} P_\zeta(k_1)P_\zeta(k)\left[1 + \left(\frac{k_1}{k}\right)^2 \frac{9+15\cos(2\phi)}{16} + \ldots\right], \end{aligned} \quad (4.15)$$

where in the second line we expanded in k_1/k for a scale-invariant spectrum, ϕ is the angle between the long and the short-scale modes, and $\mathbf{k} \equiv (\mathbf{k}_3 - \mathbf{k}_2)/2$. Thus in the squeezed limit there is no m dependence as expected, with leading corrections of $\mathcal{O}((k_1/k)^2)$ coming from the effect of gradients in the modulation.

Evolution until last scattering will modify this for observations of the CMB. However for l_1 corresponding to scales that are super-horizon at recombination ($l_1 \ll 100$), the corresponding perturbation can be taken to be constant across the last-scattering surface. The small-scale temperature is then modulated by $1 + (6f_{\rm NL}/5)\zeta_*$, and hence the local model bispectrum is

$$\langle T(\mathbf{l}_1)T(\mathbf{l}_2)T(\mathbf{l}_3)\rangle \approx C_{l_1}^{T\zeta_*}\left\langle \frac{\delta}{\delta\zeta_*(\mathbf{l}_1)^*}\left(T(\mathbf{l}_2)T(\mathbf{l}_3)\right)\right\rangle \tag{4.16}$$

$$= \frac{1}{2\pi}\delta(\mathbf{l}_1+\mathbf{l}_2+\mathbf{l}_3)\frac{6}{5}f_{\rm NL}C_{l_1}^{T\zeta_*}(C_{l_2}+C_{l_3}), \tag{4.17}$$

where ζ_* is the primordial curvature perturbation at last scattering, $\zeta_*(\hat{\mathbf{n}}) = \zeta(\hat{\mathbf{n}}, r_*)$ and r_* is the distance to last-scattering. We can see immediately that on the lensed sky, where the lenses are taken to be uncorrelated to the ζ_*, the same result is obtained simply replacing C_l with the lensed $\tilde{C}_l$, and hence it should be no surprise that local bispectrum lensing is well modelled by power spectrum lensing. (Note that this low l_1 limit is particularly interesting because non-linear evolution effects are under control analytically and known to be small (Creminelli et al., 2011).)

When l_1 is larger the situation is more complicated since the modulation can no longer be approximated as being constant through last scattering. However the local bispectrum shape is still squeezed, so we can expect that our full result of Eq. (4.12) will accurately describe the effect of lensing where only the lowest angular bispectrum moments are required. Numerically, using the fully-sky analogue of the angular decomposition, we find that the full sky temperature local bispectrum (calculated with CAMB) projected into only its isotropic part is $\sim 96\%$ correlated to the full result ($l_{\rm max} = 2000$, no noise), and 99% correlated if both the $m = 0$ and $m = 2$ (isotropic and quadrupolar) moments are retained. The quadrupolar moments are more important for larger (sub-horizon) $l_1 \gtrsim 200$. This is because the triangles with a given l have small-scale modes with transfer functions involving l_2 and l_3 that vary by $\pm l_1/2$ depending on ϕ, the angle between $\mathbf{l}_1$ and $\mathbf{l}$; for l_1 comparable to or larger than the separation of the acoustic peaks there is a significant variation in these transfer functions, giving a significant $m \neq 0$ component to the squeezed CMB bispectrum for larger l_1. See Fig. 4.1.

The unlensed short-leg approximation is expected to be quite accurate since almost all the signal to noise in local non-Gaussianity is at $l_1 \lesssim 500$ for Planck sensitivity, where lens-

ing effects are still small. We check these approximations numerically below by comparison with full-sky simulations.

4.1.2 Polarization

To consider polarization bispectra in the flat-sky approximation we need the lensed E and B modes given by the polarization analogue of Eq. (4.2). Taking the unlensed B modes to be zero, it follows from the definitions given in Lewis & Challinor (2006) that:

$$\tilde{E}(\mathbf{l}) = \int \frac{d^2\mathbf{x}}{2\pi}\frac{d^2\mathbf{l}'}{2\pi} E(\mathbf{l}') e^{i\mathbf{l}'\cdot\boldsymbol{\alpha}} e^{i\mathbf{x}\cdot(\mathbf{l}'-\mathbf{l})} \cos 2\phi_{l'l}, \tag{4.18}$$

$$\tilde{B}(\mathbf{l}) = \int \frac{d^2\mathbf{x}}{2\pi}\frac{d^2\mathbf{l}'}{2\pi} E(\mathbf{l}') e^{i\mathbf{l}'\cdot\boldsymbol{\alpha}} e^{i\mathbf{x}\cdot(\mathbf{l}'-\mathbf{l})} \sin 2\phi_{l'l}\,, \tag{4.19}$$

and $\phi_{l'l}$ is the angle between $\mathbf{l}'$ and $\mathbf{l}$. We can then use the lensed E and B modes to calculate the polarization bispectra combinations in the unlensed short-leg approximation as before:

$$\langle X(\mathbf{l}_1)\tilde{Y}(\mathbf{l}_2)\tilde{Z}(\mathbf{l}_3)\rangle \approx \langle \tilde{X}(\mathbf{l}_1)\tilde{Y}(\mathbf{l}_2)\tilde{Z}(\mathbf{l}_3)\rangle = \frac{1}{2\pi}\tilde{b}^{XYZ}_{l_1l_2l_3}\delta(\mathbf{l}_1+\mathbf{l}_2+\mathbf{l}_3), \tag{4.20}$$

where X, Y and Z can be any of T, E and B. Since the primordial B modes are small, we expect the effect of lensing on the b^{TEB} and b^{EEB} bispectra to be unimportant, and do not calculate them here.

XTE bispectra

Following the same steps as for the temperature case, the first combination gives

$$\begin{aligned}\langle X(\mathbf{l}_1)\tilde{T}(\mathbf{l}_2)\tilde{E}(\mathbf{l}_3)\rangle \;=\; & \int \frac{d^2\mathbf{x}_2}{2\pi}\frac{d^2\mathbf{x}_3}{2\pi}\frac{d^2\mathbf{l}'_2}{2\pi}\frac{d^2\mathbf{l}'_3}{2\pi}\langle X(\mathbf{l}_1)T(\mathbf{l}'_2)E(\mathbf{l}'_3) \\ & \times e^{-i\mathbf{l}_2\cdot\mathbf{x}_2} e^{i\mathbf{l}'_2\cdot(\mathbf{x}_2+\boldsymbol{\alpha}_2)} e^{i\mathbf{l}'_3\cdot\boldsymbol{\alpha}_3} e^{i\mathbf{x}_3\cdot(\mathbf{l}'_3-\mathbf{l}_3)} \cos(2\phi_{l'_3l_3})\rangle.\end{aligned} \tag{4.21}$$

Keeping terms where $\boldsymbol{\alpha}$ is uncorrelated to T and E, and writing the expectation value as a function of $\mathbf{r} \equiv \mathbf{x}_2 - \mathbf{x}_3$ we have

$$\langle X(\mathbf{l}_1)\tilde{T}(\mathbf{l}_2)\tilde{E}(\mathbf{l}_3)\rangle = \frac{1}{(2\pi)}\delta(\mathbf{l}_1+\mathbf{l}_2+\mathbf{l}_3)\int \frac{d^2\mathbf{r}}{2\pi}\frac{d^2\mathbf{l}'_2}{2\pi} b^{XTE}_{l_1l'_2l'_3}\cos(2\phi_{l'_3l_3}) e^{i\mathbf{r}\cdot(\mathbf{l}'_2-\mathbf{l}_2)}\langle e^{i\mathbf{l}'_2\cdot\boldsymbol{\alpha}_2} e^{i\mathbf{l}'_3\cdot\boldsymbol{\alpha}_3}\rangle \tag{4.22}$$

where $\mathbf{l}_{3'} = -\mathbf{l}_1 - \mathbf{l}'_2$. In the squeezed limit, expanding around $\mathbf{l}_1$ gives $\cos(2\phi_{l'_3l_3}) \approx \cos(2\phi_{l'l}) + \mathcal{O}(l_1/l)$. Hence neglecting non-Gaussianity of lensing potentials and very small terms for squeezed shapes we have

$$\tilde{b}^{XTE}_{l_1l_2l_3} \;\approx\; \int \frac{d^2\mathbf{r}}{2\pi}\frac{d^2\mathbf{l}'}{2\pi} b^{XTE}_{l_1l'_2l'_3}\cos(2\phi_{l'l}) e^{i\mathbf{r}\cdot(\mathbf{l}'-\mathbf{l})}\exp\left(-\frac{l'^2}{2}[\sigma^2(r)+\cos 2\phi_{l'r}C_{\mathrm{gl},2}(r)]\right). \tag{4.23}$$

Using the expansion of Eq. (4.10), the angular integrals can be done as in the temperature case, giving a result in terms of modified and unmodified Bessel functions:

$$\tilde{b}^{(XTE)m}_{l_1 l} \approx \frac{1}{2}\int r dr \int dl' l' b^{(XTE)m}_{l_1 l'} e^{-l'^2\sigma^2(r)/2} \sum_n I_n[l'^2 C_{\mathrm{gl},2}(r)/2] \times \left[J_{2n+m+2}(l'r)J_{m+2}(lr) + J_{2n+m-2}(l'r)J_{m-2}(lr)\right]. \tag{4.24}$$

For the isotropic component $\tilde{b}^{(XTE)0}_{l_1 l}$ the two terms give equal contributions, and the result is then mathematically the same as the result of the lensed C_l^{TE} power spectrum in terms of the unlensed spectrum (see e.g. Lewis & Challinor (2006)). Note however that in general m does not have to be even in the case of the XTE bispectrum, since there is no symmetry between the two small-scale modes. Nonetheless we can expect the main lensing effect to be described in terms of the monopole component, at least for low l_1.

XEE bispectra

In the case where the two small-scale modes are of the same type, there is a symmetry under interchange of $\mathbf{l}_2$ and $\mathbf{l}_3$, and the approximations become valid to $\mathcal{O}(l_1^2/l^2)$: following the previous argument

$$\begin{aligned}\langle X(\mathbf{l}_1)\tilde{E}(\mathbf{l}_2)\tilde{E}(\mathbf{l}_3)\rangle &= \int \frac{d^2\mathbf{x}_2}{2\pi}\frac{d^2\mathbf{x}_3}{2\pi}\frac{d^2\mathbf{l}'_2}{2\pi}\frac{d^2\mathbf{l}'_3}{2\pi}\big\langle X(\mathbf{l}_1)E(\mathbf{l}'_2)E(\mathbf{l}'_3)e^{i\mathbf{l}'_2\cdot\boldsymbol{\alpha}_2}e^{i\mathbf{x}_2\cdot(\mathbf{l}'_2-\mathbf{l}_2)} \\ &\quad \times e^{i\mathbf{l}'_3\cdot\boldsymbol{\alpha}_3}e^{i\mathbf{x}_3\cdot(\mathbf{l}'_3-\mathbf{l}_3)}\cos(2\phi_{l'_3 l_3})\cos(2\phi_{l'_2 l_2})\big\rangle \\ &= \frac{1}{(2\pi)}\delta(\mathbf{l}_1+\mathbf{l}_2+\mathbf{l}_3)\int \frac{d^2\mathbf{r}}{2\pi}\frac{d^2\mathbf{l}'_2}{2\pi} b^{XEE}_{l_1 l'_2 l'_3}\cos(2\phi_{l'_3 l_3})\cos(2\phi_{l'_2 l_2}) \\ &\quad \times e^{i\mathbf{r}\cdot(\mathbf{l}'_2-\mathbf{l}_2)}\langle e^{i\mathbf{l}'_2\cdot\boldsymbol{\alpha}_2}e^{i\mathbf{l}'_3\cdot\boldsymbol{\alpha}_3}\rangle. \end{aligned} \tag{4.25}$$

But now in the squeezed limit, expanding in $\mathbf{l}_1$ gives $\cos(2\phi_{l'_3 l_3})\cos(2\phi_{l'_2 l_2}) = \cos^2(2\phi_{l'l}) + \mathcal{O}(l_1^2/l^2)$, and hence to $\mathcal{O}(l_1^2/l^2)$

$$\tilde{b}^{XEE}_{l_1 l_2 l_3} \approx \int \frac{d^2\mathbf{r}}{2\pi}\frac{d^2\mathbf{l}'}{2\pi} b^{XEE}_{l_1 l'_2 l'_3}\cos^2(2\phi_{l'l})e^{i\mathbf{r}\cdot(\mathbf{l}'-\mathbf{l})}\exp\left(-\frac{l'^2}{2}[\sigma^2(r)+\cos 2\phi_{l'r}C_{\mathrm{gl},2}(r)]\right). \tag{4.26}$$

Using the expansion of Eq. (4.10), Eq. (4.26) can then be calculated in terms of integrals of modified and unmodified Bessel functions:

$$\tilde{b}^{(XEE)m}_{l_1 l} \approx \frac{1}{4}\int r dr \int dl' l' b^{(XEE)m}_{l_1 l'} e^{-l'^2\sigma^2(r)/2} \sum_n I_n[l'^2 C_{\mathrm{gl},2}(r)/2] \times \left[2J_{2n+m}(l'r)J_m(lr) + J_{2n+m+4}(l'r)J_{m+4}(lr) + J_{2n+m-4}(l'r)J_{m-4}(lr)\right]. \tag{4.27}$$

Again the isotropic component $\tilde{b}^{(XEE)0}_{l_1 l}$ is given as expected in terms of the unlensed $b^{(XEE)0}_{l_1 l}$ in exactly the same way as the C_l^{EE} power spectrum is lensed.

XBB bispectra

The $\tilde{b}^{XBB}$ bispectrum gives a similar result to $\tilde{b}^{XEE}$, but we assume it is generated purely by lensing of a primordial b^{XEE} bispectrum:

$$\tilde{b}^{XBB}_{l_1 l_2 l_3} \approx \int \frac{d^2\mathbf{r}}{2\pi}\frac{d^2\mathbf{l}'}{2\pi} b^{XEE}_{l_1 l'_2 l'_3} \sin^2(2\phi_{l'l}) e^{i\mathbf{r}\cdot(\mathbf{l}'-\mathbf{l})} \exp\left(-\frac{l'^2}{2}[\sigma^2(r) + \cos 2\phi_{l'r} C_{\mathrm{gl},2}(r)]\right). \quad (4.28)$$

However since the unlensed XBB signal is expected to be zero for squeezed shapes it is unlikely to be important to model this in the immediate future.

4.1.3 Full sky

So far we have only used the flat-sky approximation. This is very helpful for clarifying the relevant physics and keeping results simple, but in reality the observations that we have are of the full sky. Since squeezed triangles involve large-scale modes, it is therefore important to use a full spherical analysis. It can be shown that as expected, the equivalent of Eq. (4.10), shows that bispectra with different angular dependence remain orthogonal in the squeezed limit. A full analysis should then consider how these are lensed. Appendix B of Pearson et al. (2012) gives the full sky angular dependence of the bispectrum (Eq. (B9)) and describes how it reduces to Eq. (4.11) in the flat sky limit.

Focussing on isotropic squeezed bispectra of most interest for primordial non-Gaussianity, we can simply use the understanding from the flat sky that the effect of lensing is just to lens the small-scale power, i.e. we apply the usual curved-sky CMB power spectrum lensing method (Challinor & Lewis, 2005; Lewis & Challinor, 2006) to the reduced full-sky bispectrum $b^m_{l_1 l}$, where $l = (l_1 + l_2)/2$, separately for each value of l_1. The computational cost of this method is then just $N_m \times l_{1,\mathrm{max}}$ times more expensive than lensing the power spectrum, and since the latter operation only costs a fraction of a second on a single CPU this is not problematic if only one or two angular moments ($N_m = 1, 2$) are required. By contrast the leading perturbative calculation (Hanson et al., 2009) is computationally very challenging, though it has the advantage of also being directly applicable to non-squeezed shapes. In detail we split the unlensed local bispectrum up into $b^0_{l_1 l}$ and $b^2_{l_1 l}$, and a small residual, lens the $m = 0$ and $m = 2$ bispectra for $l_1 < 1000$ using a modification of the standard method for lensing the full-sky temperature power spectrum (Seljak, 1996; Challinor & Lewis, 2005), and then add back on the small (unlensed) residual part to obtain our estimate of the full lensed bispectrum. Our approximations are not valid for $l_1 \gg 500$, and the high l_1 angular moments become expensive to calculate, however most of the signal is at lower l_1, so we only apply the lensing for $l_1 < 1000$ and approximate the

(very small) contributions from higher l_1 as being unlensed. It turns out that the $m = 2$ part of the bispectrum is rather smooth and not effected much by lensing, so lensing only the $m = 0$ component is usually sufficient (Fig. 4.1).

Using our simple prescription for lensing the local non-Gaussianity we can then easily calculate various useful results to quantify the importance of lensing. Consider first noise-free temperature data to $l_{\rm max} = 2000$. We find that the lensed local bispectrum is correlated at the > 0.999 level with the unlensed bispectrum, with the correction δb to the bispectrum due to lensing only biasing estimators based on the unlensed shape by $\sim 0.007 f_{\rm NL}$ (Hanson et al. (2009) have previously shown the bias is very small). This confirms that the correction due to lensing is almost orthogonal to the original shape, which should not be surprising since lensing preserves total power (see discussion below). The change in shape due to lensing δb is detectable at one sigma for $f_{\rm NL} \sim 93$. Including polarization data δb would be detectable from lensing of the isotropic component alone for $f_{\rm NL} \sim 22$, but the bias remains small, $\sim 0.01 f_{\rm NL}$. For Planck noise the current $f_{\rm NL}$ limit is enough to rule out any chance of detecting the effect of lensing and we confirm the bias is negligible.

4.2 Comparison with simulations

To test our new approximation we compared it with simulations. We generated 480 full-sky Healpix (Gorski et al., 2005) maps at $l_{\rm max} = 2500, n_{\rm side} = 2048$ with $f_{\rm NL} = 100$ following the method of Ref. Hanson et al. (2009). The unlensed input power spectra were taken from CAMB (Lewis et al., 2000). The lensing potential power spectrum was then used to simulate uncorrelated lensing deflection angle maps, and the unlensed maps were then lensed using LensPix (Lewis, 2005; Hamimeche & Lewis, 2008). An estimator for the bispectrum in each full-sky noise-free realization is

$$\hat{B}^{ijk}_{l_1 l_2 l_3} = \sum_{m_1, m_2, m_3} \begin{pmatrix} l_1 & l_2 & l_3 \\ m_1 & m_2 & m_3 \end{pmatrix} a^i_{l_1 m_1} a^j_{l_2 m_2} a^k_{l_3 m_3}, \tag{4.29}$$

where i labels T, E or B, and we can relate to the reduced bispectrum $b_{l_1 l_2 l_3}$ defined using:

$$B_{l_1 l_2 l_3} = \sqrt{\frac{(2l_1+1)(2l_2+1)(2l_3+1)}{4\pi}} \begin{pmatrix} l_1 & l_2 & l_3 \\ 0 & 0 & 0 \end{pmatrix} b_{l_1 l_2 l_3}. \tag{4.30}$$

This equation holds only for the even-parity bispectra ($l_1 + l_2 + l_3 = even$), which are all we consider in this work. To reduce the variance and therefore the number of simulations needed to average over, we follow Hanson et al. (2009) by subtracting a term that averages

to give zero bispectrum, but removes much of the realization-dependent variance. We also took advantage of symmetries to reduce the number of sums, using:

$$\hat{B}'_{l_1 l_2 l_3} = \sum_{m_2=0}^{l_2} \sum_{m_3=-l_3}^{l_3} (2-\delta_{0m_2}) \begin{pmatrix} l_1 & l_2 & l_3 \\ m_1 & m_2 & m_3 \end{pmatrix} \Re\left[a_{l_1 m_1} a_{l_2 m_2} a_{l_3 m_3} - \bar{a}_{l_1 m_1} \bar{a}_{l_2 m_2} \bar{a}_{l_3 m_3}\right] \tag{4.31}$$

where $m_1 = -m_2 - m_3$, and a_{lm} and $\bar{a}_{lm}$ are the lensed spherical harmonic coefficients from maps generated using the same random seeds but with $f_{\rm NL} \neq 0$ and $f_{\rm NL} = 0$ respectively. Since we were running multiple simulations, and computational cost is nearly dominated by calculation of the $3j$ symbol, for each set of $\{l, m\}$ we calculated the slice contributions from as many simulations as we could hold in memory. To avoid confusion with a lensing-induced bispectrum, the lensing potential is generated with $C_l^{T\psi} = C_l^{E\psi} = 0$, so that the subtracted term involving $\bar{a}$ gives zero bispectrum on average. To test our bispectrum estimation method we compared unlensed simulated bispectra slices to the theory unlensed reduced bispectra generated by CAMB, with good agreement.

As a first check on polarization bispectra, we used the publicly-available simulated non-Gaussian polarization maps from Elsner & Wandelt (2009), which have a maximum multipole of 1024.

Simulation results

For the pure temperature bispectrum $b^{TTT}_{l_1 l_2 l_3}$ simulations were run up to a maximum multipole of 2000. (Although the full-sky Healpix (Gorski et al., 2005) maps were $l_{\rm max} = 2500$, the lensing process requires a few hundred more multipoles than the scale you want to resolve.) The first acoustic peak of the CMB temperature power spectrum at $l \sim 200$ corresponds to the scale which has just had time to maximally compress or expand by the time of recombination. Therefore a bispectrum with $l_1 = 10$ corresponds to very large super-horizon modulations in the small-scale power; this modulation is roughly constant through the surface of last scattering (the approximation of Eq. (4.17)). However a bispectrum with $l_1 = 200$ will give a modulation in small-scale power that varies significantly through the thickness of the last-scattering surface. We have tested our lensing approximation for both the case of constant and non-constant modulation by simulating bispectra with both $l_1 = 10$ and $l_1 = 200$.

Because of the closure condition, a bispectrum with equal small-scale modes ($l_2 = l_3$) looks like an isosceles triangle, where the large-scale mode is roughly orthogonal to the short scale modes. For $l_3 = l_1 + l_2$ (eg. $b_{10,l,l+10}$), the closure condition demands that

the triangle you draw has zero area and all the modes are aligned (parallel). We test if our lensing approximation holds for both orientations of modes by calculating bispectrum slices for both cases where possible. Since there is a significant quadrupolar $m = 2$ part of the bispectrum for $l_1 = 200$, the slices for the different mode orientations are quite different, and our simulations test that the decomposition of the bispectrum into modes, and lensing just the monopole part, works consistently. For $l_1 = 10$ the bispectrum is nearly isotropic, so the slices are very similar.

Figure 4.2 shows the fractional change due to lensing for the reduced bispectrum slices $b^{TTT}_{10,l,l+10}$ and $b^{TTT}_{10,l,l}$, averaged over 480 simulated maps. In these plots the simulated fractional change has been normalized to remove variance from the large-scale l_1 modes: since $l_1 = 10$ is a super-horizon mode, its modulation is roughly constant across last scattering and the bispectrum is roughly proportional to $C^{T\zeta_*}_{l_1}$ (Eq. (4.17)). In general, variance on larger scale modes is larger, since there are less angular modes to average over. For roughly constant large-scale modulation normalizing can help to reduce the realisation dependent variance, which then cancels in the numerator and denominator. Both slices agree very well with the simulations, but the $b^{TTT}_{10,l,l}$ slice has more sampling noise as discussed further below.

Figure 4.3 shows the effect of lensing on the $b^{TTT}_{200,l,l+200}$ slice, which also agrees with the theoretical calculation despite the more complicated sub-horizon form of the bispectrum. For larger l_1 the bispectrum is no longer isotropic, so $b^{TTT}_{200,l,l+200}$ and $b^{TTT}_{200,l,l}$ differ significantly because of the large $m = 2$ quadrupole component. Contributions to the signal to noise are roughly equal for every $d\phi$ of angle between the long and the short modes; however since for squeezed shapes $l_3 \sim l_2 + l_1 \cos(\phi)$, there are more integer l_3 per unit angle for orthogonal triangles ($\phi \sim \pi/2$, $l_2 \sim l_3$) than parallel ($\phi \sim 0$, $l_2 \sim l_3 \pm l_1$). The signal to noise per slice is therefore much less for an individual slice with $l_2 \sim l_3$ than $l_2 \sim l_3 \pm l_1$, though the overall contribution to the signal is equally important for the different orientations.The simulation sample variance on $b^{TTT}_{200,l,l}$ was too large to see the lensing effect on a single slice (the fractional effect of lensing is also smaller for triangle shapes to which the smooth $m = 2$ bispectrum component contributes significantly; c.f. Fig. 4.1).

Polarization bispectra were estimated up to a maximum multipole of ~ 900. Figure 4.4 shows the reduced bispectra for the polarization slices $b^{TTE}_{10,l,l+10}$ and $b^{TEE}_{10,l,l+10}$, which were also normalized to remove large-scale variance. The agreement of the simulations with the theory is seen by eye, as well as the characteristic smoothing of peaks due to lensing.

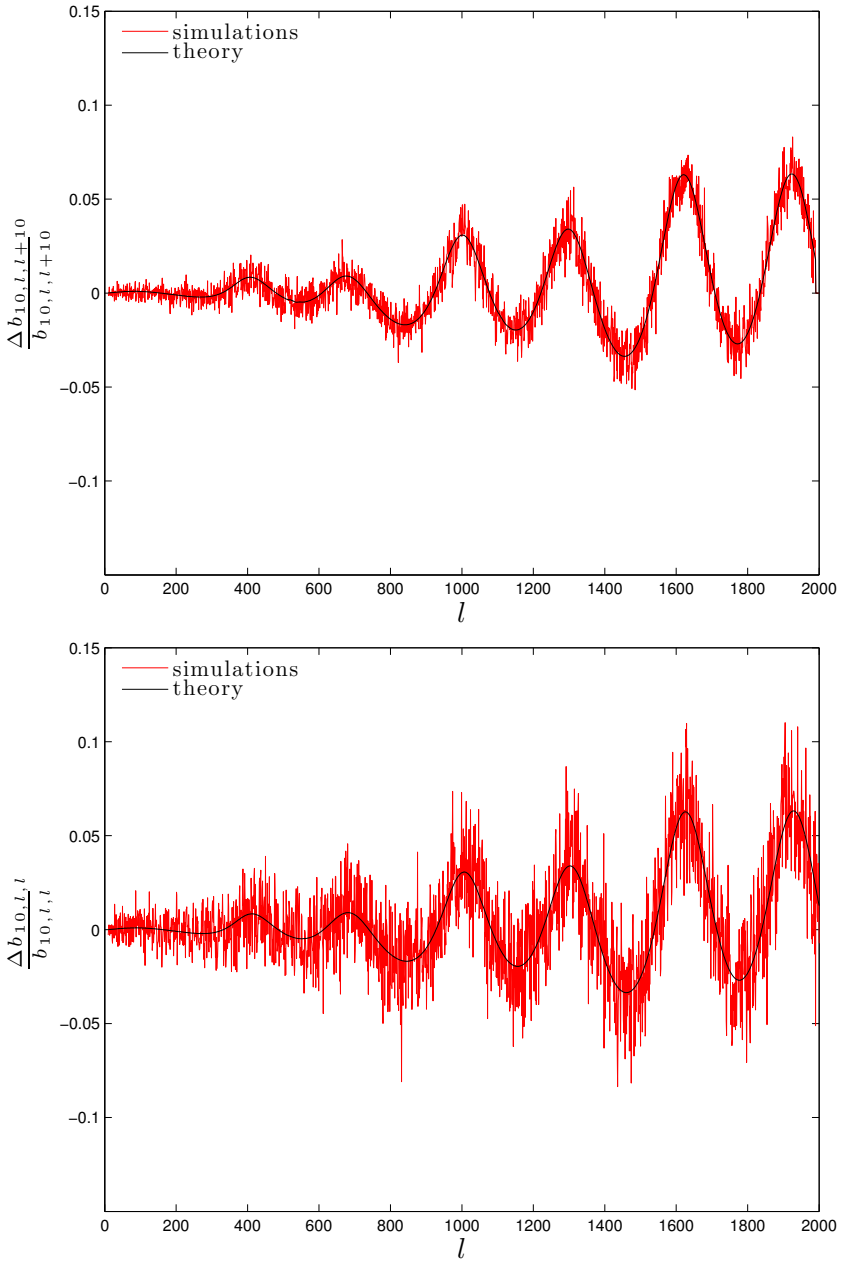

Figure 4.2: The fractional change due to lensing in the reduced bispectrum slices $b^{TTT}_{10,l,l+10}$ and $b^{TTT}_{10,l,l}$. The red shows the simulated result averaged over 480 realizations. The $b^{TTT}_{10,l,l}$ slice is somewhat noisier than the $b^{TTT}_{10,l,l+10}$ slice (see discussion in text). The black line is the theoretical approximation of this work, which agrees well with the simulations to within sample variance.

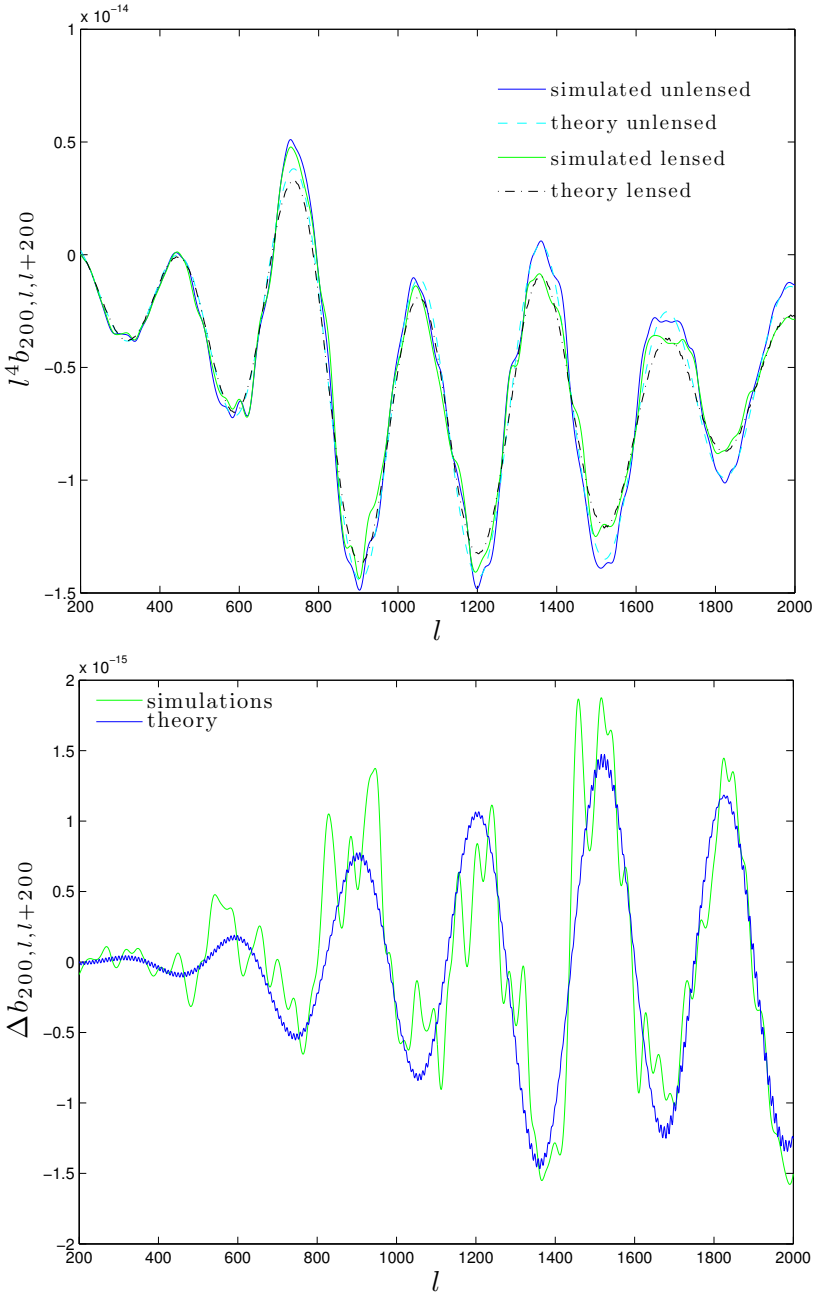

Figure 4.3: Bispectrum slice $b^{TTT}_{200,l,l+200}$. The top panel shows a comparison of the simulated vs theory lensed and unlensed bispectra, averaged over 480 realizations and smoothed over $\Delta l = 10$. The bottom panel gives the difference between the lensed and unlensed bispectrum for both simulations and theory, showing good agreement within the sample variance.

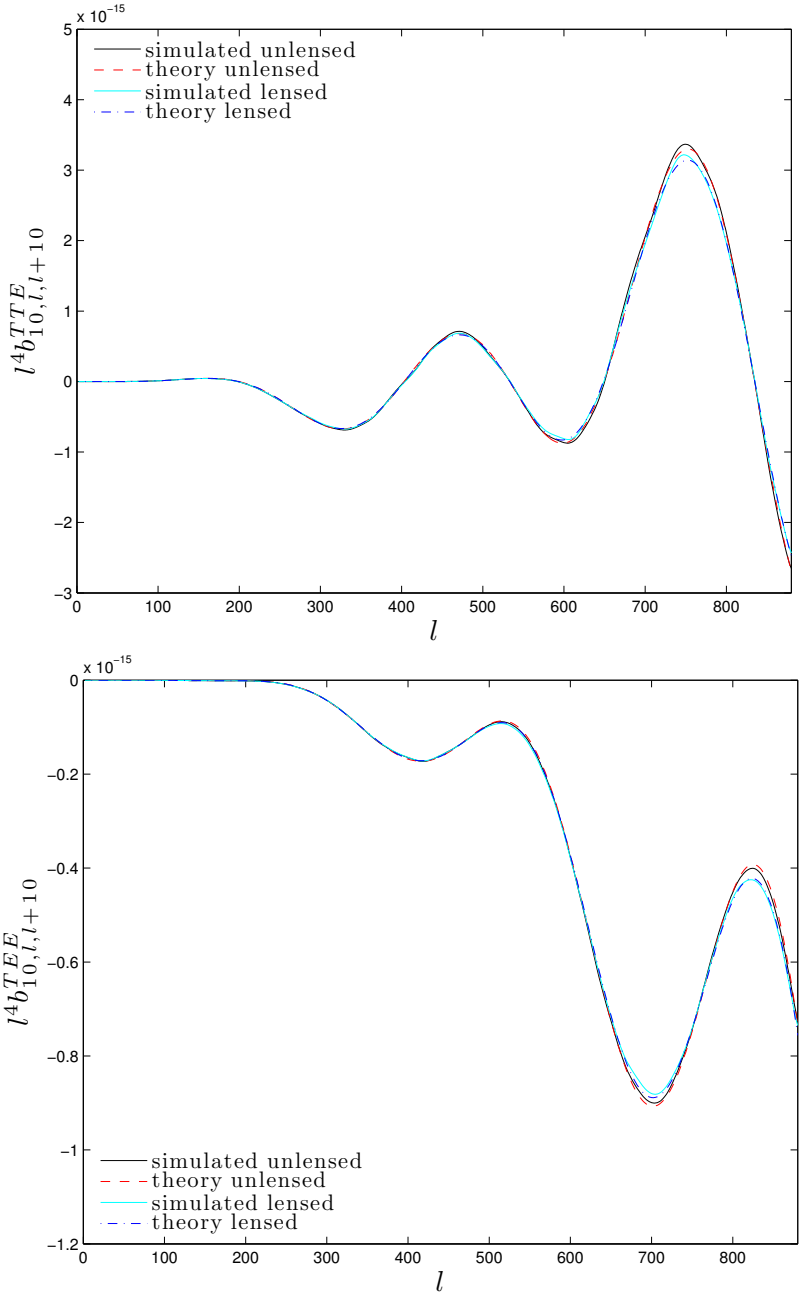

Figure 4.4: The reduced bispectrum slices $b^{TTE}_{10,l,l+10}$ and $b^{TEE}_{10,l,l+10}$ averaged over 99 realizations and smoothed over 10 l. The black and cyan lines show the simulated and normalized unlensed and lensed bispectra. The dashed red line shows the normal theoretical unlensed bispectrum, and the dark blue dot-dashed line shows the lensed approximation of the bispectrum tested in this work.

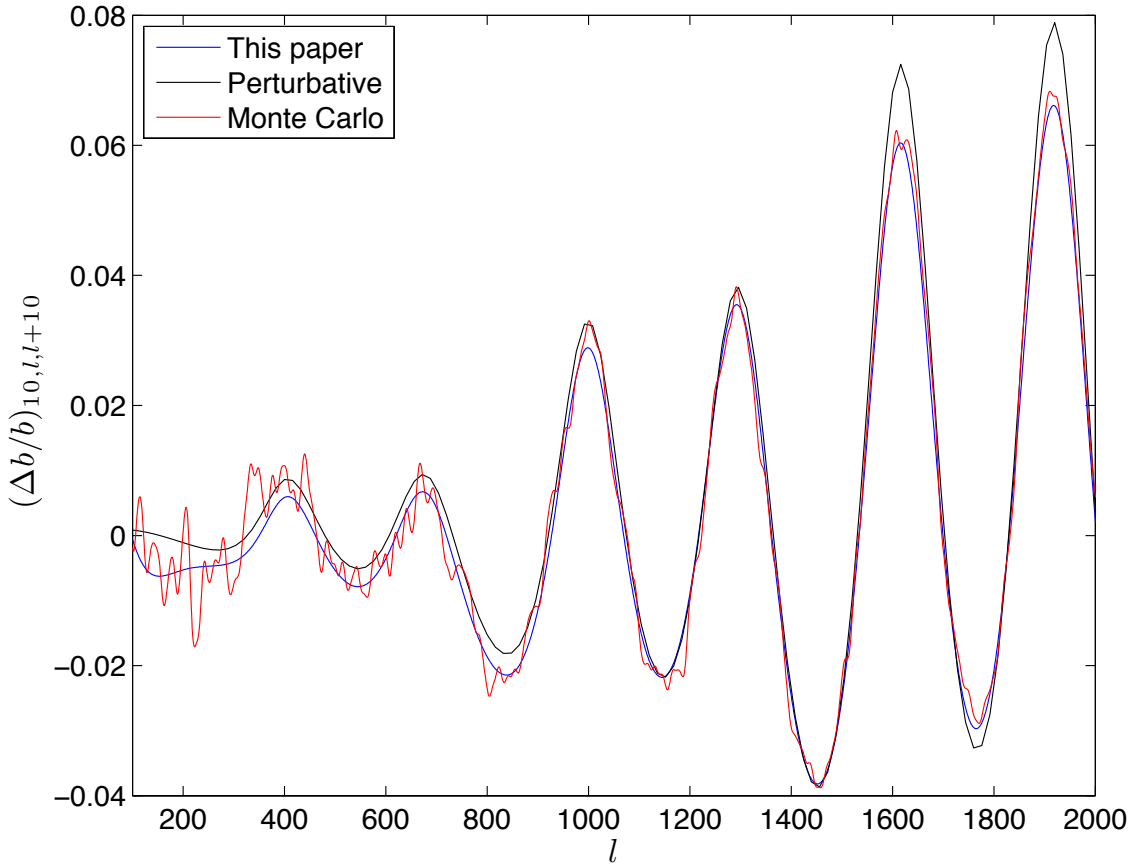

Figure 4.5: The fractional change in the reduced bispectrum slice $b_{10,l,l+10}$ due to lensing. The blue line shows the non-perturbative approximation of this work, the black line shows the leading-order perturbative result from Hanson et al. (2009). The red lines show the result of 1000 Monte Carlo simulations of Hanson et al. (2009) smoothed over $\Delta l = 5$. The new approximation only needs to lens the isotropic component of the bispectrum, and then is both significantly more accurate on small scales and faster to compute.

Comparison with perturbative result

In Fig. 4.5 we compare our new approximation to the result from the leading perturbative approximation of Cooray et al. (2008); Hanson et al. (2009) for a squeezed bispectrum slice. The perturbative calculation captures the main effect, but the new approximation is more accurate on small scales; this is essentially exactly the same as the effect of higher-order correction on the power spectrum (Challinor & Lewis, 2005), since it is the power spectrum that enters the squeezed form of the local bispectrum (Eq. (4.17)). Our non-perturbative bispectrum approximation is easier to calculate since it only requires a standard CMB power spectrum lensing calculation for each l_1 (only the isotropic part of the bispectrum needs to be lensed to good accuracy). We have only compared with one slice of the full

leading perturbative result due to the high numerical cost of calculating the lensed spectra that way.

4.3 Summary

We have discussed two effects of lensing. Firstly, the presence of large-scale lensing modes modulates the small-scale CMB and hence partially mimic the effect of primordial modulations, giving rise to a bispectrum signal that is potentially a source of confusion with primordial non-Gaussianity. The lensing effect is well-known to project onto the local non-Gaussianity model at the significant level of $f_{\rm NL} \sim 9$. Secondly, the effect of many smaller-scale lensing modes changes the detailed shape of any primordial bispectrum, similar to the smoothing effect on the power spectrum. For squeezed shapes we showed how this effect can easily be calculated, and that it is well approximated as applying CMB power spectrum lensing to each slice of the $m = 0$ isotropic part of the squeezed bispectrum.

The potential bias on primordial signals due to the average change in the primordial shape due to CMB lensing is however very small. This is easily understood: since CMB lensing just moves points around, the nth moment of the temperature at any given point $\langle [T(\mathbf{x})]^n \rangle$ is unchanged under lensing on average, for example the total power is conserved:

$$\langle T(\mathbf{x})^2 \rangle = \int \mathrm{d}\ln l \, \frac{l^2 C_l}{2\pi} = \int \mathrm{d}\ln l \, \frac{l^2 \tilde{C}_l}{2\pi}. \tag{4.32}$$

Local non-Gaussianity looks like a modulation of small-scale power as a function of position. In the squeezed limit we are considering very large-scale modulations, and the simplest way to measure the modulation is just to calculate the small-scale fluctuation variance as a function of position. However this variance is unchanged under lensing, and hence the non-Gaussianity estimate is unchanged under lensing on average, so it is unbiased. The total local skewness $\langle [T(\mathbf{x})]^3 \rangle$ is also invariant under lensing on average, giving[1]

$$\langle T(\mathbf{x})^3 \rangle = \int \frac{\mathrm{d}^2\mathbf{l}_1 \mathrm{d}^2\mathbf{l}}{(2\pi)^4} \, b_{l_1 l_2 l_3} = \int \frac{\mathrm{d}^2\mathbf{l}_1 \mathrm{d}^2\mathbf{l}}{(2\pi)^4} \, \tilde{b}_{l_1 l_2 l_3}. \tag{4.33}$$

In reality the picture is a bit more complicated because estimators weight by the inverse signal plus noise, so the estimators are not exactly unbiased, but nonetheless there is a good reason why the bias is expected to be small for local shapes. The detailed change in shape due to lensing could in principle be detected if $f_{\rm NL} \geq 20$, but the change is almost

[1] This is consistent with the exact bispectrum lensing result because $\sigma^2(0) = C_{\mathrm{gl},2}(0) = 0$. Note also that only the isotropic part of the bispectrum contributes to the skewness.

orthogonal to the unlensed shape and hence neglecting it is usually harmless. On the other hand the bias due to correlation between primordial and lensing-induced non-Gaussianity should be subtracted or consistently modelled to avoid biases. Lensing also affects the variance of non-Gaussianity estimators; this has been calculated in Hanson et al. (2009), and optimized bispectrum estimators accounting for this extra variance have been derived in Lewis et al. (2011).

Chapter 5

Discussion and Conclusions

The future of cosmology is bright. We have made tremendous progress in the last twenty-five years, but there remains much work to be done. To better understand the distant past, the period of inflation in the first fraction of a second, and the distant future, the era of dark energy domination, the next frontiers include measuring the large-scale structure of the universe, searching for non-Gaussianities in the primordial perturbations, and detecting tensor modes in the CMB. Data are pouring in from both surveys of the large-scale structure and next generation CMB polarization instruments. With this new data comes new challenges: to extract the maximum cosmic information from our investments requires the construction of optimal estimators, cross-correlation, and inventive ways to deal with noise, foregrounds and cuts.

In Chapter 2 we forecasted the ability of upcoming CMB polarisation data to reconstruct the lensing potential using the pure-B mode estimator. The reconstruction improvement afforded by CMB polarisation measurements will enable precision measurements of the lensing power spectrum leading to improved constraints on cosmological parameters. The lensing is sensitive to small scale effects providing an extra probe of the neutrino mass sum $\sum m_\nu$. As such the lensing information breaks the degeneracy between the neutrino mass sum $\sum m_\nu$ and the dark energy fraction Ω_Λ, leading to tighter constraints of both parameters compared to an analysis of the CMB without lensing data. As well as improving parameter constraints from the CMB, this improved measurement of the lensing potential will be a useful probe of the underlying matter distribution of the universe hence aiding large-scale structure analysis.

In Chapter 3 we forecast the information content of the cross-correlation of the lensing potential with the galaxy power spectrum, a large-scale structure tracer. We find that it leads to improved parameter constraints on both galactic and non-galactic cosmolo-

gical parameters as compared to analysing the CMB and large-scale structure separately. There are many opportunities to explore for exploiting the cross-correlation information, and many logical extensions of the work presented in Chapter 3. For example, modelling the redshift dependence of the bias and using full 3-Dimensional galaxy information. For photometric surveys, the lack of spectra makes it difficult to measure the redshift distribution of the galaxies. When you can not measure the redshift of the sources accurately, for any increase in power it is difficult to distinguish between more galaxies or a higher bias. This degeneracy between the galaxy bias and the redshift distribution makes it difficult to constrain the two parameters independently from galaxy information alone. However, the addition of CMB lensing information and good redshift modelling could break the degeneracy and allow the two to be constrained separately.

Another piece of information in the large-scale structure data is the weak lensing of the galaxies themselves. The elliptical shape of the galaxy gets altered slightly by the effect of gravitational lensing. Measurements of this will teach us much about the nature of dark energy. This is a difficult task, since the analysis is plagued with difficult systematics; difficulties in determining the point spread function (PSF) of galaxies; difficulties determining the precise redshift of the galaxies and difficulties in understanding the intrinsic alignment of galaxies. It is already known that the weak lensing information can be used in combination with CMB lensing and structure surveys to better constrain cosmology. (For example Ref. Hall & Taylor (2014) recently found that the intrinsic alignment of galaxies leads to an additional term in the CMB lensing and weak lensing cross power spectrum.) However, there is much to be done in this field. The particular degeneracies which joint analysis of data sets can break need to be found, and their physical origins understood. Techniques must be developed to optimally analyse the data sets in combination. The Large Synoptic Survey Telescope (LSST) will make precision measurements of the weak lensing effect using state of the art instruments and techniques such as adaptive optics. It will take high quality image data of galaxies and provide high precision photometric redshift determination. It is precisely this kind of data set which will benefit from exploitation of the CMB lensing information along with joint and cross correlation analysis. The addition of CMB lensing information to LSST is likely crucial in discriminating dynamical dark energy models.

In Chapter 4 we derived a useful analytical expression for the lensed squeezed primordial bispectrum. Although data from the Planck satellite (Ade et al., 2013h) has since found the level of non-Gaussianity in the universe to be consistent with zero, the search

is still on for primordial non-Gaussian signatures. If it exists, non-Gaussianity will affect the large-scale structure as well as the CMB sky. In particular, a local non-Gaussianity causes a change on large scales of the halo bias. As structure surveys and observations improve, so do opportunities to observe this non-Gaussian signature.

Bibliography

Abbott T., et al. (2005). The dark energy survey. astro-ph/0510346. Cited on 6

Abell P. A., et al. (2009). LSST Science Book, Version 2.0. 0912.0201. Cited on 6, 50, 52

Ade P., et al. (2013a). Evidence for Gravitational Lensing of the Cosmic Microwave Background Polarization from Cross-correlation with the Cosmic Infrared Background. 1312.6645. Cited on 23

Ade P., et al. (2013b). Gravitational Lensing of Cosmic Microwave Background Polarization. 1312.6646. Cited on 23, 41, 43, 46

Ade P., et al. (2013c). Planck 2013 results. I. Overview of products and scientific results. 1303.5062. Cited on 49

Ade P., et al. (2013d). Planck 2013 results. XIX. The integrated Sachs-Wolfe effect. 1303.5079. Cited on 48

Ade P., et al. (2013e). Planck 2013 results. XV. CMB power spectra and likelihood. 1303.5075. Cited on 8, 9, 46

Ade P., et al. (2013f). Planck 2013 results. XVII. Gravitational lensing by large-scale structure. 1303.5077. Cited on 23, 45, 46, 50

Ade P., et al. (2013g). Planck 2013 results. XVIII. Gravitational lensing-infrared background correlation. 1303.5078. Cited on 48

Ade P., et al. (2013h). Planck 2013 Results. XXIV. Constraints on primordial non-Gaussianity. 1303.5084. Cited on 83

Anderes E. (2013). Decomposing CMB lensing power with simulation. Phys. Rev. D, 88:083517, 1301.2576. Cited on 25

Austermann J., Aird K., Beall J., Becker D., Bender A., et al. (2012). SPTpol: an instrument for CMB polarization measurements with the South Pole Telescope. *Proc.SPIE Int.Soc.Opt.Eng.*, 8452:84520E, 1210.4970. Cited on 4, 50

Benoit-Levy A., Dechelette T., Benabed K., Cardoso J.-F., Hanson D., et al. (2013). Full-sky CMB lensing reconstruction in presence of sky-cuts. A&A, 555:A37, 1301.4145. Cited on 37

Bernardeau F., Colombi S., Gaztanaga E., Scoccimarro R. (2002). Large scale structure of the universe and cosmological perturbation theory. *Phys.Rept.*, 367:1–248, astro-ph/0112551. Cited on 21

Bleem L., van Engelen A., Holder G., Aird K., Armstrong R., et al. (2012). A Measurement of the Correlation of Galaxy Surveys with CMB Lensing Convergence Maps from the South Pole Telescope. 1203.4808. Cited on 45

Boldrin M., Giocoli C., Meneghetti M., Moscardini L. (2012). Predicting the number of giant arcs expected in the next generation wide-field surveys from space. 1209.2709. Cited on 52

Bunn E. F., Zaldarriaga M., Tegmark M., Oliveira-Costa A. d. (2003). E/B decomposition of finite pixelized CMB maps. *Phys. Rev.*, D67:023501, astro-ph/0207338. Cited on 28, 29

Calabrese E., Hlozek R. A., Battaglia N., Battistelli E. S., Bond J. R., et al. (2013). Cosmological parameters from pre-planck cosmic microwave background measurements. *Phys.Rev.*, D87(10):103012, 1302.1841. Cited on 46

Challinor A., Lewis A. (2005). Lensed cmb power spectra from all-sky correlation functions. *Phys. Rev.*, D71:103010, astro-ph/0502425. Cited on 66, 72, 79

Challinor A., Peiris H. (2009). Lecture notes on the physics of cosmic microwave background anisotropies. *AIP Conf.Proc.*, 1132:86–140, 0903.5158. Cited on 7

Challinor A., Lewis A. (2011). The linear power spectrum of observed source number counts. *Phys.Rev.*, D84:043516, 1105.5292. Cited on 49

Cooray A., Sarkar D., Serra P. (2008). Weak Lensing of the Primary CMB Bispectrum. *Phys. Rev.*, D77:123006, 0803.4194. Cited on 79

Creminelli P., Pitrou C., Vernizzi F. (2011). The CMB bispectrum in the squeezed limit. *JCAP*, 1111:025, 1109.1822. Cited on 69

Das S., Sherwin B. D., Aguirre P., Appel J. W., Bond J., et al. (2011). Detection of the Power Spectrum of Cosmic Microwave Background Lensing by the Atacama Cosmology Telescope. *Phys.Rev.Lett.*, 107:021301, 1103.2124. Cited on 23, 46

Das S., Louis T., Nolta M. R., Addison G. E., Battistelli E. S., et al. (2013). The Atacama Cosmology Telescope: Temperature and Gravitational Lensing Power Spectrum Measurements from Three Seasons of Data. 1301.1037. Cited on 23, 46

Dekel A., Lahav O. (1999). Stochastic Nonlinear Galaxy Biasing. ApJ, 520:24–34, astro-ph/9806193. Cited on 20

Dodelson S. (2003). *Modern Cosmology*. Academic Press. Academic Press. ISBN: 9780122191411. Cited on 2

Elsner F., Wandelt B. D. (2009). Improved simulation of non-Gaussian temperature and polarization CMB maps. *Astrophys.J.Suppl.*, 184:264–270, 0909.0009. Cited on 74

ESA (accessed 11 Feb 2014). *Planck satellite ESA mission page*. `http://www.esa.int/Our_Activities/Space_Science/Planck`. Cited on 3

Feng C., Aslanyan G., Manohar A. V., Keating B., Paar H. P., et al. (2012). Measuring Gravitational Lensing of the Cosmic Microwave Background using cross-correlation with large scale structure. *Phys.Rev.*, D86:063519, 1207.3326. Cited on 45

Geach J., Hickox R., Bleem L., Brodwin M., Holder G., et al. (2013). A Direct Measurement of the Linear Bias of Mid-infrared-selected Quasars at $z \approx 1$ Using Cosmic Microwave Background Lensing. *Astrophys.J.*, 776:L41, 1307.1706. Cited on 50, 52

Gorski K. M., et al. (2005). Healpix – a framework for high resolution discretization, and fast analysis of data distributed on the sphere. *Astrophys. J.*, 622:759–771, astro-ph/0409513. Cited on 73, 74

Goto T., Szapudi I., Granett B. R. (2012). Cross-correlation of WISE Galaxies with the Cosmic Microwave Background. 1202.5306. Cited on 50

Hall A., Taylor A. (2014). Intrinsic alignments in the cross-correlation of cosmic shear and CMB weak lensing. 1401.6018. Cited on 83

Hamimeche S., Lewis A. (2008). Likelihood analysis of cmb temperature and polarization power spectra. *Phys. Rev.*, D77:103013, arXiv:0801.0554 [astro-ph]. Cited on 73

Hanson D., Smith K. M., Challinor A., Liguori M. (2009). CMB lensing and primordial non-Gaussianity. *Phys. Rev.*, D80:083004, 0905.4732. Cited on 64, 65, 72, 73, 79, 81

Hanson D., Lewis A. (2009). Estimators for CMB Statistical Anisotropy. *Phys. Rev.*, D80:063004, 0908.0963. Cited on 23, 29, 35

Hanson D., Challinor A., Lewis A. (2010). Weak lensing of the CMB. *General Relativity and Gravitation*, 42:2197–2218, 0911.0612. Cited on 11, 22, 23

Hanson D., Challinor A., Efstathiou G., Bielewicz P. (2011). CMB temperature lensing power reconstruction. *Phys. Rev.*, D83:043005, 1008.4403. Cited on 25, 33

Hanson D., et al. (2013). Detection of B-mode Polarization in the Cosmic Microwave Background with Data from the South Pole Telescope. *Phys.Rev.Lett.*, 111:141301, 1307.5830. Cited on 23, 46

Hinshaw G., et al. (2013). Nine-Year Wilkinson Microwave Anisotropy Probe (WMAP) Observations: Cosmological Parameter Results. *Astrophys.J.Suppl.*, 208:19, 1212.5226. Cited on 46, 60

Hirata C. M., Seljak U. (2003a). Analyzing weak lensing of the cosmic microwave background using the likelihood function. *Phys. Rev.*, D67:043001, astro-ph/0209489. Cited on 16, 22, 29

Hirata C. M., Seljak U. (2003b). Reconstruction of lensing from the cosmic microwave background polarization. *Phys. Rev.*, D68:083002, astro-ph/0306354. Cited on 22, 23, 29

Hirata C. M., Ho S., Padmanabhan N., Seljak U., Bahcall N. A. (2008). Correlation of CMB with large-scale structure: II. Weak lensing. *Phys. Rev.*, D78:043520, 0801.0644. Cited on 45

Holder G., Viero M., Zahn O., Aird K., Benson B., et al. (2013). A Cosmic Microwave Background Lensing Mass Map and Its Correlation with the Cosmic Infrared Background. *Astrophys.J.*, 771:L16, 1303.5048. Cited on 45

Hu W. (2000). Weak lensing of the cmb: A harmonic approach. *Phys. Rev.*, D62:043007, astro-ph/0001303. Cited on 67

Hu W., Okamoto T. (2002). Mass reconstruction with CMB polarization. *Astrophys. J.*, 574:566–574, astro-ph/0111606. Cited on 22, 24, 25, 26, 27, 34, 37, 46, 48

Jones W. C., et al. (2006). A measurement of the angular power spectrum of the CMB temperature anisotropy from the 2003 flight of boomerang. ApJ, 647:823–832, astro-ph/0507494. Cited on 46

Kaiser N. (1984). On the Spatial correlations of Abell clusters. *Astrophys.J.*, 284:L9–L12. Cited on 21

Keisler R., Reichardt C., Aird K., Benson B., Bleem L., et al. (2011). A Measurement of the Damping Tail of the Cosmic Microwave Background Power Spectrum with the South Pole Telescope. *Astrophys.J.*, 743:28, 1105.3182. Cited on 46

Kermish Z., Ade P., Anthony A., Arnold K., Arnold K., et al. (2012). The POLARBEAR Experiment. 1210.7768. Cited on 4, 50

Kesden M., Cooray A., Kamionkowski M. (2003). Lensing reconstruction with CMB temperature and polarization. *Phys. Rev.*, D67:123507, astro-ph/0302536. Cited on 26, 34

Knox L. (1995). Determination of inflationary observables by cosmic microwave background anisotropy experiments. *Phys. Rev. D*, 52:4307–4318. Cited on 48

Laureijs R., et al. (2011). Euclid Definition Study Report. 1110.3193. Cited on 50

Leitch E. M., Kovac J., Halverson N., Carlstrom J., Pryke C., et al. (2005). DASI three-year cosmic microwave background polarization results. *Astrophys.J.*, 624:10–20, astro-ph/0409357. Cited on 46

Lewis A., Challinor A., Lasenby A. (2000). Efficient computation of CMB anisotropies in closed FRW models. *Astrophys. J.*, 538:473–476, astro-ph/9911177. Cited on 14, 31, 73

Lewis A., Challinor A., Turok N. (2002). Analysis of cmb polarization on an incomplete sky. *Phys. Rev.*, D65:023505, astro-ph/0106536. Cited on 28, 29

Lewis A. (2005). Lensed CMB simulation and parameter estimation. *Phys. Rev.*, D71:083008, astro-ph/0502469. Cited on 73

Lewis A., Challinor A. (2006). Weak gravitational lensing of the cmb. *Phys. Rept.*, 429:1–65, astro-ph/0601594. Cited on 11, 22, 65, 66, 70, 71, 72

Lewis A. (2011). The real shape of non-Gaussianities. *JCAP*, 1110:026, 1107.5431. Cited on 24, 67

Lewis A., Challinor A., Hanson D. (2011). The shape of the CMB lensing bispectrum. *JCAP*, 1103:018, 1101.2234. Cited on 24, 25, 65, 81

Liddle A., Lyth D. (2000). *Cosmological Inflation and Large-Scale Structure*. Cambridge University Press. Cited on 2, 21

Montroy T. E., et al. (2006). A measurement of the CMB spectrum from the 2003 flight of boomerang. ApJ, 647:813–822, astro-ph/0507514. Cited on 46

Namikawa T., Takahashi R. (2013). Bias-Hardened CMB Lensing with Polarization. 1310.2372. Cited on 36, 43

NASA (accessed 11 Feb 2014a). *Cosmic Background Explorer NASA mission page*. `http://lambda.gsfc.nasa.gov/product/cobe/`. Cited on 3

NASA (accessed 11 Feb 2014c). *Wilkinson Microwave Anisotropy Probe NASA mission page*. `http://map.gsfc.nasa.gov/`. Cited on 3

NASA (image added date: 2013-03-21 accessed 11 Feb 2014b). *NASA/JPL-Caltech/ESA photojournal*. `http://photojournal.jpl.nasa.gov/catalog/PIA16874`. Cited on 3

Niemack M., Ade P., Aguirre J., Barrientos F., Beall J., et al. (2010). ACTPol: A polarization-sensitive receiver for the Atacama Cosmology Telescope. *Proc.SPIE Int.Soc.Opt.Eng.*, 7741:77411S, 1006.5049. Cited on 4, 50

Okamoto T., Hu W. (2003). CMB lensing reconstruction of the full sky. *Phys. Rev.*, D67:083002, astro-ph/0301031. Cited on 22

Pearson R., Lewis A., Regan D. (2012). CMB lensing and primordial squeezed non-Gaussianity. *JCAP*, 1203:011, 1201.1010. Cited on 64, 72

Pearson R., Sherwin B., Lewis A. (2014). CMB lensing reconstruction using cut sky polarization maps and pure-B modes. 1403.3911. Cited on 22

Pearson R., Zahn O. (2014). Cosmology from cross correlation of cmb lensing and galaxy surveys. *Phys. Rev. D*, 89:043516. Cited on 45

Perotto L., Lesgourgues J., Hannestad S., Tu H., Wong Y. Y. (2006). Probing cosmological parameters with the CMB: Forecasts from full Monte Carlo simulations. *JCAP*, 0610:013, astro-ph/0606227. Cited on 48

Rhodes J., Allen S., Benson B., Chang T., de Putter R., et al. (2013). Exploiting Cross Correlations and Joint Analyses. 1309.5388. Cited on 47

Sanchez A. G., Montesano F., Kazin E. A., Aubourg E., Beutler F., et al. (2013). The clustering of galaxies in the SDSS-III Baryon Oscillation Spectroscopic Survey: cosmological implications of the full shape of the clustering wedges. *Mon.Not.Roy.Astron.Soc.*, 433:1202–1222, 1312.4854. Cited on 53

Schmittfull M. M., Challinor A., Hanson D., Lewis A. (2013). On the joint analysis of CMB temperature and lensing-reconstruction power spectra. *Phys.Rev.*, D88:063012, 1308.0286. Cited on 33, 53

Seljak U. (1996). Gravitational lensing effect on cosmic microwave background anisotropies: A power spectrum approach. *Astrophys. J.*, 463:1, astro-ph/9505109. Cited on 66, 72

Serra P., Cooray A. (2008). Impact of Secondary non-Gaussianities on the Search for Primordial Non-Gaussianity with CMB Maps. *Phys. Rev.*, D77:107305, 0801.3276. Cited on 65

Sherwin B. D., Dunkley J., Das S., Appel J. W., Bond J., et al. (2011). Evidence for dark energy from the cosmic microwave background alone using the Atacama Cosmology Telescope lensing measurements. *Phys.Rev.Lett.*, 107:021302, 1105.0419. Cited on 60

Sherwin B. D., Das S., Hajian A., Addison G., Bond J. R., et al. (2012). The Atacama Cosmology Telescope: Cross-Correlation of CMB Lensing and Quasars. *Phys.Rev.*, D86:083006, 1207.4543. Cited on 45

Smith K. M. (2006). Pseudo-c(l) estimators which do not mix E and B modes. *Phys.Rev.*, D74:083002, astro-ph/0511629. Cited on 28

Smith K. M., Zahn O., Dore O. (2007). Detection of gravitational lensing in the cosmic microwave background. *Phys. Rev.*, D76:043510, arXiv:0705.3980 [astro-ph]. Cited on 45

Smith K. M., Zaldarriaga M. (2007). A general solution to the E-B mixing problem. *Phys. Rev.*, D76:043001, astro-ph/0610059. Cited on 28, 29, 31

Smith K. M., Zaldarriaga M. (2011). Algorithms for bispectra: Forecasting, optimal analysis, and simulation. *Mon.Not.Roy.Astron.Soc.*, 417:2–19, astro-ph/0612571. Cited on 65

Smith R. E., Scoccimarro R., Sheth R. K. (2007). Scale dependence of halo and galaxy bias: Effects in real space. Phys. Rev. D, 75(6):063512, astro-ph/0609547. Cited on 20, 53

Spanos A. (1986). *Statistical Foundations of Econometric Modelling*. Cambridge University Press. Cited on 47

Stompor R., Efstathiou G. (1999). Gravitational lensing of cosmic microwave background anisotropies and cosmological parameter estimation. *Mon. Not. Roy. Astron. Soc.*, 302:735, astro-ph/9805294. Cited on 60

Story K., Reichardt C., Hou Z., Keisler R., Aird K., et al. (2013). A Measurement of the Cosmic Microwave Background Damping Tail from the 2500-square-degree SPT-SZ survey. *Astrophys.J.*, 779:86, 1210.7231. Cited on 46

Tauber J., et al. (2006). The Scientific programme of Planck. astro-ph/0604069. Cited on 49

Tegmark M. (1997). Measuring cosmological parameters with galaxy surveys. *Phys.Rev.Lett.*, 79:3806–3809, astro-ph/9706198. Cited on 47, 48

Vallinotto A. (2012). Using CMB lensing to constrain the multiplicative bias of cosmic shear. *Astrophys.J.*, 759:32, 1110.5339. Cited on 6, 47

Vallinotto A. (2013). The synergy between the Dark Energy Survey and the South Pole Telescope. *Astrophys.J.*, 778:108, 1304.3474. Cited on 47

van Engelen A., Keisler R., Zahn O., Aird K., Benson B., et al. (2012). A measurement of gravitational lensing of the microwave background using South Pole Telescope data. *Astrophys.J.*, 756:142, 1202.0546. Cited on 23, 46

Verde L. (2007). A practical guide to Basic Statistical Techniques for Data Analysis in Cosmology. *ArXiv e-prints*, 0712.3028. Cited on 47

Wright E. L., Eisenhardt P. R., Mainzer A., Ressler M. E., Cutri R. M., et al. (2010). The Wide-field Infrared Survey Explorer (WISE): Mission Description and Initial On-orbit Performance. *Astron.J.*, 140:1868, 1008.0031. Cited on 50

Zahn O. (2014). Lensing correlations. in preparation. Cited on 53

Zarija L. (2008). Nonlinear growth of structure in cosmological simulations. thesis, University of Chicago at Urbana Champaign. Cited on 53